RADAR SENSING OF OCEAN WAVE HEIGHTS

A THESIS SUBMITTED TO THE GRADUATE DIVISION OF THE
UNIVERSITY OF HAWAI'I IN PARTIAL FULFILLMENT
OF THE REQUIREMENTS FOR THE DEGREE OF

MASTER OF SCIENCE

IN

OCEANOGRAPHY

DECEMBER 2010

By
Tyson Hilmer

Thesis Committee:

Pierre Flament, Chairperson
Mark Merrifield
Douglas Luther

We certify that we have read this thesis and that, in our opinion, it is satisfactory in scope and quality as a thesis for the degree of Master of Science in Oceanography.

THESIS COMMITTEE

_____
Chairperson

_____

_____

This work is dedicated to

my beautiful wife Susanne

for her unequivocal patience

Acknowledgements

ABSTRACT

This thesis focuses on explaining and improving the estimation of ocean wave heights from high-frequency oceanographic radar. Three months of data from a WERA HF radar is compared to a Datawell MarkIII directional waverider buoy, under a wide range of sea states. Large spatial and temporal variation in the radar-derived waveheight, significantly greater than previously reported, are explained in terms of various error sources. Averaging and filtering methods for improving the significant waveheight are evaluated, and the dominant error source is shown to be external radio frequency interference. Eigen-analysis and model-based methods are evaluated for the removal of interference. A comprehensive summary of the second order radar-ocean scattering equations is given, with evaluation of its terms.

Contents

List of Tables

List of Figures

Chapter 1

Introduction

The data products from oceanographic radars can be separated into two fundamental categories delineated by the interaction mechanism of remote measurement. Foremost is first order scattering, due to coherent reflection of the electromagnetic wave off linear ocean waves of a fixed wavelength. The other mechanism is second order scattering, caused by similar coherent reflections off the continuum of nonlinear ocean waves. These two scattering mechanisms differ in how the information content is encoded in the radar signal, and by the physical process measured. The frequency shift of first order scatter allows oceanographic radars to generate large two dimensional maps of ocean surface currents. The scattering mechanism is relatively simple, and frequency differences are a robust radar measurement. The spectral amplitudes of second order scatter contains information about the full 2-dimensional sea surface, and consequently the directional wave spectrum. The scattering mechanism is relatively complex, and the measurement is not uniquely determined. Furthermore, the information carried in spectral amplitudes is sensitive to instrument performance and noise sources.

The motivation for this work is to further understanding and accuracy of the second order radar measurement. HF radars are unique in their ability to provide dense three-dimensional observations which are outside the scope of other instruments. Prior success in ocean wave measurement via HF radar has been demonstrated, but there is a demand for further observation and validation. The theoretical and empirical relationship between the radar Doppler spectrum and ocean surface is

1

an ongoing field of study. Much of this thesis focuses on how the Doppler spectrum is processed to yield oceanographic parameters, primarily significant waveheight.

1.1 Applications

Oceanographic radar is capable of providing wide-area measurements that are difficult or impossible to make any other way. Their development and application as an oceanographic research tool began in 1955, and their performance is now widely established. Using electromagnetic and hydrodynamic theory, it is possible to infer information about the ocean surface; primarily its shape and velocity, from the radar Doppler spectrum. Radar provides continuous, synoptic measurement of physical oceanographic properties; two-dimensional spatial maps of surface-current vectors, the surface wave directional spectrum, significant waveheight, and surface wind direction. The benefit of radar over conventional in-situ instruments is the spatial measurement field; typically $O(10{,}000)$ measurement points over a 2-dimensional area, with range depending on the transmit frequency. Comparable in-situ instruments, such as buoys, pressure sensors, ADCPs, and ECMs, provide relatively smaller spatial coverage or a point measurement. Conversely, satellite remote sensing; e.g. radar altimeters, synthetic aperature radars, scatterometers, and microwave radiometers, provide relatively coarser spatial coverage over a larger region. Complete spatial fields are available every 10-30 minutes, dependent on the coherent integration time of the spectra. The majority of radar installations are shore based, although several ship-board experiments have been conducted [Gurgel and Essen, 2000].

The large observational area and near real-time availability of oceanographic radar offers a variety of real-world applications. They are capable of monitoring sea state and weather conditions, whilst simultaneously tracking ships and even iceburgs. Current maps aid in oil spill containment and search-and-rescue operations. Ship and object detection is used for vessel traffic control and Exclusive Economic Zone enforcement. Wind estimates are useful for detecting frontal boundaries [Fernandez et al., 1997] and other sudden changes in direction, e.g. small-scale storms and waterspouts. While sea state monitoring is used for engineering projects, and safety conditions for beaches and the recreational nearshore.

1.2 Operational Description of Oceanographic Radars

Oceanographic radars typically operate in the High-Frequency (HF) radio band (3-30 MHz), and at very low power (30 W). The radar transmits a nearly monochromatic electromag-
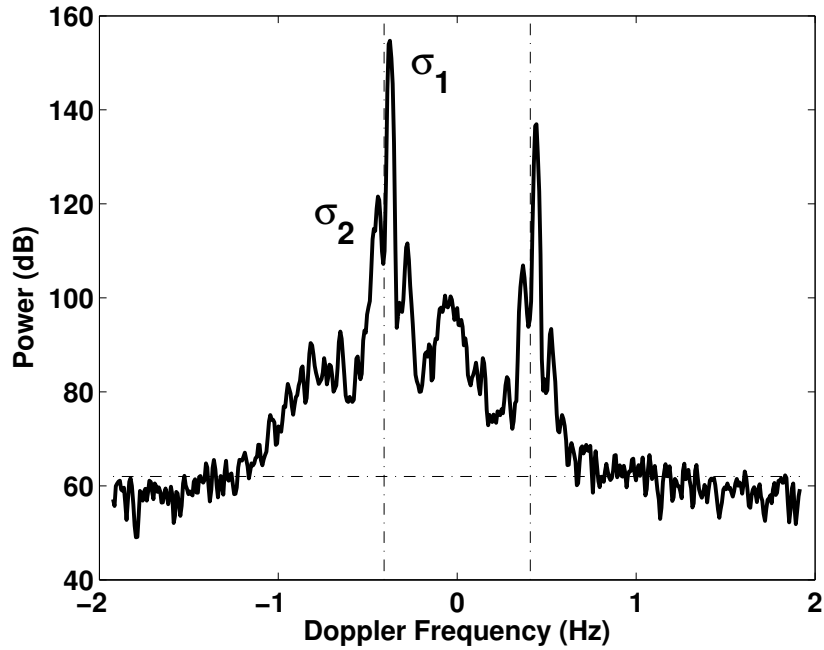
Figure 1.1: An example radar Doppler spectrum. First order Bragg peaks are located at ~ 0.5 Hz [σ_1]. This Bragg frequency for this instrument is 0.409 Hz [dashed vertical lines]; the positive frequency difference between observed and expected Bragg frequency indicates a radial current moving toward the radar. The second order continuum [σ_2] is adjacent to the Bragg peaks. The noise floor for this spectrum is ~ 60 dB [dashed horizontal line].

netic (EM) wave which propagates as a trapped ground wave along the conductive surface of the ocean. The EM wave is scattered off the ocean surface, and some of the reflected energy is incident on the radar's receive antennas. The receive signal is then complex-modulated with the transmit signal to obtain the Doppler spectra (Figure 1.1). The Doppler spectrum is a measurement of variations in the transmitted EM wave due to interactions with the physical environment. It is the fundamental radar measurement, and must be processed via algorithms to yield oceanographic parameters.

The radar measurement is inherently radial. By separating two or more receive antennas in space, their radial measurements can be combined to estimate two-dimensional vector fields (Figure 1.2). The precision of the combined vector field scales with the sine of the angle between the radial vectors, a factor commonly referred to as Geometric Dilution of Precision (GDOP) [Barrick, 2005b] (Figure 1.3).

Range resolution is obtained using coded waveforms, the most common being Frequency Modulated Continuous Wave (FMCW). FMCW linearly sweeps over a frequency band of hundreds
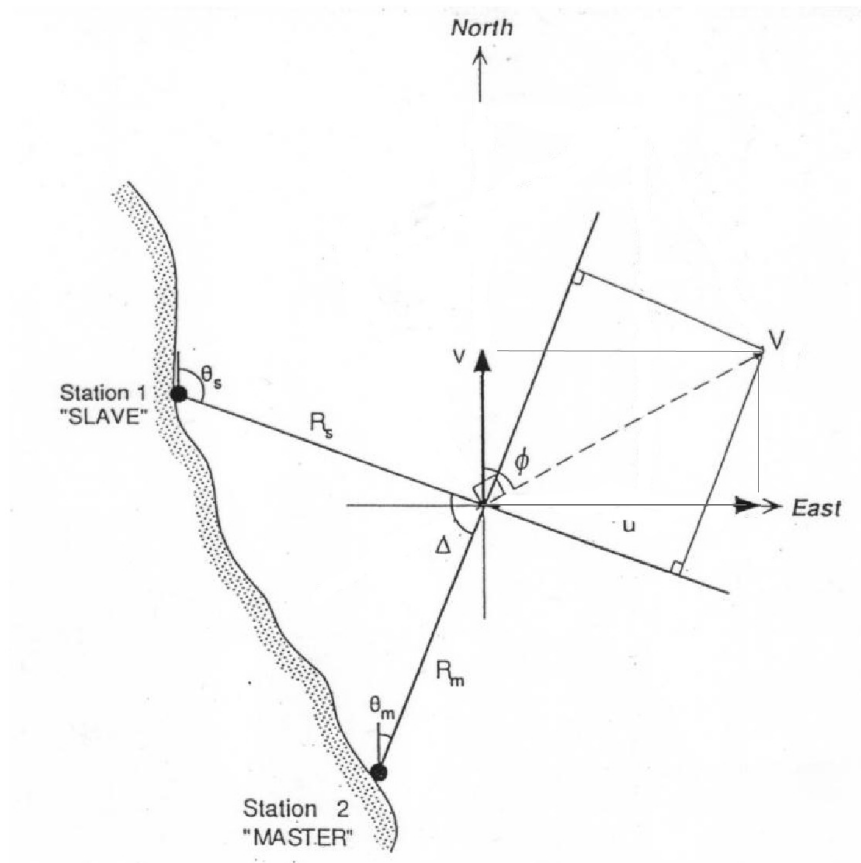
Figure 1.2: From Fernandez et al. [1997]. Schematic for determining the resulting vector currrent from velocity components of two intersecting radials.
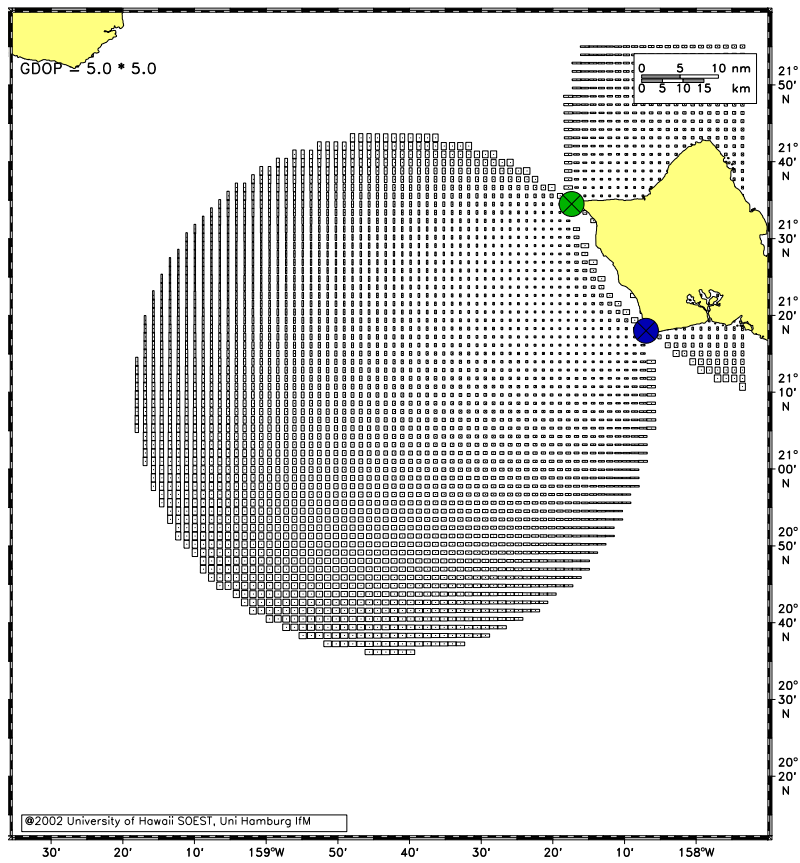
Figure 1.3: Geographic Dilution of Precision for the Oahu sampling grid.

of KHz, with the bandwidth determining the range resolution. Ranges are known from the constant frequency difference between the transmitted and received signals, with maximum range determined by operating frequency and power. Doppler spectral resolution is obtained by repeating the range measurements and performing time-series analysis on the samples. The coherent integration time T determines the frequency resolution $\Delta f = 1/T$ Hz. Consequently, the radial velocity resolution is $\Delta v = \lambda \Delta f/2$ m s^{-1}, where λ is the radar wavelength.

Angular resolution is achieved using multiple receive antennas in varying array configurations. Directivity is defined as a measure of the antenna array's capability to resolve a given direction. The minimum resolvable angle is determined by the Rayleigh criterion $\theta_R = \arcsin \lambda/d$, where d is the antenna separation distance and λ is the EM wavelength. As the desired directivity increases, so does the required number of antennas and length of the array. A more detailed discussion of angle determination is given in the beamforming appendix §C. HF radar is limited in its directivity due to the relatively large EM wavelength (10-100 m for 30-3 MHz), necessitating large arrays.

The incident angle of the receive signal can be inferred from phase differences between multiple antennas. Currently there are two major categories of receive antenna patterns used for oceanographic radars. One is the linear (or phased) array, typically with 8 to 16 antennas spaced one-half wavelength apart. The large number of antennas and length of a linear array provides superior angular resolution, at the disadvantage of considerable spatial size and other logistical requirements. The other category of receive array is the square array. These have the logistical benefit of being compact, but have limited angle-resolving capabilities; typically a 1:1 or 1:2 mapping between range and direction, compared to the full 2-dimensional field of a linear array.

The algorithm used for estimating directional information also depends on the receive array type. Square arrays use direction-finding algorithms to estimate direction, which vary in complexity from simple geometric equations to eigen-decomposition methods. The common feature of all direction-finding algorithms is the incidence angle must be solved for, i.e. it is a dependent variable of the data set. Thus signal components can only arrive from a limited subset of directions; which is a significant and necessary limiting assumption. Linear arrays use beamforming equations; essentially directional weighting functions which apply a phase shift to each antenna, then sum. The beamforming method allows for estimating signal from any specific direction, as the incidence angle is an independent variable.

1.3 Development History

Crombie [1955] was the first to apply radar to oceanographic measurement. He identified coherent scattering from the sea in a radar Doppler spectrum, and realized the difference between the expected surface gravity wave and measured Doppler frequencies was due to surface current velocities. Crombie [1972] examined the coherence between signals received on two closely spaced whip antennas, and found the phase coherence varied with Doppler frequency, implying that signals having different Doppler shifts were coming from different directions, and interpreted this as viewing a uniform current from different aspect angles. This result led to the development of the Coastal Ocean Dynamic Applications Radar (CODAR) [Barrick et al., 1977, Lipa and Barrick, 1983] by the NOAA Wave Propagation Laboratory. The 16-element phased array Ocean Surface Current Radar (OSCR) was commercially developed by Marex Ltd., England. OSCR was used for mapping tidal and residual currents near Britain [Prandle, 1987], and by the University of Miami for coastal observations [Shay et al., 1995, Graber et al., 1996]. A summary of nine OSCR deployments is given in Prandle and Ryder [1985]. In 1996 the HF Wellen radar (WERA) was developed at the University of Hamburg. WERA was designed to allow a range of radar frequencies from 5-45 MHz, range resolution from 2 km to 250 m, and different antenna configurations. WERA utilized new ocean wave directional spectrum algorithms developed by the University of Sheffield, UK. Operational theory for the WERA is described in Gurgel et al. [1999b], and system design in Gurgel et al. [1999a]. See Teague et al. [1997] for a concise review of oceanographic radar development.

This work primarily focuses on HF groundwave radar, where the EM wave propagates along the ocean surface. Skywave is another category of radar requiring mention. Otherwise referred to as Over-The-Horizon (OTH) radar, they function by bouncing dekametric waves off the ionosphere. Originally developed for long-range military surveillance, skywave radar has spatial coverage of $O \cdot 10^6$ km^2 with resolution O 10 km, whereas HF groundwave radar has $O \cdot 10^3$ km^2 coverage and O 1 km resolution. The intermediate reflections of skywave radar introduces additional processing considerations due to signal modulation and noise from the ionosphere - a feature not shared by groundwave HF radar.

1.4 Electromagnetic Scattering Theory

For ocean surface waves of a specific wavelength relative to the incident EM wave, a phase coherent reinforcement (constructive interference) exists in the reflected EM signal (Figure
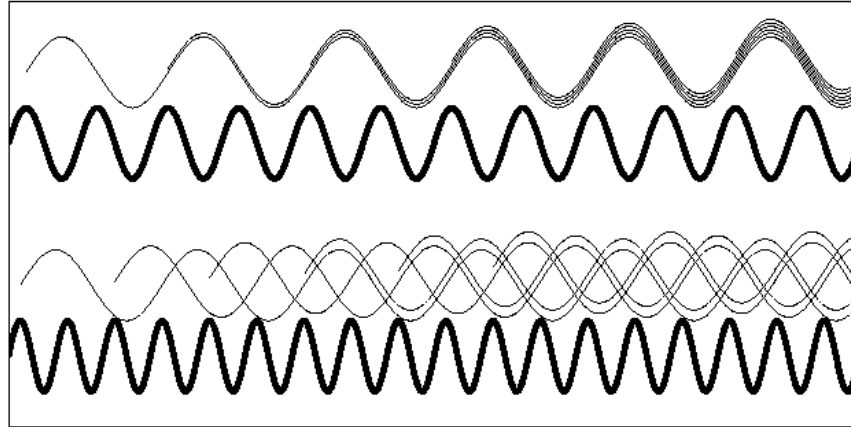
Figure 1.4: Bragg scattering is coherent reflection of the EM wave [thin] by ocean waves [thick] with wavelength $\lambda/2$ [top]. Incoherent reflections, i.e. cancellation of the EM energy, occur for arbitrary ocean wavelengths [bottom].

1.4). This effect is known as Bragg scattering [Bragg, 1913], and the corresponding surface waves are referred to as Bragg waves. In the literature, this effect is also labeled "first order" or "linear", as the EM-ocean wave interaction simplifies to a linear equation. The coherently reflected signal is evident as peaks in the reflected EM spectra, offset by a Doppler shift from the transmit frequency (Figure 1.1). This Doppler shift in the return spectra was first reported by Crombie [1955], who also correctly surmised the celerity of the Bragg waves as the cause for the Doppler shift. From Crombie [1955], the Doppler shift due to Bragg waves is:

$$\Delta f = \frac{c}{\lambda} = \sqrt{\frac{g}{2\pi\lambda}} = \sqrt{\frac{g}{\pi L}} \tag{1.4.1}$$

where Δf is the Doppler shift (Hz), c is the ocean wave celerity (m/s), λ is the ocean wave wavelength (m), and L is radar electromagnetic wave wavelength (m). Crombie [1972] further observed that the phase of the coherence varied with Doppler frequency, implying that signals having different Doppler shifts were coming from different directions, and interpreted this as viewing a uniform current from different aspect angles. Bragg scattering is commonly attributed to waves with one half the EM wavelength; this is true for radars with a backscatter antenna configuration, i.e. co-located transmit and receive antennas. Bistatic, i.e. spatially separated transmit and receive antennas, require a more general expression for Bragg scattering (§A.5).

Barrick [1970] was the first to derive a complete theory for electromagnetic waves scattering from the sea surface using electromagnetic and oceanographic first principles, resulting in an explicit integral representation of the Doppler spectrum in terms of the directional waveheight

spectrum of the sea. Barrick's EM interaction equations are the fundamental basis for the use and interpretation of oceanographic radars. Barrick [1970, 1971a,b, 1972], Derr [1972], Weber and Barrick [1977], Barrick and Weber [1977] are seminal papers for scattering theory. For a review of previous EM scattering research, see Saxton [1964]. The theory considers radiation and propagation of EM waves above the sea, with attention to the effects of a variable sea surface. Barrick [1970] is considered the theoretical confirmation of Crombie [1955], due to the theoretical prediction of Bragg peaks in the Doppler spectrum. The equations are general in that they allow for variable geometries for the transmit and receive antennas. Using only first order theory, the ocean wave directional spectra can be obtained by varying the antenna placement, as discussed by Barrick [1970], numerically investigated by Nierenberg and Munk [1969], and applied by Peterson et al. [1970], Teague [1971]; or by varying the transmit frequency [Crombie, 1970]. A full summary of Barrick's electromagnetic scattering derivations is given in §A.

Further theoretical work by Weber and Barrick [1977], Barrick and Weber [1977] showed that the second order continuum of energy in the Doppler spectrum is produced by two independent effects; an electromagnetic and a hydrodynamic. The electromagnetic component corresponds to radar waves twice scattered from ocean waves, where the geometry of the double scattering causes coherent reflections (Figure 1.5). The hydrodynamic component corresponds to nonlinear surface waves which satisfy the Bragg wavelength [Barrick and Weber, 1977] via the wavevector relation $k_B = k_1 + k_2$ (Figure 1.6,1.7). Both of these components are represented in the scattering equations as second order terms from a perturbation expansion; hence the terminology "second order". Waves of any wavelength may contribute to electromagnetic and hydrodynamic terms, thus information about the entire wave directional spectrum is contained in the second order continuum. As with first order scattering, the necessary condition for both the EM and hydrodynamic components is coherence of the reflected signal. The derivation for both terms is given in §A.6.

After evaluating the effect of sea state on attenuation, Barrick [1970, 1972] continues to a full solution for the electromagnetic field scattered by a moving sea surface. The method employed is a Fourier series expansion for the ocean surface, and a similar expansion for the three components of the EM field above the surface, *with the same wavenumbers*, but with unknown coefficients. These coefficients are solved for by enforcing boundary conditions at the surface. The EM fields at the boundary are expanded in a perturbation series with ordering of terms. A summary of the derivation and its mathematical limitations is given in §A.2. A fundamental result of the direct relationship between the EM scattered modes and ocean wave modes is; the direction of propagation of the scattered EM mode is the Bragg direction required by a periodic surface with the

9
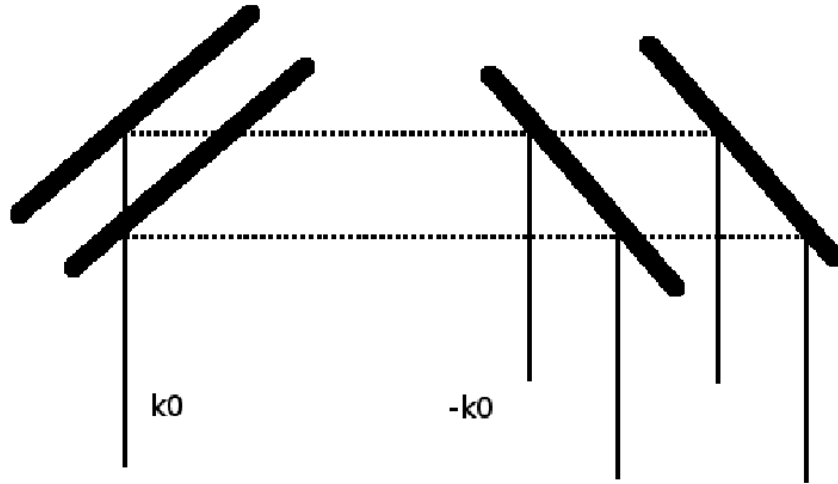
Figure 1.5: Electromagnetic double-scattering. The incident radar wavevector $\boldsymbol{k_0}$ is on the left. Multiple coherent received wavevectors $-\boldsymbol{k_0}$ are on the right.

ocean wavevector. This is the geometric relationship necessary for coherent EM scattering, *to any order*, by the sea surface. By imposing the first order surface gravity wave dispersion relation on the random sea surface, only one ocean wavevector can satisfy the Bragg relation for a given incident EM wavevector. Thus, to first order, Barrick [1970] showed the scattered EM field consists of two impulse functions, i.e. Bragg peaks.

The end result of Barrick [1970] is an expression relating the radar Doppler spectrum energy $\sigma(\omega)$ to the ocean wave height spectrum $W(p, q, \omega)$:

$$\sigma(\omega) = \pi k_0^4 (\sin\theta_s - \cos\varphi_s)^2 W(k_0(\sin\theta_s\cos\varphi_s - 1), k_0\sin\theta_s\sin\varphi_s, \omega - \omega_0) \qquad (1.4.2)$$

where $\sigma(\omega)$ is the range-independent bistatic scattering cross section per unit surface area per radian s^{-1} bandwidth, ω is the Doppler frequency, k_0 is the EM wavenumber, θ_s and φ_s are scattering geometry angles (Figure 1.8), and W is the average wavenumber-frequency ocean surface height spectrum (eqn A.2.2). The wavenumber arguments p, q to $W(p, q, \omega)$ have been replaced by $k_0(\sin\theta_s\cos\phi_s - \sin\theta_i), k_0\sin\theta_s\sin\phi_s$. The latter are precisely the wavenumbers required of a diffraction grating which is to *coherently* scatter a wave incident from θ_i into directions θ_s, ϕ_s.

Equation 1.4.2 is simplified using the deep water dispersion relation, which is:
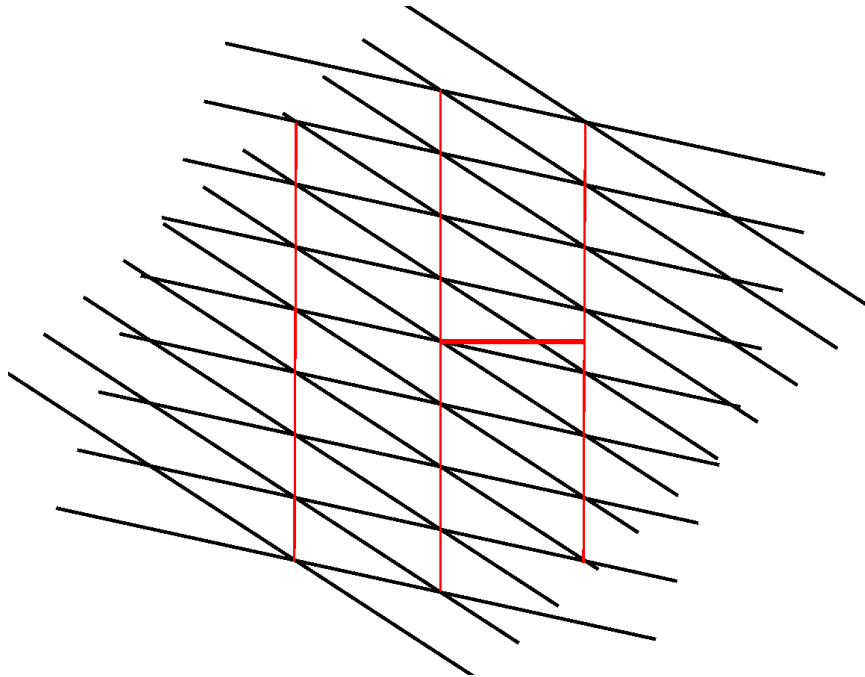
Figure 1.6: Second order hydrodynamic scattering. A nonlinear effect wherein two first order waves [black] interact to produce a second order wave [red]. The second order waves are *not* a simple linear superposition of first order waves. The wavevector geometry must satisy $k_B = k_1 + k_2$, where $k_{1,2}$ are the first order waves and k_B is the second order wave. Crestlines for the $k_{1,2}$ wavefields are shown in black, with k_B shown in red. The second order crestlines connect points of $k_{1,2}$ maximum constructive and destructive interference, i.e. crestline and trough intersects.
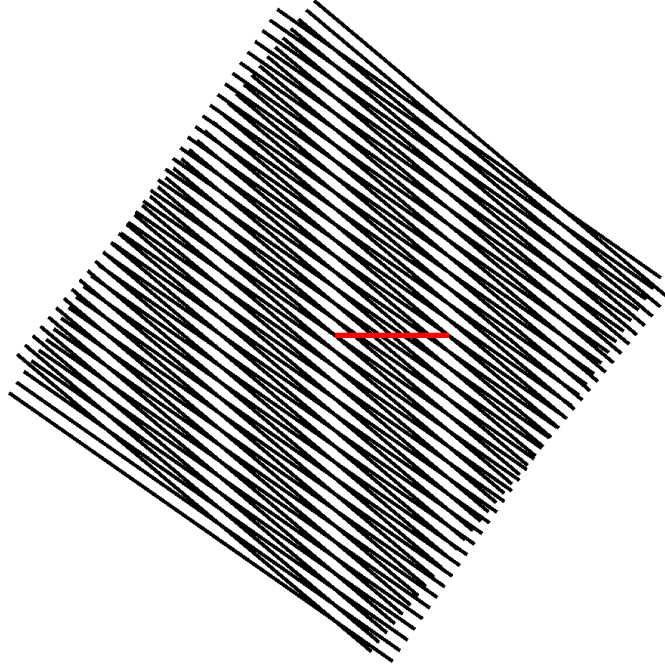
Figure 1.7: Hydrodynamic scattering. Same as Figure 1.6, with k_1, k_2 chosen to optimize the visual Moire' effect.

$$\omega_{g\pm}^2 = \pm g\sqrt{p^2 + q^2} = \pm g\sqrt{(am)^2 + (an)^2} \qquad (1.4.3)$$

The wavenumber-frequency spectrum then becomes:

$$W(p, q, \omega) = 2W_+(p, q)\delta(\omega + \omega_+) + 2W_-(p, q)\delta(\omega + \omega_-) \qquad (1.4.4)$$

where the $\pm$ signs refer to the direction of motion of the waves. Substituting 1.4.4 into 1.4.2:

$$\sigma(\omega) = 4\pi k_0^4(\sin\theta_s - \cos\varphi_s)^2 \left[W_+(p, q)\delta(\omega + \omega_+ - \omega_0)\right.$$

$$\left. + W_-(p, q)\delta(\omega + \omega_- - \omega_0)\right] \quad (1.4.5)$$

Note that the Doppler spectrum consists of two peaks centered at the carrier ω_0 but shifted by an amount:

$$\omega_\pm = \pm\sqrt{gk_0(\sin^2\theta_s - 2\sin\theta_s\cos\varphi_s + 1)^{1/2}} \qquad (1.4.6)$$

These Doppler shifts correspond to the velocites of ocean waves with the proper lengths for Bragg scatter, i.e. $L = \lambda/(\sin^2\theta_s - 2\sin\theta_s\cos\varphi_s + 1)^{1/2}$, where $\lambda = 2\pi/k_0$ is the radio
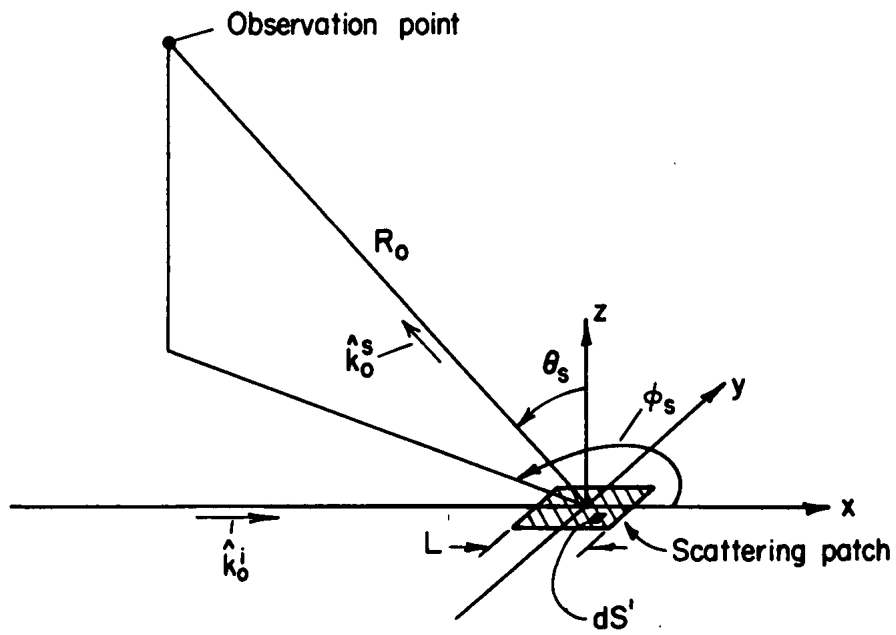
Figure 1.8: from Barrick [1970]. Far-Zone scatter geometry. Square patch of side L, considerably larger than the wavelength λ, but smaller than R_0, the distance from the patch to the observation point, i.e. $\lambda << L << R_0$. $\hat{k}_0^s$ is a unit vector pointing in the desired observation direction, i.e. $\hat{k}_0^s = \sin\theta_s \cos\phi_s \hat{x} + \sin\theta_s \sin\phi_s \hat{y} + \cos\theta_s \hat{z}$.
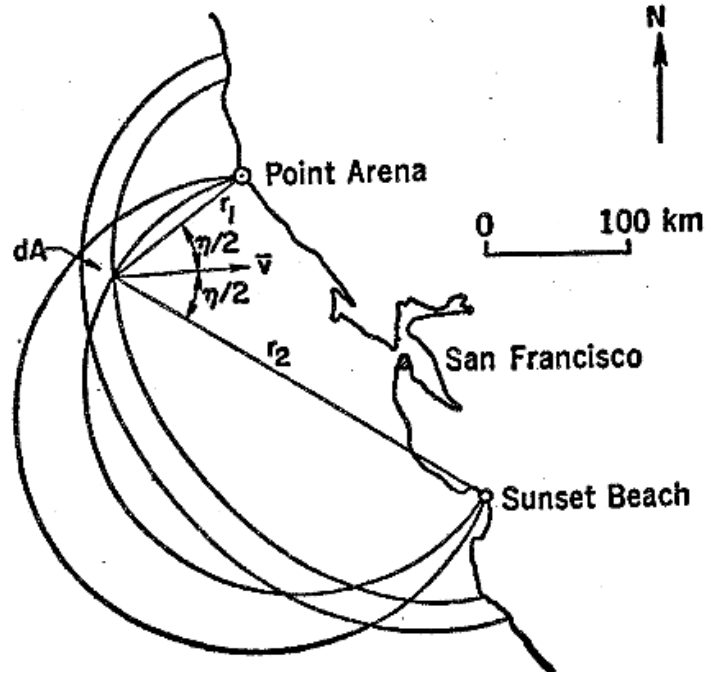
Figure 1.9: From Peterson et al. [1970]. Bistatic radar geometry. The geometrical figures are ellipses, with foci at Point Arena and Sunset Beach, and circles which contain the chord line between Point Arena and Sunset Beach.

wavelength. The frequency shift, $\omega_\pm$, is zero in the forward direction, where $\theta_s \rightarrow \pi/2$, $\varphi_s \rightarrow 0$. It is largest in the backscatter direction, where $\theta_s \rightarrow \pi/2$, $\varphi_s \rightarrow \pi$. Here, $\omega_\pm = \pm\sqrt{2k_0 g}$, and the lengths of the water waves responsible for scattering are the shortest, i.e. $L = \lambda/2$. The Bragg wavevector will bisect the angle included between the Tx and Rx antennas (Fig 1.9).

Using the first order model, the shortest wavelength a radar can sample is the Bragg wavelength, i.e. is controlled by the EM frequency (Eqn. 1.4.6). Longer wavelengths can be sampled using bistatic Tx,Rx antenna separation, i.e. by varying the scattering angle φ_s. Barrick [1970, sec. 4] discusses various bistatic radar configurations for employing the relationship between the Doppler spectrum and the ocean waveheight directional spectrum (Eqn. 1.4.5). An example of this is a bistatic surface-to-surface configuration using omnidirectional transmit and receive antennas (Figure 1.9). A partially complete waveheight directional spectra could be generated using this method and the assumption of a constant directional spectra across the measurement domain.

First order theory limits the explainable portion of the Doppler spectrum to the Bragg peaks and the corresponding data to a one-dimensional sampling of the ocean wave directional

spectrum. As measurements show, there is a significant amount of coherent information throughout the Doppler spectrum (Figure 1.1). Second order theory seeks to relate this region of the Doppler spectrum to measurable properties of the ocean surface directional spectrum.

Hasselmann [1971] first suggested that the Doppler spectrum continuum resulted from higher-order wave-wave interactions. According to this hypothesis, electromagnetic energy is scattered by those combinations of interacting ocean waves that produce the required $\lambda/2$ periodicity on the surface of the sea. Hasselmann based his analysis on a Feynman diagram formalization of the hydrodynamic effects [Hasselmann, 1966], but also included electromagnetic interaction. His analyis predicted symmetrical sidebands on either side of the Bragg peaks, proportional to the waveheight spectrum of the sea. The scattering equation of Barrick and Weber [1977] predicts non-symmetrical sidebands, and multiple second-order peaks due to specific nonlinear wave interactions. It is the prevailing theory in contemporary research, as it correctly predicts spectral characteristics found in observations. Some early confirmation of the Barrick theory is in Tyler et al. [1972]. The theoretical second order Doppler spectrum of Derr [1972] is based on the Weber and Barrick [1977] expressions for second order ocean gravity waves.

Weber and Barrick [1977] derived a more general solution to the nonlinear hydrodynamic equations of motion for ocean waves by extending Stokes [1847] original perturbation analysis. Stokes' solution was for a single gravity wave propagating with a rigid, periodic profile and a constant velocity. Weber's solution allows for a general periodic wave train, i.e. an arbitrary number of distinct gravity wavevectors, with a non-rigid profile and different phase velocities. Weber and Barrick [1977] applied the perturbation solution to find a second order correction to waveheight and a third order dispersion relation correction. Barrick and Weber [1977] show that the general two-dimensional solution [Weber and Barrick, 1977] agrees, within the appropriate limiting cases; with Stokes [1847] for wave velocity and height correction for a single wave; with Longuet-Higgins and Phillips' 1962 phase velocity correction for one wave due to the presence of another colinear wave; and with Tick's 1959 result for the second-order waveheight of a one-dimensional wave train profile.

An important result of Weber and Barrick [1977] is that the waveheights of various orders do not all exist in the same wavevector-frequency domain (Eqn. A.6.3). In general, each order of ocean waves has a different dispersion relation. By nature of the perturbation expansion, second order waves are expressed as double products of first order wave height. Because the second order waves cannot satisfy the first order dispersion equation, they are not "free", i.e. they do not remove energy from the first order waves and cannot propagate freely without the existence of the two first

order waves. The analysis of Weber and Barrick [1977] has constraints to the domain over which the solutions are valid. Energy transfer between waves, between the atmosphere and ocean, and viscosity are neglected. The analysis represents the vertical displacement of the surface as a Fourier series. Thus the spatial and temporal scales should be less than those over which energy transfer processes are important, and large compared to the spatial periods $2\pi/k$ and temporal periods $2\pi/\omega$ of the dominant waves present.

The notation K,Ω is used for second order waves to indicate their exclusion from the first order dispersion relation. The spatial wavenumber of the second order wave K is the vector sum of the wavevectors of the first order waves present. The same is true for the frequencies.

$$K = k + k' \text{ and } \Omega_0 = \omega_0 + \omega_0' \tag{1.4.7}$$

(to lowest order, where $\omega_0 = \sqrt{gk}$ and $\omega_0' = \sqrt{gk'}$).

Barrick and Weber [1977] explain Eqn. A.6.8 for the case of two first order sinusoidal wave trains, where $k, k' = \pm k_a, \pm k_b$. There will be several second order wave trains whose Fourier coefficients $\eta_2(K, \Omega_0)$ are determined by the products of terms in the sum. The four sets of second order waves are:

1) The self effect (second harmonic) second order waves:

$$\text{Wavenumbers } K_{aa} = 2k_a, K_{bb} = 2k_b \tag{1.4.8}$$

$$\text{Frequencies } \Omega_{0aa} = 2\omega_{0a}, \Omega_{0bb} = 2\omega_{0b} \tag{1.4.9}$$

2) The mutual effect second order waves:

$$\text{Wavenumbers } K_{s,d} = k_a \pm k_b \tag{1.4.10}$$

$$\text{Frequencies } \Omega_{0s,d} = \omega_{0a} \pm \omega_{0b} \tag{1.4.11}$$

The analogy used by Barrick and Weber [1977] is Moire patterns in diffraction gratings (Figure 1.7). The self effect waves are parallel to the first order waves, have half the spatial period of the fundamental, but move at the same phase speed. Crestlines of the mutual effect waves connect points of maximum constructive and destructive interference for first order waves, i.e. the first order crest and trough intersects (Figure 1.6). In general, the self effect wave heights are of the same order as the mutual effect waves. But as the number of first order waves N increases, the mutual effect exceeds the self effect term, i.e. N vs. $N(N-1) \approx N^2$ Barrick and Weber [1977]. The heights of the second order waves are small compared to the first order waveheights, e.g. $O(\text{cm})$ second order waves for $O(\text{m})$ first order waves Barrick and Weber [1977].

16

The gravity wave dispersion relation is expressed (to second order):

$$\omega(\boldsymbol{k}) = \omega_0 + \omega_2 = \omega_0(1 + \frac{\omega_2}{\omega_0}) = \sqrt{gk}(1 + \frac{\omega_2}{\omega_0}) \qquad (1.4.12)$$

and hence

$$v_{ph} = \sqrt{gk}(1 + \frac{\omega_2}{\omega_0}) = \sqrt{gk}(1 + \Delta v_{ph}(\boldsymbol{k})) \qquad (1.4.13)$$

This correction term ω_2/ω_0 to the dispersion relation represents the correction to the phase velocity of an ocean wave of length $2\pi/k$. The form of A.6.10 indicates that the change in phase velocity comes not only as a result of the existence of that wave alone, but as a result of the presence of all other waves [Barrick and Weber, 1977]; i.e. the aforementioned "self" and "mutual" effects. Stokes [1847] analysis showed that the nonzero height of the original wave increases its speed slightly, which agrees with the self effect term. The mutual effect term agrees with the analysis of Longuet-Higgins and Phillips [1962]. Barrick and Weber [1977] evaluated the phase speed correction for two-wave interaction. In short, a longer, higher second wave produces a greater phase velocity change on the first wave than a shorter, lower second wave. For parallel waves, the correction term has the same magnitude, but its sign is dependent on their relative directions. Orthogonal incidence results in a phase speed increase, but the magnitude is relatively small compared with parallel incidence (2.78% of the value for parallel incidence) [Barrick and Weber, 1977].

From Derr [1972] the expression for the second order Doppler spectrum in terms of the ocean waveheight energy spectrum:

$$\sigma_{vv}(\omega_D) = 16\pi k_0^4 \int_{-\infty}^{\infty} \int_{-\infty}^{\infty} |\Gamma_T(\boldsymbol{k_1}, \boldsymbol{k_2})|^2 W(\boldsymbol{k_1}) W(\boldsymbol{k_2}) \delta(\omega_D - \omega_1 - \omega_2) dp dq \qquad (1.4.14)$$

where $\sigma_{vv}(\omega_D)$ is the average second order backscatter cross section per unit surface area per rad s^{-1} bandwidth, $\boldsymbol{k_1} = (p - k_0)\hat{x} + q\hat{y}$, $\boldsymbol{k_2} = -(p + k_0)\hat{x} - q\hat{y}$, $k_1 = |\boldsymbol{k_1}|$, $k_2 = |\boldsymbol{k_2}|$, $\omega_1 = \text{sgn}(k_{1x})\sqrt{(gk_1)}$, $\omega_2 = \text{sgn}(k_{2x})\sqrt{(gk_2)}$, $\eta = \omega - \omega_0$ is the Doppler shift from the carrier, $\delta(x)$ is the Dirac impulse function of argument x, and $W(\boldsymbol{k}) = W(k_w, k_y)$ is the directional waveheight spectrum of the ocean. This equation is valid for backscattering at grazing incidence with vertical polarization over a perfectly conducting sea.

The second order electromagnetic contribution Γ_{EM} is found to be

$$\Gamma_{EM} = \frac{1}{2}(k_{1x}k_{2x} - 2\boldsymbol{k_1} \cdot \boldsymbol{k_2})/(\sqrt{\boldsymbol{k_1} \cdot \boldsymbol{k_2}} + k_0\Delta) \qquad (1.4.15)$$

17

where Δ is the normalized impedance of the sea surface.

The second order hydrodynamic effects produce:

$$\Gamma_H = -\frac{i}{2}\left[k_1 + k_2 + (k_1 k_2 - \boldsymbol{k_1} \cdot \boldsymbol{k_2})(1 - 2\eta^2/(\eta^2 - \omega_B^2))(g/\omega_1\omega_2)\right] \qquad (1.4.16)$$

where $i = \sqrt{-1}$ and $\omega_B = \sqrt{(2gk_0)}$ is the first order Bragg Doppler shift. The total Γ used in the integral to account for both types of second order effects is $\Gamma = \Gamma_{EM} + \Gamma_H$.

Equation 1.4.14 shows that a double scatter Bragg process is responsible for the second order Doppler spectrum. The scattered radio wavenumber $-k_0\hat{x}$ is equal to $\boldsymbol{k_1}+\boldsymbol{k_2}+k_0\hat{x}$, where the last term is the incident radio wavenumber. The frequency ω of the scattered field is $\omega_1 + \omega_2 + \omega_0$. For EM second order effects, an ocean wavetrain with wavenumber k_1 scatters the radio energy along the surface to a second wavetrain with wavenumber k_2, which redirects it back toward the receiver (Fig 1.5); the intermediate radio wave can be either propagating or evanescent. For second order hydrodynamic effects (Fig 1.6), two ocean wavetrains produce second order ocean waves with wavevectors $\boldsymbol{k_1} \pm \boldsymbol{k_2}$; these latter ocean waves are not freely propagating because they do not satisfy the first order gravity wave dispersion relationship [Derr, 1972]. One of the two integrals can be done in closed form because of the Dirac function in the integrand. The remaining integration is done numerically because of the complex form of the integrand.

The magnitude of the second order Doppler sidebands are dependent on sea state. These sidebands contain continuous integrable singularities, i.e. spectral peaks, at Doppler frequencies $\sqrt{(2)}f_B$ and $2^{3/4}f_B$. The $\sqrt{2}$ singularity is due to both electromagnetic and hydrodynamic second order effects. The electromagnetic component is from ocean waves of length $L = \lambda$ (rather than $\lambda/2$). The hydrodynamic component is from a second spatial harmonic with length $L = \lambda$. The $2^{3/4}$ singularity is due to a "corner reflector" electromagnetic effect. This occurs when two sets of first order scattering ocean waves pass through $45°$ with respect to the propagation direction [Derr, 1972].

The two-dimensional nonlinear integral equation 1.4.14 which gives the Doppler spectrum as a function of the directional ocean wave spectrum, [Barrick, 1970, Derr, 1972], is the core equation used in further derivations of wave parameters. A further discussion of its properties is given in §3.5.

18

1.5   Previous Research

High frequency ocean radar measures EM waves reflected from the ocean surface. This signal results in a Doppler spectrum comprised of two large Bragg peaks and a continuum of second order energy. Several ocean parameters can be inferred from this information; surface currents, surface wind direction, vertical current shear, rms wave height, the scalar, and the directional ocean wave spectrum.

1.5.1   Currents

The most robust radar-derived estimate is surface current velocities. Surface currents within the orbital depth decay of the ocean Bragg waves will modify their apparent celerity. This additional celerity is measured as a difference from the expected Doppler shift in the radar spectrum. The success of this method lies in its simplicity and direct relationship to the received signal. The strongest feature of the Doppler spectrum are the Bragg peaks, typically at 20-30 dB above the second-order continuum (Heron and Heron, 1998). Furthermore, only the frequency location of the Bragg peaks is required, whereas phase and amplitude are relatively more sensitive to internal and external noise sources. Methods for extracting the frequency of the first order peaks are discussed in §2.2.

This method has been widely used to map sea surface currents and investigate physical interactions. Stewart and Joy [1974] used a multifrequency radar on San Clemente Island to measure the vertical current shear at two bearings. Heron et al. [1985] operated a narrow-beam radar inside the Great Barrier Reef, achieving 5 cm s^{-1} accuracy. OSCR-derived tidal currents have been compared to near-surface current measurements [Prandle, 1987] and modeled velocities [Prandle and Ryder, 1989]. Statistical analysis found the standard error of OSCR to be less than 4 cm s^{-1}. Shay et al. [1995] compared radar currents to subsurface ultrasonic current meters. Regression analysis indicated a bias of 2-4 cm s^{-1} and slope of $O(1)$, with periods of high and low correlation. Graber et al. [1996] compared OSCR currents to interferometric synthetic aperture radar INSAR, shipboard measurements, and buoys. Kosro et al. [1997] found OSCR and ADCP currents with correlations of ~ 0.8 and rms differences of ~ 15 cm s^{-1}. Shay [1997] found radar current oscillations within the internal wave continuum from the buoyancy to the inertial frequencies. Chavanne et al. [2007] compared tidal currents in the Adriatic Sea to model results, and investigated the interactions between mesoscale currents and internal tides [Chavanne, 2007].

19

A relatively new development is the measurement of vertical current shear via radar [Shrira et al., 2001]. They demonstrate the ability to measure depth integrated currents to three different depths; employing the known ocean wavevectors of the second order singularities, i.e. $2^{1/2}f_B$ and $2^{3/4}f_B$ second harmonics and corner reflections, in conjunction with the Bragg wavevector.

1.5.2 Winds

The surface wind direction can be inferred from radar spectra. The method for estimating wind direction from radar spectra was originally developed by Long and Trizna [1973] for use with skywave radar. The experiment was conducted at the U.S. Naval Research Laboratory, and generated wind maps for large areas of the Atlantic. Stewart and Barnum [1975] evaluated the accuracy of that technique. The wind direction method of Long and Trizna [1973] has since been applied with success to ground wave HF radar.

The Long and Trizna [1973] method is as follows: If the wind has remained constant over enough time and fetch, the surface wave energy will be in equilibrium with the wind, and can be modeled as a 2-dimensional cardiod distribution as a function of angle with respect to wind direction [Longuet-Higgins et al., 1963]. Longuet-Higgins et al. [1963] suggested the form:

$$G(\theta) = A \cos^s(\theta/2) \qquad (1.5.1)$$

where $G(\theta)$ represents the angular distribution of wave energy, A is a constant, θ is the angle from the direction of maximum wave energy, i.e. the angle of the wind, and s is a spreading parameter. A is a constant required for the normalization $\int_{-\pi}^{\pi} A \cos^s(\theta/2)d\theta = 1$ for different values of s.

The Bragg ratio R_B is defined as the ratio of energy in the approaching to receding Bragg peak [Long and Trizna, 1973]. Bragg peaks with a positive Doppler shift are due to waves approaching the radar, whereas the negative Bragg peak is due to receding waves. The magnitude of the Bragg peak is directly related to the energy within the approaching and receding Bragg waves (Figure 1.10). Following Fernandez et al. [1997] the Bragg ratio is:

$$R_B = B_+/B_- \qquad (1.5.2)$$

where B_+ and B_- are the positive and negative Bragg peaks, respectively. If the wind vector is directed towards the radar, the majority of the Bragg waves will be propagating towards the radar, causing the Bragg ratio to be positive and large. If the wind vector is perpendicular to the radar direction, then $B_+ \sim B_-$, and the Bragg ratio will be near zero.
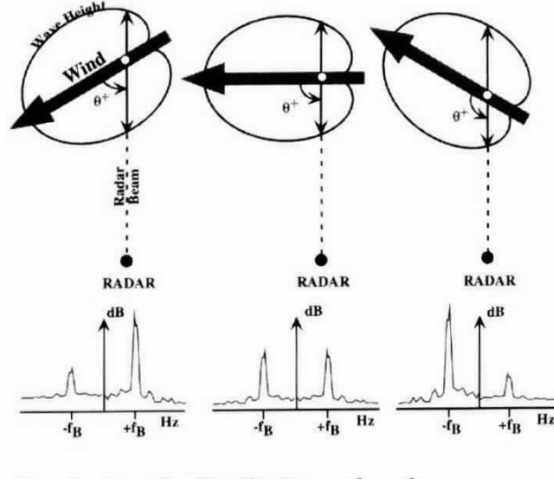
Figure 1.10: From Fernandez et al. [1997]. Sample distributions of surface wave energy as a function of angle relative to the wind direction for cases with wind blowing toward (left), at right angles to (middle), and away from (right) the radar look direction. Sample backscatter spectra below show relative heights of the approaching (+) and receding (-) Bragg peaks for each case and θ^+ denotes the angle between the wind and the approaching wave directions.

Define θ^+ and θ^- as the angles between the wind vector and the approaching and receding Bragg waves, respectively. Substituting the cardiod distribution of 1.5.1 into 1.5.2 yields:

$$R_B = \frac{\cos^s\left(\frac{\theta^- - 180°}{2}\right)}{\cos^s(\theta^-/2)} = \tan^s(\theta^-/2) \tag{1.5.3}$$

There is a left-right ambiguity in 1.5.3 that can be resolved using observations from two radar stations. Equation 1.5.3 can be inverted for θ^- if a value for s is assumed; $\theta^- = 2\arctan(R_B^{1/s})$

Two fundamental assumptions allow for inference of surface wind direction from radar spectra. The first is that the Bragg waves are locally generated by the wind. That is, a stationarity in space and time is assumed. Bragg wave propagation and evolution as a function of wind history and outside energy sources is not considered. The method of Long and Trizna [1973] assumes the ocean Bragg wave energy are proportional to the spectral power of the Bragg peaks, following Barrick [1970]. This implies a 1:1 instantaneous mapping of wind direction to Bragg wave amplitude and direction. The second assumption is *a priori* knowledge of the Bragg wave directional spreading function. The accuracy of radar-derived wind direction estimates depends on the model used, spatial and temporal variability in the measurement cell, the GDOP, antenna beamforming, and noise levels.

21
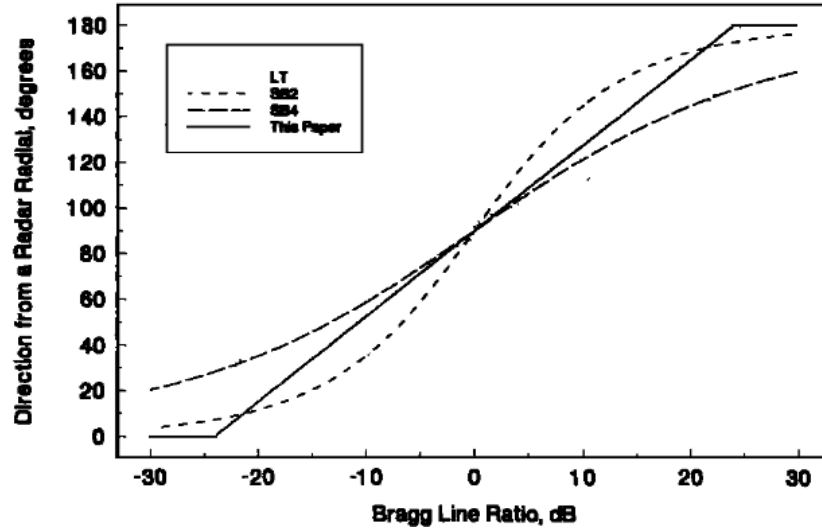
Figure 1.11: From Harlan and Georges [1994]. Comparison of several semiempirical models for the dependence of the Bragg ratio R_B on wind direction, measured from the radar look direction. LT indicates the Long and Trizna [1973] model. SB2 and SB4 indicate the Stewart and Barnum [1975] model with $s = 2, 4$ for the spreading function

The accuracy of the stationarity assumption is largely dependent on the Bragg wavelength. Ocean waves of different wavelengths respond differently to changes in wind speed and direction. To assume local generation, the Bragg waves must be significantly damped before entering the next grid cell, and they must quickly reach equilibrium with a turning surface wind. Masson [1990] studied directional wave spectra during turning wind events, and estimated relaxation coefficients as a function of wave frequency. van Vledder and Holthuijsen [1993] give equations for calculating the Bragg wave group speed and damping rate. Thus energy propagation between range cells, and response time for shifting winds can be evaluated. For example, Harlan and Georges [1994] calculated a 36 min response time for 10 m Bragg waves under an 8 m s^{-1} wind.

The exact form of the directional spreading function is unkown, and observations indicate that a specific functional form is difficult to justify [Phillips, 1966, Nierenberg and Munk, 1969]. Assumptions of unimodality or symmetry are not valid [Masson, 1990]. Higher wind speeds produce more directional spreading [Stewart and Barnum, 1975]. At low wind speeds, directional variability complicates measurement Pierson Jr. [1990] and Gilhousen [1987]. For a given Bragg ratio, the estimated wind direction can vary by $30°$ depending on the choice of spreading model (Figure 1.11). The reader is referred to Banner and Young [1993] for an evaluation of wind-wave models, and Harlan and Georges [1994], Wyatt [2001] for their application to radar measurements.

Donelan et al. [1985] conducted a detailed study of deep water wind-wave evolution using an array of 14 wave gauges. They proposed a directional spreading function *near the spectral peak* of:

$$D(\theta, k) = \text{sech}^2 \beta(\theta - \theta_w) \qquad (1.5.4)$$

where k is the wavenumber, θ is the polar direction, and θ_w is the wind direction. They found the primary variation of β was on k/k_p, where k_p is the wavenumber of the spectral peak. At frequencies above $1.6 f_p$, the directional spread becomes noisy.

Maresca and Georges [1980] used a $\cos^s(\theta/2)$ spreading model, and found less accurate results for large s, i.e. highly directional wave distributions. Harlan and Georges [1994] identified an operational limitation wherein the measurable Bragg ratio did not exceed a maximum value, i.e. an upper limit to the directionality of the spreading function. This was also noted by Gurgel et al. [2006]; observed ratios did not exceed ± 20 dB, corresponding to an inability to measure wave directions between ± 15 or ± 165 degrees (the chosen $\cos^s$ model requires a peak Bragg ratio of ± 25 dB). Wyatt [2001] proposed using the Donelan et al. [1985] $\text{sech}^2 \beta(\theta)$ model, as it does not give infinite values for angles near $0°$ or $180°$. It can be adjusted to give the same slope as the $\cos^s$ model with $\beta = 0.7$ or to cover the observed Bragg ratios of $\pm \approx 20$ dB with $\beta = 1.0$. Gurgel et al. [2006] found the best fit to buoy measurements with $\beta = 0.8$.

Numerous studies have compared radar-derived wind direction estimates to alternative measurements. [Stewart and Barnum, 1975] found the Bragg ratio method accurate to within $16°$ compared to shipboard anemometer measurements. Using the same WARF radar, Maresca and Georges [1980] found wind direction agreement of $7°$ compared to a National Data Buoy Office (NDBO) buoy. Shearman and Wyatt [1982] describe the results of mapping winds during the JASIN experiment. Heron et al. [1985] found agreement of $\pm 10°$ within a swell-shadowed region of the Great Barrier Reef using *in-situ* measurements. Using a OTH radar, Harlan and Georges [1994] accurately recreated ocean-basin scale wind fields ($18 \cdot 10^6$ km^2) using an empirical fit to NMC model and buoy data, yielding a rms error of $\sim 33°$ (Figure 1.12). Fernandez et al. [1997], Wyatt [1997] compared wind direction estimates obtained from the OSCR radar at the DUCK facility to offshore moored buoys and a research pier station (Figure 1.13). Spatial maps of wind direction have shown variations over horizontal scales of a few kilometers, and resolved the passage of a sharp front [Fernandez et al., 1997].

Vesecky et al. [2002] used a partial least squares (PLS) method combined with *in-situ* measurements to add magnitude to wind estimates from a multifrequency radar. This is a unique
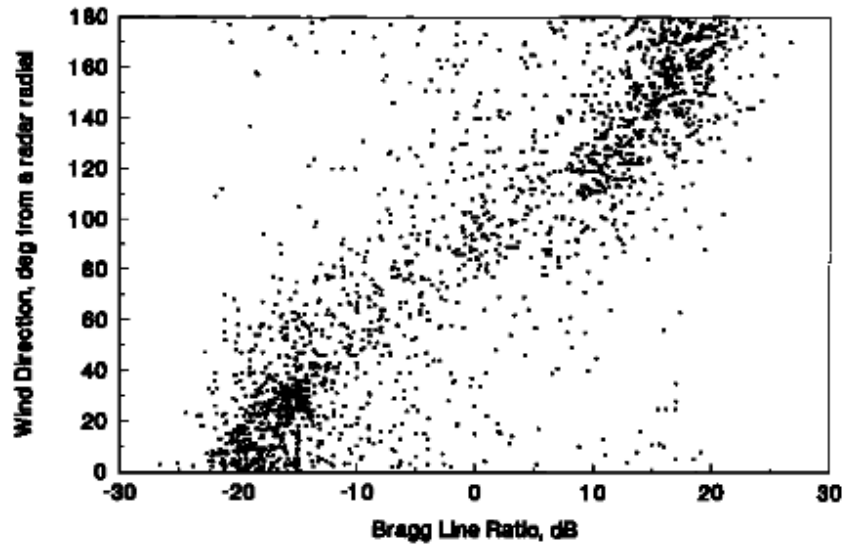
Figure 1.12: From Harlan and Georges [1994]. 1900 OTH radar measurements of the Bragg ratio R_B plotted against the magnitude of the NMC or in situ wind direction, measured relative to the direction of arrival of the radar ray. Each radar measurement falls within 100 km and 1.5 hours of the corresponding model or *in-situ* measurement. The correlation coefficient is 0.69.
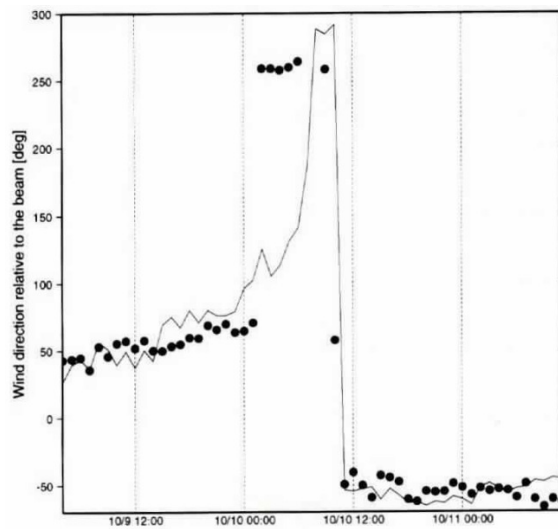
Figure 1.13: From Fernandez et al. [1997]. Wind direction relative to the master radar site measured at a wave buoy off Duck, North Carolina in October 1994 (solid) together with estimates from the HF radar (symbols) for a 2-day period.

addition to the Long and Trizna [1973] method which cannot infer wind magnitude. The PLS technique uses linear regression to fit observations to a statistical model, and achieved a standard error of prediction of $\sim 40°$ and $r^2 = \sim 0.45$.

1.5.3 Waves

Using electromagnetic and hydrodynamic theory, Barrick [1977] derived an integral expression for the root-mean-square waveheight (hereafter H_s) as a function of the Doppler spectrum:

$$H_s{}^2 = \frac{2 \int_{-\infty}^{\infty} \sigma_2(\omega_d)/W(\nu)d\omega_d}{k_0^2 \int_{-\infty}^{\infty} \sigma_1(\omega_d)d\omega_d} \tag{1.5.5}$$

$$W(\nu) = \frac{8}{k_0^2} \overline{|\Gamma|^2} \tag{1.5.6}$$

where $\nu = \omega_d/\omega_B$ is Doppler frequency normalized to the Bragg frequency. σ_1 is the first order power (integrated power spectral density), σ_2 is the second order power, ω_d is the Doppler shift frequency (Hz), ω_B is the Bragg frequency (Hz), k_0 is the incident EM wavenumber (rad/m), and W is a dimensionless weighting function. The total coupling coefficient Γ is defined in Equations 1.4.15,1.4.16. The assumption of a mean weighting function $\overline{|\Gamma|^2}$ over all directions allows 1.5.5 to be independent of direction, and thus H_s can be estimated from the radar spectrum alone, without *a-priori* knowledge of the sea state. Estimation of the first and second order powers σ_1,σ_2 from the measured Doppler spectrum is discussed at length in subsequent sections.

There are three sources for error in the radar-derived H_s estimate. They include; theoretical error, statistical i.e. sampling error, and noise. The first two can be calculated, whereas noise error can only be identified and avoided. Theoretical error arises from use of the EM scattering equations and their inherent inaccuracies and limitations. Theoretical analysis herein will be limited to the H_s equation 1.5.5. For inter-comparison of various radars the relative standard error (RSE), i.e. the standard deviation of the measurements normalized by the mean, will be referred to. This compensates for increased measurement variation due to greater waveheights.

There are three limitations to the mathematical validity of the EM scattering equations [Barrick, 1970]. 1) Small amplitude approximation: the sea surface height ζ above the mean plane is small in terms of the EM wavelength. 2) Small slope approximation: the sea surface slope $\nabla\zeta$ is small. 3) The medium is highly conducting. Conditions (1) and (3) are not a concern for HF radar. The shortest wavelength for HF is ~ 10 m, thus the small amplitude (1) approximation is satisfied. Sea water satisfies (3) below UHF (300 MHz). Condition (2) is a documented limitation, often

25

referred to as the "saturation limit", wherein large waveheights cause the second order continuum to be indistinguishable from the first order Bragg peaks [Lipa and Nyden, 2005]. The small slope assumption requires $k_0 H_s < 4$. Wyatt et al. [1999] noted an upper limit of $H_s = 7.1$ m for a 27.65 MHz radar, i.e. $k_0 H_s = 4.11$. The empirical method of Gurgel et al. [2006] failed near this limit, due to spectral merging of the first and second order regions. The saturation limit is not only a mathematical limitation, but a physical limitation to radar operation.

Barrick [1977] tested 1.5.5 using the Phillips [1966] synthetic wave model, and concluded the formulas were only weakly dependent on the incident radar-wave direction, *above a certain $k_0 H_s$ limit*. Synthetic testing showed poor accuracy below $k_0 H_s < 0.1$, indicating a theoretical limit. Above $k_0 H_s > 0.3$, RSE for H_s was 22.7% [Barrick, 1977]. Observations of a 7-10 MHz radar operating over a 10 month period yielded poor accuracies below 1 m H_s [Wyatt et al., 2006]. This corresponds well to the lower theoretical limit of 0.7 m.

Maresca and Georges [1980] investigated two semi-empirical methods for estimating wave parameters from the radar data; the rms waveheight H_s, and the scalar wave spectrum. Both methods involved generating a range of synthetic ocean wave directional spectra, passing them as inputs to the second-order EM scattering model of Weber and Barrick [1977] (Eqn. A.6.17), and using least-squares regression to optimize the fit between theoretical and observed Doppler spectra. The linearized form of 1.5.5 agreed well with nearly all synthetic spectra evaluated (Figure 1.14). The H_s equation did not agree with the highly directional, i.e. $s = 8$, wave model. This was explained as an increased sensitivity of the second-order energy to the radar look direction θ [Maresca and Georges, 1980]. Similarly, the estimated scalar wave spectrum was found to be highly dependent on the radar-to-wind direction, and the wave directional distribution.

Barrick [1980] derived the statistical properties of the H_s equation. The sea surface height, and consequently the received radar voltages, are taken to be Gaussian [Derr, 1972]. Thus the Fourier-transformed power spectra at each spectral point is a χ^2 random variable with two degrees of freedom. The division of sums of χ^2 power spectral samples produces a F-distributed random variable [Barrick, 1980]. In this context, the H_s waveheight (Eqn. 1.5.5) is expressed in the form of a power law:

$$k_0 H_s = C q^p \tag{1.5.7}$$

where k_0 is the radar wavenumber, C is a constant, q is the quotient of spectral sums, i.e. second order to first order energy, and p is by theory $1/2$. By the aforementioned argument, q is F-distributed.

Figure 1.14: From Maresca and Georges [1980]. The ratio of the of the total second-order to first-order power, R_σ, plotted against $k_0 h$ calculated from synthetic Doppler spectra for four forms of the ocean wave spectrum

For a radar which collects K sequential spectra in time at a fixed range, the best possible accuracy is obtained by simply averaging all K spectra Barrick [1980]. It makes no difference how the timeseries are divided into individual spectra. The situation becomes more complicated when one desires to average consecutive spectra in range or time, as individual spectra will have varying path loss and system gain, i.e. signal-to-noise ratios. These gain factors must be removed prior to averaging, via the second-to-first order energy quotient q.

The obvious method is to average the quotients q for each power spectrum, as this cancels the variable gain factors; $k_0 h = C \langle q \rangle^p$. But for $0 < p < 1$, both the error and bias are improved by averaging the quotient to its pth power; $k_0 h = C \langle q^p \rangle$ [Barrick, 1980]. Furthermore, when the denominator of q has many samples N, the standard deviation of q improves [Barrick, 1980]. This is not the case for the H_s calculation, as relatively few Bragg peak spectral points comprise the denominator. By averaging the reciprocated quotient q^{-1}, the error improves. Thus, the RSE and bias are minimized by averaging the reciprocated quotient to the pth, i.e.

$$k_0 h = C \langle q^{-p} \rangle^{-1} \tag{1.5.8}$$

The normalized standard deviation σ, i.e. RSE, and waveheight bias h_b/h due to sampling are given as:

$$\sigma(h) = \sigma(q^{-p})/(\langle q^{-p} \rangle^2 \sqrt{K}) \tag{1.5.9}$$

$$h_b/h = \langle q^{-p} \rangle^{-1} \tag{1.5.10}$$

where K is the number of spectra averaged together, h_b is the calculated H_s, and h is the true H_s.

In summary, the best H_s accuracy is achieved by simply averaging equal-gain spectra. For unequal-gain spectra the gain must be eliminated via a normalization, e.g. quotient, prior to averaging. In this case, accuracy always increases by having more samples, i.e. higher frequency resolution, i.e. no incoherent averaging of spectra [Barrick, 1980].

Multiple researchers have reported on observed error in radar H_s measurements (Table 1.1). Using a 20 kW skywave radar, Maresca and Georges [1980] compared radar H_s to a National Data Buoy Office buoy for waveheights of 0.3-0.8 m. Using eqn. 1.5.9, they calculated H_s RSE of 3.3% compared to observations of $\sim 15\%$ (N=84). They attributed the primary difference to a lack of normalization prior to spectral averaging, i.e. compensating for path gains. Heron et al. [1985] compared a 30 MHz ground wave radar to a Datawell waverider buoy within the Great Barrier Reef for a 24 hour period. Root-mean-square deviations were 0.15 m for 0-1 m waveheights.

Table 1.1: Comparison studies of radar to buoys

	radar	λ_B (m)	Observed H_s(m)	Correlation	σ
Maresca and Georges [1980]	WARF*	9-15	0.3-0.8		7,17%
Heron et al. [1985]	COSRAD	5	0-1		$> 15\%$
Heron et al. [1998]	OSCR	6	0-1	0.97	20%
Wyatt and Green [2002]	PISCES,WERA	6-15,10-25	0.5-4	0.94	10.5%
Wyatt et al. [2003]	WERA		1-8	0.94	16.6%
Wyatt et al. [2005]	OSCR		0.5-3	0.88	
Wyatt et al. [2006]	PISCES	15-21	0.5-8	0.90	33.8%

λ_B: Bragg wavelength, σ: normalized standard deviation, i.e. relative standard error
* skywave radar

Deviations at these low waveheights were attributed to noise in the second order part of the Doppler spectrum. Heron et al. [1998] compared the OSCR radar to a NOAA directional wave buoy. Radar measurements were averaged over 20 km^2 corresponding to N=15 individual spectra. RSE was $\sim 20\%$ for observed waveheights of 0-1 m, with a correlation of 0.97. Using a unique algorithm method, Essen et al. [1999] compared the WERA radar to 34 days of directional waverider buoy data. Measures of first order variance were highly correlated (r= 0.8-0.9) for some regions of the spatial field. Good data was obtained to a range of 30 km, with some degradation due to external noise. Caires [2000] reported decreased accuracies for the OSCR radar away from the center of measurement region. Compiling data from the Eurorose, SCAWVEX, and SHOWEX experiments, Wyatt and Green [2002] reported a mean correlation coefficient of 0.94 between radar and buoy measurements for the PISCES and WERA radars, and a RSE of 10.5% (N=9169). The main limitations to H_s accuracy were scattering theory, noise sources, and antenna sidelobes [Wyatt and Green, 2002]. It was further noted that strong, directional external noise in the daytime decreased spatial coverage across all directions. Wyatt et al. [2003] compared the WERA and WaMoS radars to waverider buoys at 3 different locations, and to the WAM model. H_s waveheights ranged from 1-8 m. The WERA had a mean correlation of 0.94 to the buoys, and a mean RSE of 16.6%. Wyatt et al. [2005] evaluated the OSCR radar with two buoys and concluded the dataset was unsuitable for wave measurements, despite a mean H_s correlation coefficient of 0.88. Primary limitations were the OSCR hardware, deployment configuration, poor beamforming, and signal to noise ratios. Wyatt et al. [2006] reported on 10 months of operational data from the PISCES radar. The lower operating frequencies of 7-10 MHz combined with high transmit power (up to 1.2 kW) allows the PISCES to achieve wave measurements up to ranges of 120 km. A useful lower limit of 2 m H_s was noted for radar wave measurements, attributed to the longer Bragg waves.

Chapter 2

Methods

2.1 WERA radar and directional wave buoy

The reference data set for this study comes from a Datawell MarkIII directional waverider buoy. Data were furnished by the Coastal Data Information Program (CDIP), Integrative Oceanography Division, operated by the Scripps Institution of Oceanography. According to the manufacturer, the buoy is accurate to 0.5% of the measured waveheight value. The buoy is located approximately 4.3 nm west of Sunset Point, Oahu, Hawaii, and is hereafter referred to as the CDIP buoy. Archived ocean wave parameters include scalar spectral energy, directional Fourier coefficients, significant wave height H_{m0} from the zeroth moment of the energy spectrum, peak period T_p, mean direction at the peak period D_p, and the average period T_a (m_0/m_1 spectral moments). The buoy spectra are from a 2048 point timeseries at 1.28 Hz, incoherently averaged to a 64-point spectra with variable bandwidth (Figure 2.1). Using the Maximum Entropy Method (MEM) [Lygre and Krogstad, 1986], the directional Fourier coefficients and energy spectra were used to generate directional spectra (Figure 2.2).

The radar data set used for this study was collected during the Hawaiian Ocean Mixing Experiment (HOME) between 2000 and 2002. The instrument used was the HF Wellen radar (WERA), developed at the University of Hamburg. Two radar sites were employed near the extreme North-South points of the western coast (Figure 2.3). The northern site was located at the top of the Waianae mountain range near Kaena Point. The southern site was located near the Koolina Resort. Hereafter the sites will be referred to as Kaena and Koolina. The WERA operated at a transmit frequency of 16.046 MHz, 102.5 km maximum range, 1.5 km range resolution, and 7.2 degree angular resolution. Corresponding to this operating frequency, the Bragg scattering waves are 9.38 m wavelength, wavenumber $k_0 = 0.67$ rad s^{-1}, with 2.45 s period. The data was interpolated from a
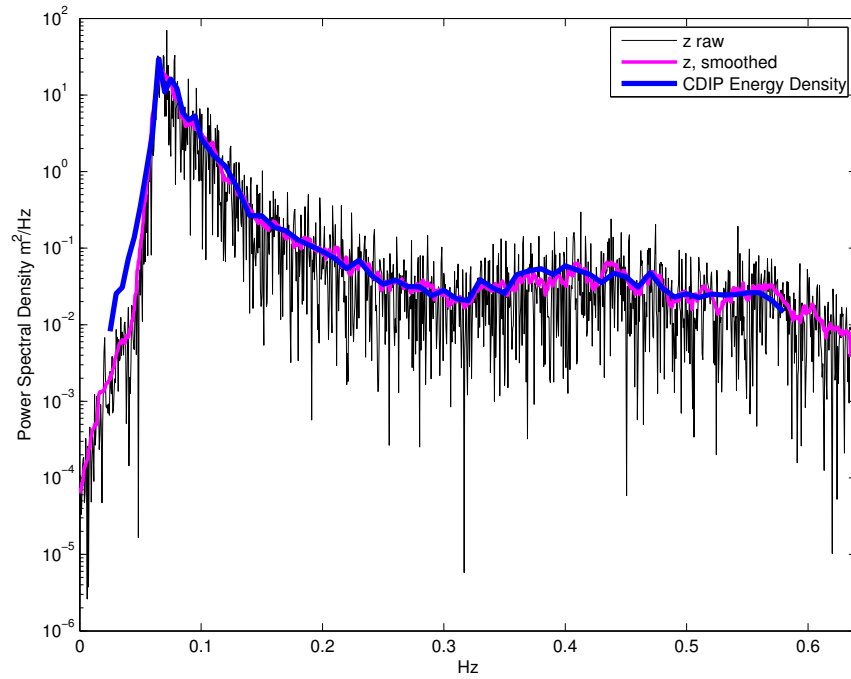
Figure 2.1: An example spectrum from the Waimea CDIP buoy. Incoherent averaging of the raw spectra [black] is used to improve the SNR of the data product [blue], at the cost of reduced frequency resolution. Similar results are achieved using a Hamming window [pink].
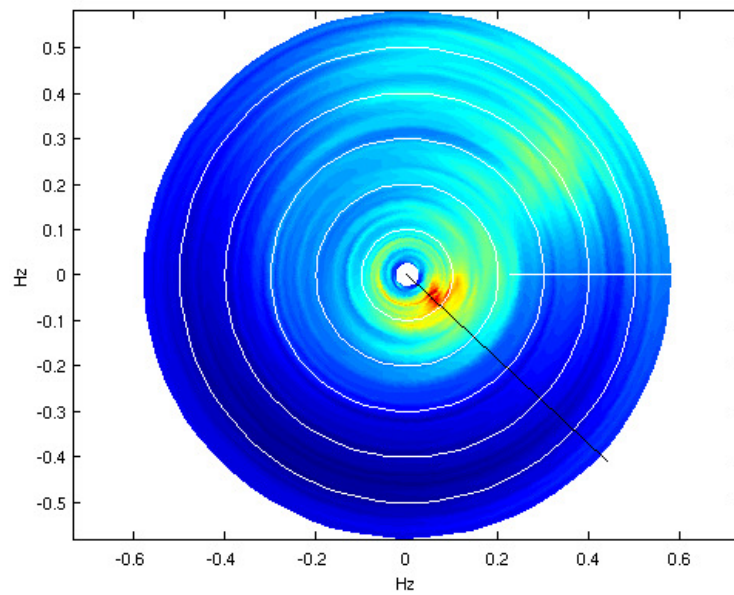
Figure 2.2: An example directional spectrum from the Waimea CDIP buoy. The polar plot is aligned with True North, with frequency increasing radially. Energies are indicated in the direction they are propagating *towards*, i.e. the peak energy at $135°$ is moving south-east [black line].

polar to cartesian coordinate system with 2 km resolution in the horizontal and vertical, with 80x90 sample points respectively (Figure 2.3).

A relatively short 21-day subset of the available data was chosen for analysis. This period coincides with previous research of tidal and mesoscale currents [Chavanne et al., 2007, Chavanne, 2007] using the same data set. Both radar stations were operational during this period, corresponding to 1221 paired time samples (Figure 2.4). Two large swell events occurred during the study period (Figure 2.5).
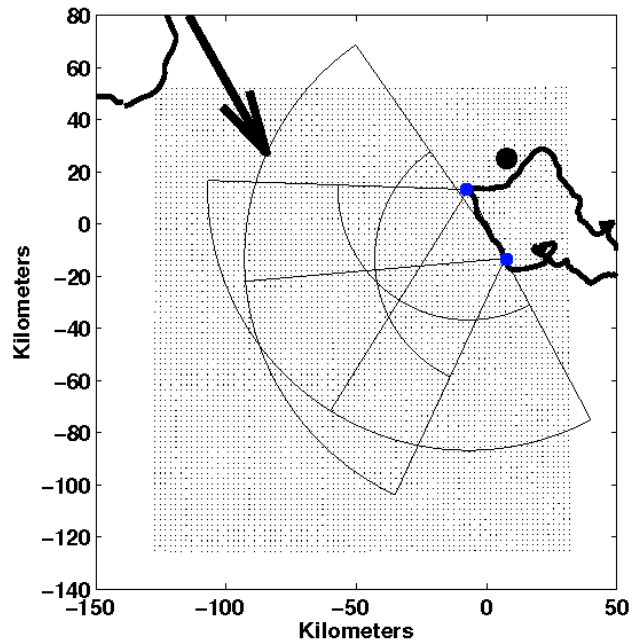
Figure 2.3: Radar site geometry for the HOME experiment. The two radar sites are indicated in blue. Both sites sampled $120°$ arcs, with $\sim 60°$ of overlap. Range arcs are shown at 50 and 100 km. The polar data was interpolated to a cartesian grid with 2 km resolution [dots]. The mean swell direction for this study was $150°$ degrees [arrow].
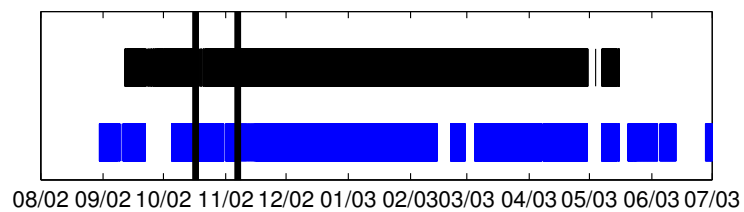
Figure 2.4: Temporal coverage of available data for Koolina [top] and Kaena [bottom]. Study period was 21 days from 10/21/2002 to 11/02/2002, corresponding to $N = 1221$ paired time samples.
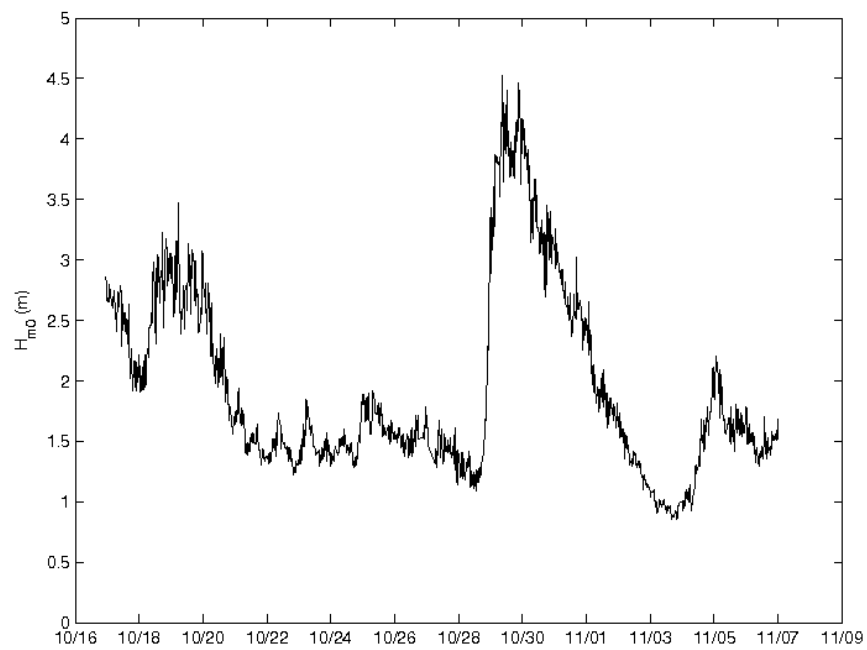
Figure 2.5: CDIP buoy significant wave height $H_{m0} = 4\sqrt{m_0}$ where m_0 is the zeroth moment of the energy spectrum. The study period spanned 21 days and two major swell events.

2.2 Processing

The raw data created by a HF radar is not simply or directly related to the physical processes measured. Algorithms are used to process the raw data into ocean state parameters. The primary tasks of an oceanographic radar algorithm are the identification and delineation of Doppler features, combined with some degree of quality control. The spectral peaks are not fixed in frequency location, necessitating search and delineation functions. Filtering and averaging in both space and time are usually employed. Data-adaptive or fixed parameter methods may be used. Quality control logic for the inclusion or rejection of data can be based on different criteria. These tasks are held in contrast to the well defined and unambiguous equations relating Doppler features to ocean parameters. The algorithmic technique by which the tasks are accomplished, and with varying skill, is arbitrary and thus a potential source of error.

The WERA radar is paired with a scientific analysis package, hereafter referred to as the WERA algorithm. As explained in §3, initial evaluation of WERA H_s error motivated stepwise inspection of the processing algorithm. Since the intermediate WERA variables were not available, a similar algorithm was developed for this work, hereafter the GS algorithm. Differences between the algorithms will be discussed with regard to effects on the final data products. When the algorithms are not mentioned, it is implied they are either identical in method or not significantly different in analysis. A summary of the WERA algorithm is given in §B.

A key component of any algorithm is the delineation of first order (S1), second order (S2), and noise energy in the spectrum (Figure 2.6). The S1 region is identified by peak values in the spectrum, and extends to the null (minimum) between S1 and S2. The algorithm identifies the null by maximizing the peak/null ratio. This avoids an error-prone difference search (Figure 2.7). The S1:S2 null is explained theoretically in [Barrick and Weber, 1977]. In short, the second order waves exist *outside* the wavevector-frequency space of first order waves. Terminology used in this thesis are; negative and positive, to refer to the negative and positive Doppler frequencies, i.e. surface features moving away and towards the radar. S2 inner and outer, to refer to the second order sidebands located at lesser and greater absolute frequencies relative to their respective Bragg peak. The signal-to-noise ratio (SNR) is often used to compare the relative amplitudes of the ocean signal S to the noise N in the Doppler spectrum:

$$\text{SNR}_{dB} = 10 \log_{10}(\frac{S^2}{N^2}) = 20 \log_{10}(\frac{S}{N}) \qquad (2.2.1)$$

35
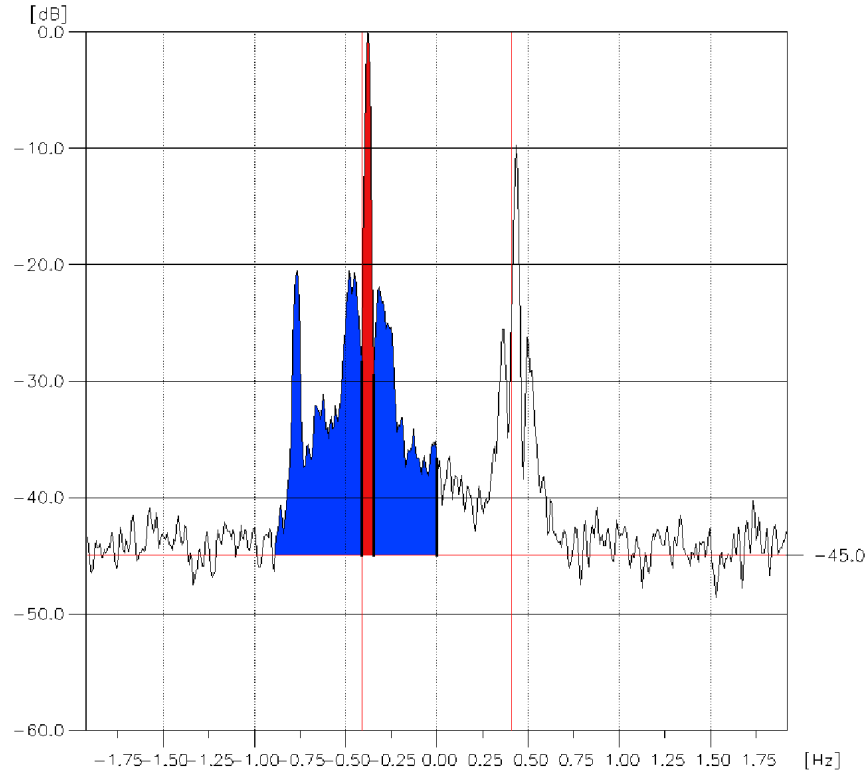
Figure 2.6: An example Doppler spectra from Kaena. First order (S1) region is in red. Second order (S2) region in blue. The frequency location of the S1:S2 null delineates the two regions. Noise level is ~ -45 dB

where S is the amplitude of a signal sinusoid. A decibel scale is used because of the large dynamic range.

Proceeding the delineation of the first and second order regions, the centroid frequency of the Bragg peak can be calculated. Accurate estimation of the Bragg peak frequency is necessary for calculation of surface currents, and it is also required for second order measurements. The Doppler shift due to surface currents must be removed from the spectra before further averaging or inter-comparison. The simplest estimate is the frequency of the peak spectral value. A more physically sensible alternative is the centroid frequency, as it is the mean location of signal energy [Barrick, 1980]. The definition of centroid frequency is:

$$\tilde{f} = \frac{\Delta f \sum i P_i}{\sum P_i} \qquad (2.2.2)$$
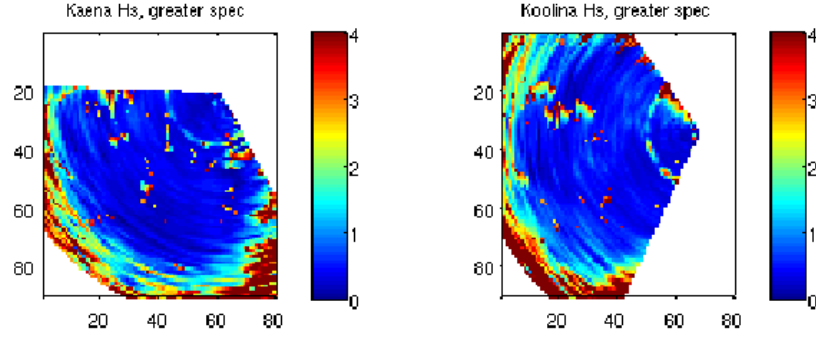
Figure 2.7: H$_s$ errors due to a difference search in the S1:S2 null detection. Difference searches tend to amplify noise. In this example, S1 energy is being underestimated due to slope inversions in the Bragg peak, i.e. "split peaks".

where Δf is the spectral frequency resolution, $i\Delta f$ is the frequency position of the ith point, and P_i is the spectral power at point i. Barrick [1980] derived a general expression for the error in centroid frequency as the standard deviation of $\tilde{f} - f_t$ where f_t is the true position of the peak:

$$\sigma(\frac{\tilde{f} - f_t}{\Delta f}) = \frac{\sqrt{\frac{1}{K} \sum_i i^2 P_i^2}}{\sum_i P_i} \qquad (2.2.3)$$

For the centroid equation 2.2.2, Barrick shows that it makes no difference in accuracy how the original fixed length time series is divided into consecutive spectra and incoherently averaged. To decrease the centroid frequency standard deviation by a factor of two, the time series length must be increased by a factor of four.

Both the WERA and GS algorithm use the centroid method for estimating the Bragg peak frequency location. The GS algorithm had consistent results for SNR > 10 dB (Figure 2.8). Centroid frequencies result in greater radial current resolution, as they use $1/N\Delta f$ compared to $1/\Delta f$ for a simple Bragg peak maximum (Figure 2.9). The accuracy of the two frequency location estimates cannot be evaluated without a reference measurement. The frequency difference between the two methods is Gaussian distributed with zero mean, and tails off (3σ) at $\sim 1\Delta f$ (Figure 2.10), suggesting the centroid calculation is not a significant source for processing error.
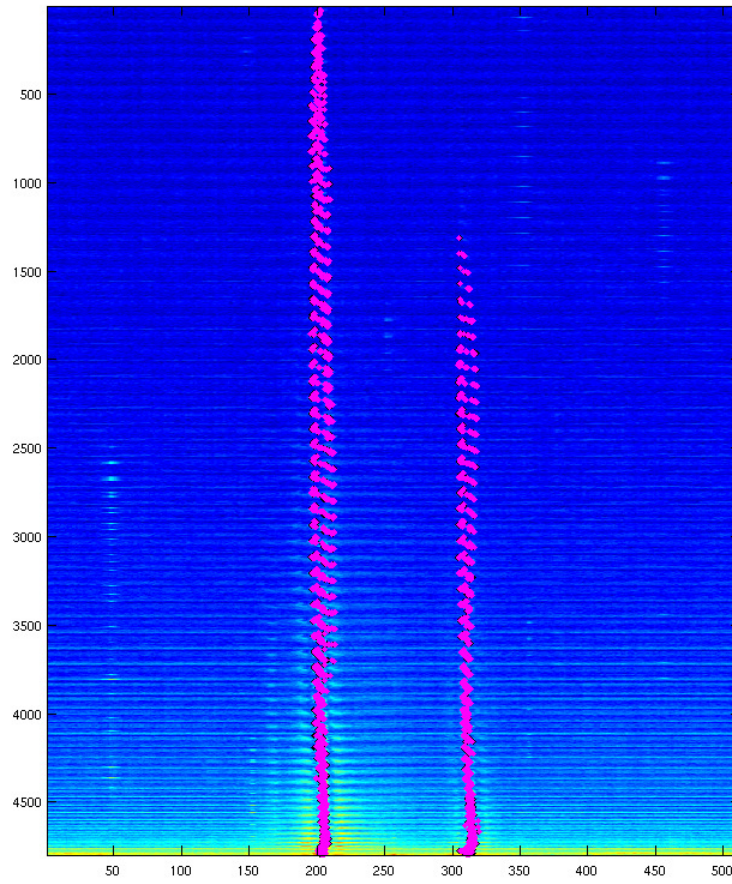
Figure 2.8: Results from the Bragg centroid frequency algorithm for a single time frame. The underlying image is a spectrogram of power spectral density with frequency on the horizontal axis and range on the vertical. Frequency locations of the Bragg peaks are marked for each range cell [magenta].
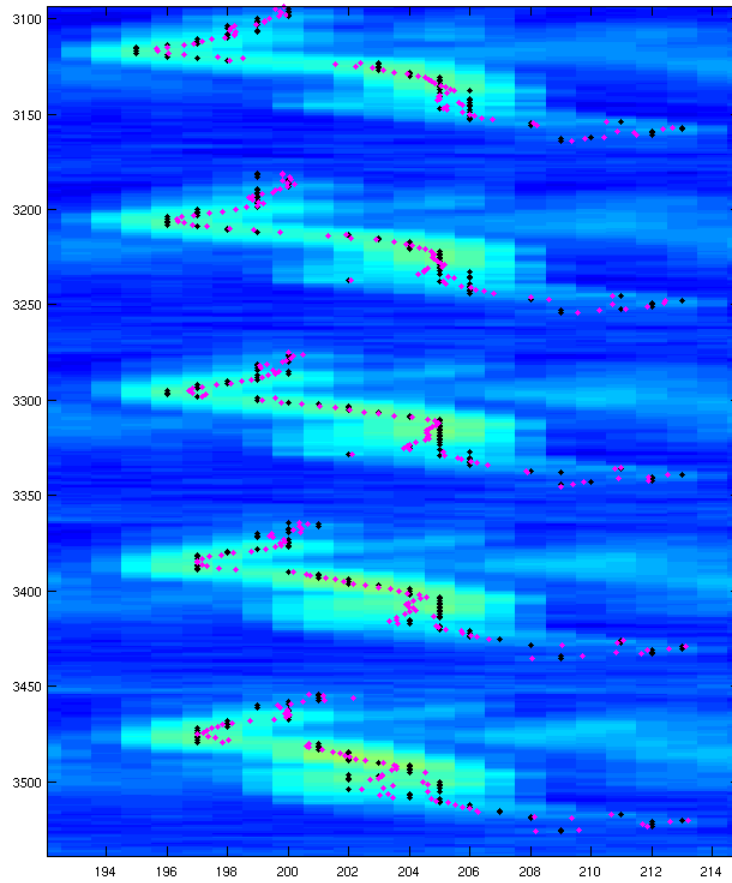
Figure 2.9: Close up of Figure 2.8, showing the results of the centroid [magenta] vs. peak [black] frequency methods calculation. The centroid frequency exceeds the $1/\Delta f$ resolution limitation of the peak frequency.
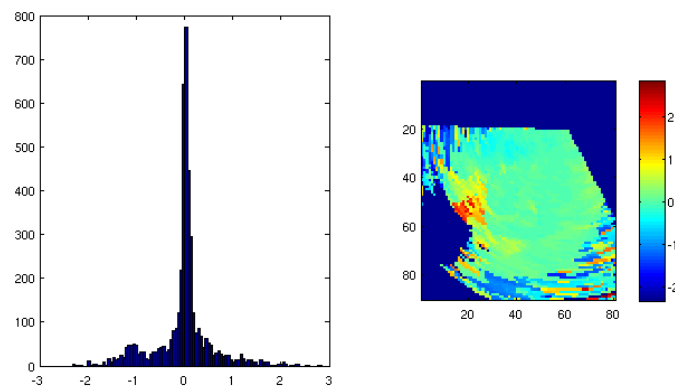
Figure 2.10: The distribution of frequency difference for Bragg frequency methods is Gaussian-like with ($\pm 3\sigma$) at $\sim 1\Delta f$. Units on both plots are Δf. The spatial field of the difference is plotted on the right.

Chapter 3

Results

3.1 Winds

QuickSCAT and Multi-Spectral Model (MSM) wind model output was obtained for comparison to the radar wind fields(Figure 3.1). A composite field of MSM and RSM data was re-sampled to match the WERA processing grid, hereafter RMSM. QuickSCAT spatial resolution was much coarser (Figure 3.2), with ¡ 10 spatial samples available for a given time.

Inspection of the wind estimates from the Oahu radars showed good spatial and temporal coherence (Figure 3.3), with significantly more spatial variance than the RMSM data (Figure 3.4). The $O(1000)$ data points from the RMSM field could essentially be reduced to a single wind vector with little loss of information. Maximum vector correlation between the RMSM and radar fields was $r^2 = 0.23$.

The radar winds were binned into an angular histogram as a function of time and compared to the mean QuickSCAT wind direction (Figure 3.5). Strong agreement between the radar wind fields and QuickSCAT samples was found. Complex correlation between the mean radar and QuickSCAT wind timeseries was $r^2 = 0.83$, with zero angular bias. The radar wind histogram revealed bimodal wind fields not observed in the reference data sets.
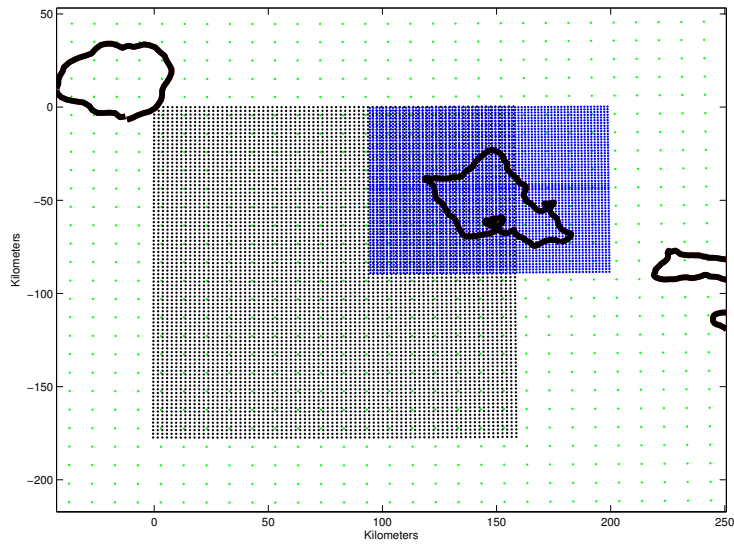
Figure 3.1: Multi-Spectral Model grid. Higher-resolution (1.45 km) MSM output [blue] was combined with lower-resolution (10 km) RSM output [green] and resampled to match the WERA processing grid (2 km) [black].
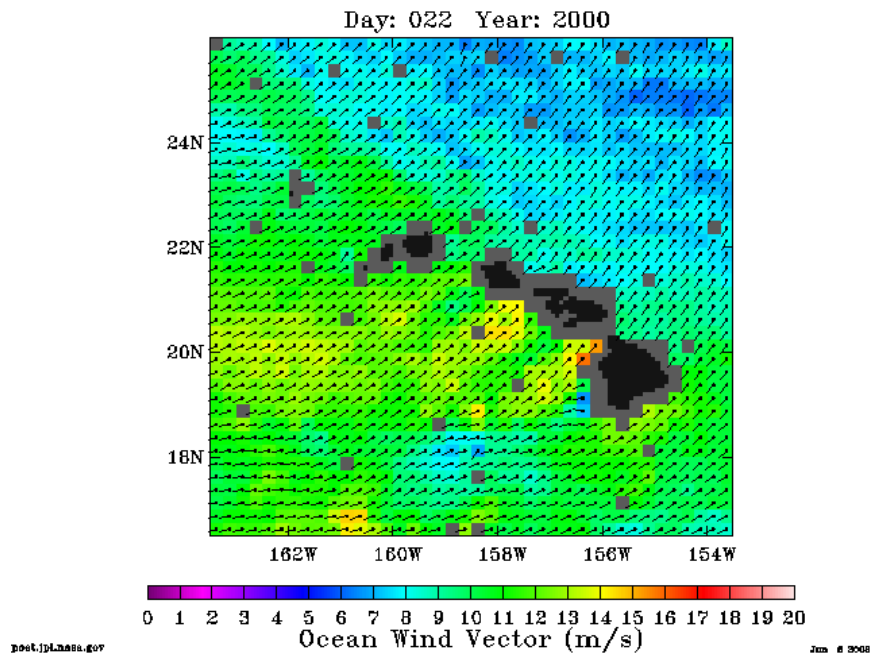
Figure 3.2: QuickSCAT winds for the Hawaiian Islands. The spatial resolution of QuickSCAT yielded ¡ 10 spatial samples of overlap with the radar field.
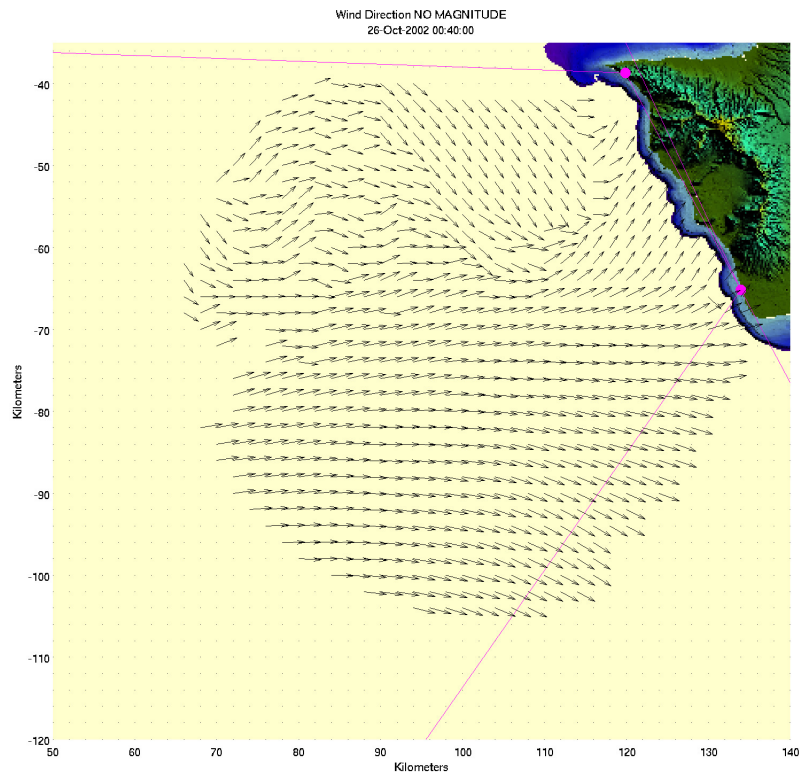
Figure 3.3: An example radar-derived wind field. Arrows represent wind direction only, no magnitude is inferred.
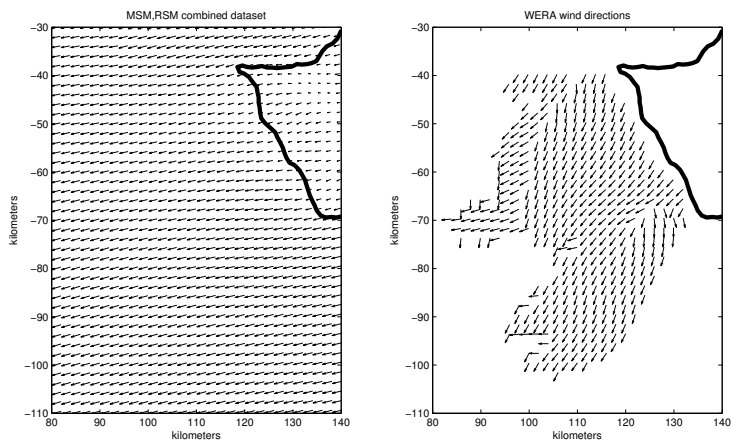
Figure 3.4: Radar wind field compared to MSM output
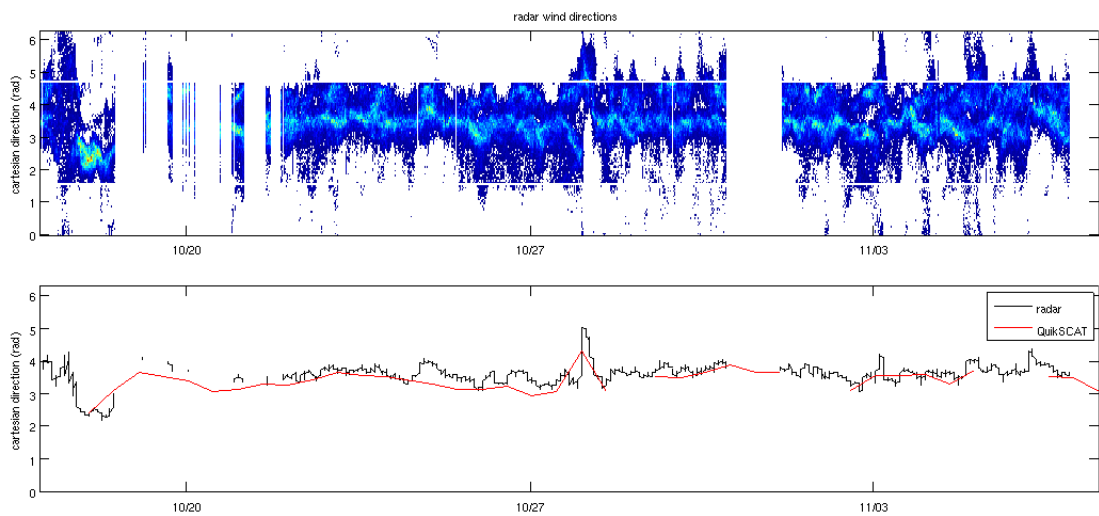
Figure 3.5: A comparison of the radar wind field to QuickSCAT data. An angular histogram of the radar winds [top] shows predominantly westward winds coherent in time, with frequent bimodal intervals. The timeseries of mean wind direction [bottom] are in good agreement with zero bias.

44
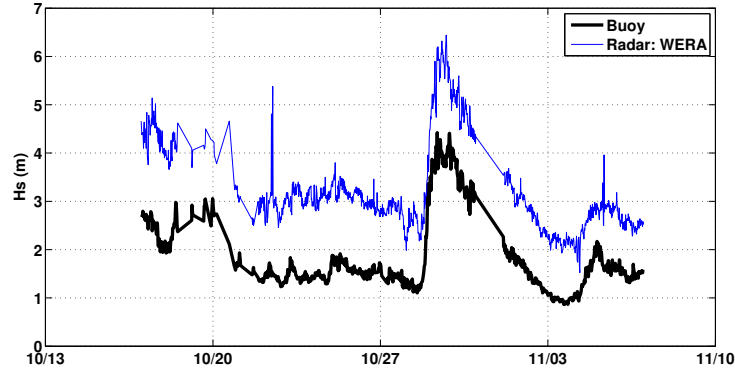
Figure 3.6: H_s timeseries for CDIP buoy (black) and radar (blue). The period is 21 days. The radar estimate is a median for the entire measurement region, and has a consistent $+1.25$ m offset.

3.2 Significant Waveheight

Initial inspection of the WERA algorithm output showed good performance at estimating *spatially-averaged* H_s. The spatial median of the WERA H_s field was in agreement with the CDIP buoy timeseries over the 21 day period, although the radar exhibited a consistent $+1.25$ m offset (Figure 3.6). Large spatially and temporally variant features were observed in the WERA H_s field (Figure 3.7). Gradients of $O(3)$ m were observed within 5 km and 40 minutes of separation. Accuracy for the full spatial-temporal fields was poor; an RMS error of 2.58 m and a RSE of 142%. These H_s variations greatly exceeded the range commonly reported in theoretical and observational studies; 15% theoretical spatial variation [Barrick, 1977], and $O(10$ cm) RMS difference to buoy measurements [Maresca and Georges, 1980, Heron et al., 1985, Wyatt and Green, 2002, Gurgel et al., 2006].

Linear regressions of all space and time samples (Figure 3.8) and the spatially-averaged timeseries (Figure 3.9) were consistent with the WERA 1.25 m offset. Agreement with scattering theory was confirmed by linearizing the power law 1.5.7 as $\log k_0 H_s = \log C + p \log q$ and regressing. Both the complete space-time dataset (Figure 3.10) and the spatially-averaged timeseries (Figure 3.11) gave correct values for the coefficient $C = \sqrt{2}$ and power $p = 1/2$. The combined results of this regression analysis suggest the WERA algorithm uses theoretically correct scaling. The same regression analysis was performed on the GS H_s estimates, which gave similar agreement with theory but lower coefficients of determination.

45
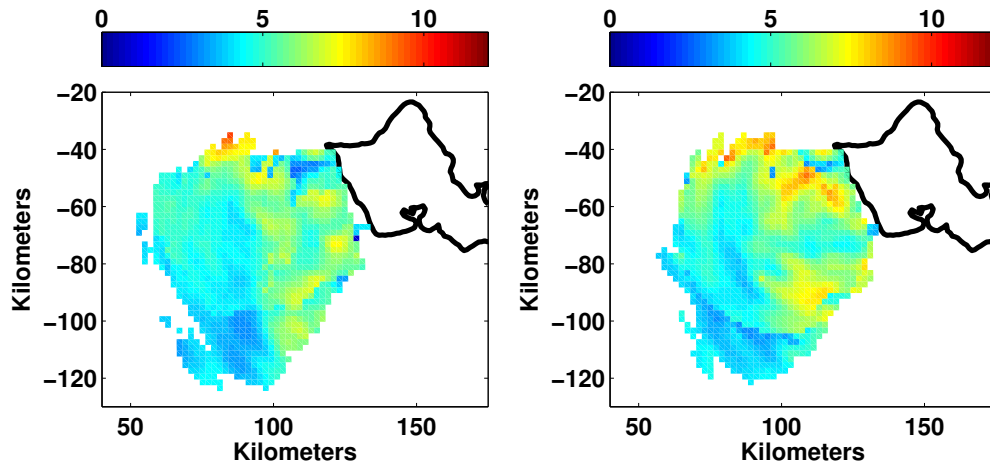
Figure 3.7: Large variations in the radar H_s field were observed, both spatially and temporally. H_s is indicated in color. Independent estimates are available from each radar site. Gradients of $O(3)$ m were observed within 5 km and 40 min. of separation.
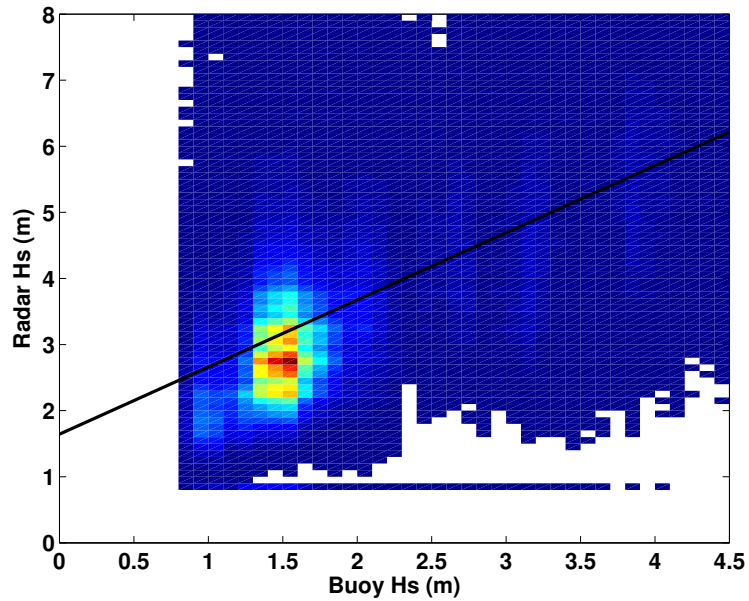
Figure 3.8: A linear regression of the radar H_s to the reference buoy gave $y = 1.02x + 1.64$, and a coefficient of determination $r^2 = 0.17$
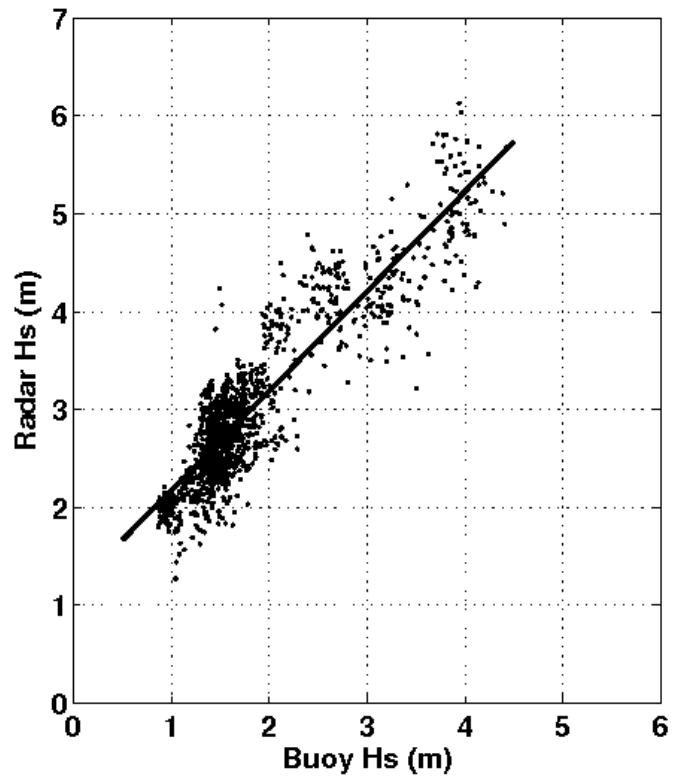
Figure 3.9: A linear regression of the spatially-averaged radar H_s timeseries to the reference buoy gave $y = 1.02x + 1.16$, and a coefficient of determination $r^2 = 0.82$.
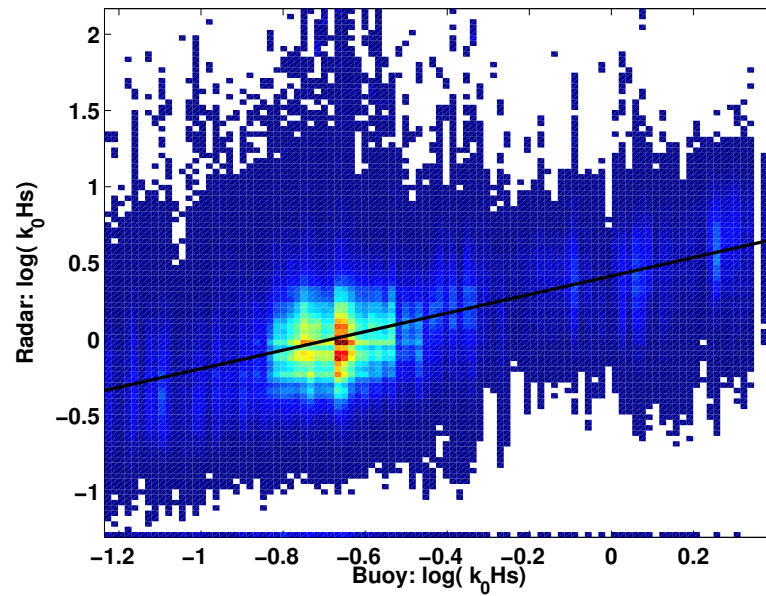
Figure 3.10: The H_s power law $k_0 H_s = \sqrt{2}q^{1/2} = Cq^p$ can be linearized as $\log k_0 H_s = \log C + p \log q$. The underlying image is a histogram of radar observations as a function of the buoy reference value. Regression of the linearized equation gave $C = 1.51$ and $p = 0.61$, and a coefficient of determination $r^2 = 0.28$
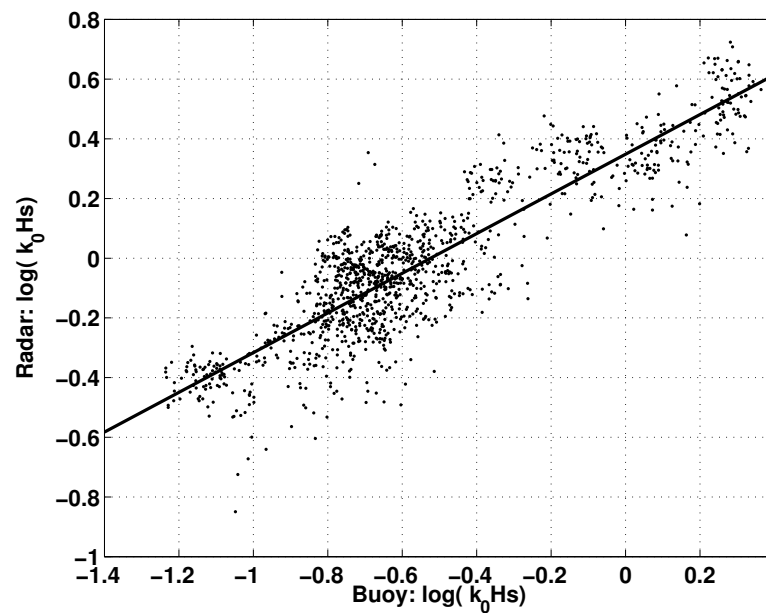
Figure 3.11: The same linearized power law regression was calculated for the spatially-averaged timeseries, yielding $C = 1.42$ and $p = 0.67$, and a coefficient of determination $r^2 = 0.79$

Table 3.1: H_s error analysis

		all data	median	$\langle q^p \rangle$	$\langle q^{-1} \rangle^{-p}$	$\langle q^{-p} \rangle^{-1}$
	RMS	2.58	1.46	1.74	1.25	1.38
WERA	RSE	142%	80%	96%	68%	76%
	bias	2.16	1.87	2.01	1.73	1.82
	RMS	9.83	2.59	4.94	0.68	1.10
GS	RSE	540%	142%	271%	38%	60%
	bias	3.53	1.96	3.16	1.01	1.51

spatial averages

Improved H_s accuracy was achieved following the averaging recommendations of Barrick [1980], as summarized in §1.5.3. Spatially-averaged timeseries were calculated using the median, arithmetic mean $\langle q^p \rangle$, inverse quotient $\langle q^{-1} \rangle^{-p}$, and inverse quotient to the pth $\langle q^{-p} \rangle^{-1}$. Three error metrics; the rms error, relative standard error, and error bias were calculated for these averaging methods (Table 3.1). All averaging methods gave improved accuracy compared to the full space-time data set. The inverse quotient resulted in the highest accuracy for all error metrics. Barrick [1980] found the inverse quotient to the pth to be the most accurate, with the inverse quotient a close second. The WERA estimates were moderately improved by spatial averaging, whereas the GS estimates drastically improved and exceeded the WERA algorithm in accuracy. The most accurate results were for the GS algorithm using inverse quotient averaging, yielding a rms error of 0.68 m, RSE error of 38%, and a bias of 1.01.

The improvement in H_s accuracy from spatial averaging is better understood in terms of the probability distribution. Histograms estimates of the probability distribution were calculated for the reference buoy and both H_s algorithms. For the full data set, both algorithms had distributions biased +1-2 m higher than the reference buoy. The inverse quotient mean used in the spatial averaging is heavily weighted towards the lower H_s values, as exhibited by the GS estimates approaching the reference buoy distribution (Figure 3.12). The WERA distribution lacks lower H_s values and is less affected from averaging. Thus the large improvement in GS accuracy is due to the inverse quotient mean shifting the values towards the correct distribution. The WERA estimates benefit less from averaging because the distribution lacks the lower H_s values. The cutoff in the WERA distribution below H_s 1 ms^{-1} is due to a forced minimum in the algorithm. Thus the probability of the lowest H_s bin is biased. Furthermore, the WERA algorithm applies an empirical weighting to the spectral energies used in the H_s equation 1.5.5, which may ultimately explain the difference in accuracy and distribution compared to the un-weighted GS algorithm (see §B).

49
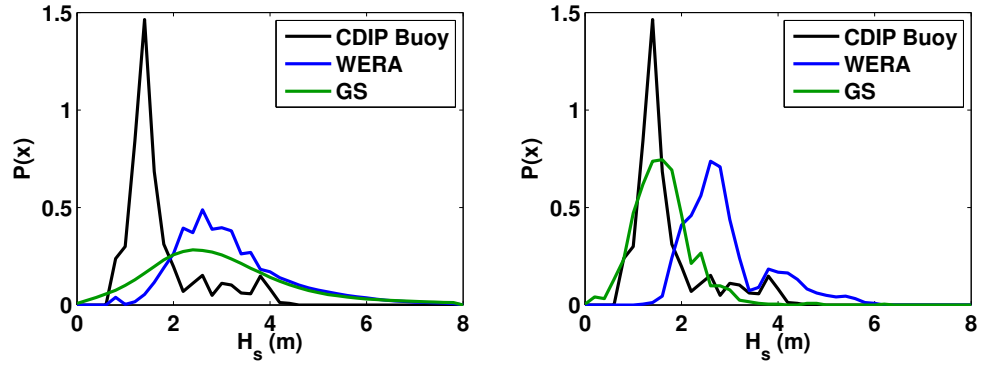
Figure 3.12: Probability distributions were calculated from histograms of the H_s estimates. The reference buoy distribution [black] is compared to the WERA [blue] and GS [green] algorithm estimates. Both the full space-time data set [left], and the spatially-averaged [right] distributions are shown. The effect of the inverse quotient averaging is seen as a weighting of the distributions towards lower values. Such averaging greatly improves the GS estimate accuracy. The WERA distribution lacks the necessary lower H_s values.

Barrick [1980] found the theoretical RSE scaled as $\sqrt{K}$ where K is the number of values used in the average. For this study, K is typically between 500 to 1000 samples, giving an expected sampling RSE of 2.2-1.5%. The most accurate observed RSE was 38%, suggesting additional error sources. Inspection of the H_s spatial fields revealed a strong directional dependence of the magnitude (Figure 3.13). Both algorithms showed good agreement, suggesting the variations were due to a shared algorithm method or inherent to the data.

It was hypothesized that the H_s spatial variation was due to a simple angular relationship between the incident radar wavevector and ocean spectrum mean direction, analogous to the vector relationship for current measurements (Figure 1.2). If so, it would be evident in the spatial cross correlation between radar sites Chavanne et al. [2007]. Since $H_s > 0$, the covariance would follow $|\cos\theta|$, where θ is the angle between sites. No spatial pattern was observed in the spatial cross correlation between the sites (Figure 3.14). With the added assumption of a spatially homogeneous wave field, each site would exhibit similar dependence for the same absolute beam angles. This relationship was not observed. Time averaging the H_s field from 1 to 21 day increments did not remove the spatial variation, indicating some degree of temporal coherence (Figures 3.15,3.16). Further analysis of the directional dependence of the H_s measurement is given in §3.5.
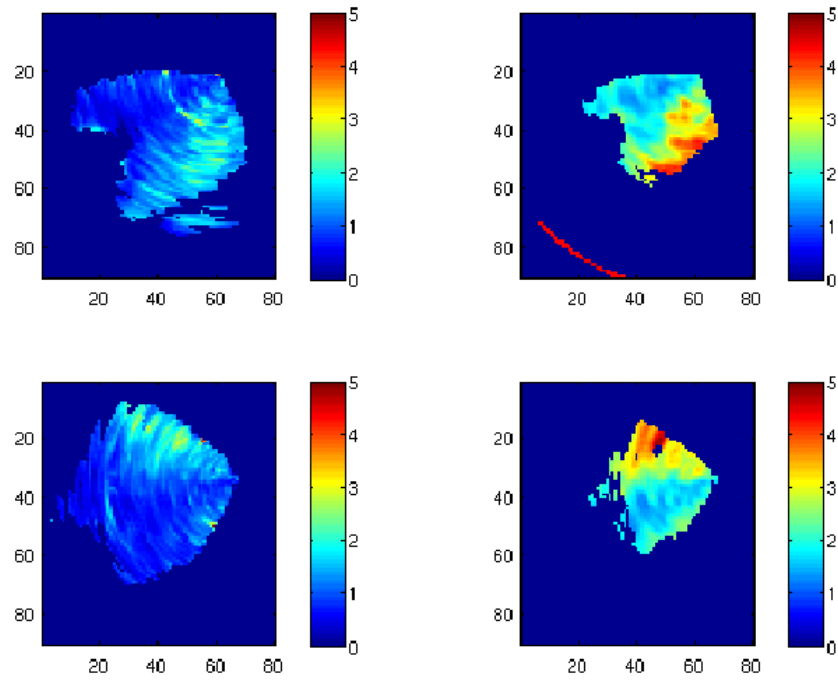
Figure 3.13: H_s results from the WERA [right] and GS algorithms [left] for a single time sample. Kaena site [top] and Koolina site [bottom]. Spatial H_s features are smoother in the WERA output due to 4x4 grid cell spectral averaging. The directional dependence is consistent between sites for the same absolute beam angle. It is shown in §3.3 that this dependence is due to external interference.
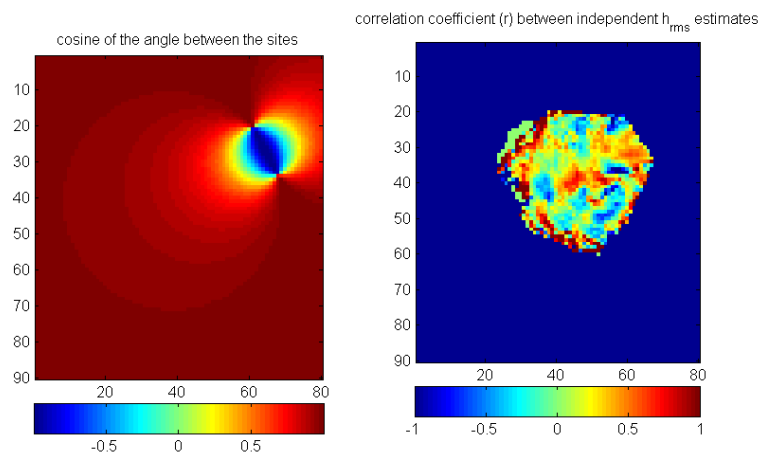
Figure 3.14: Theoretical and observed H_s spatial correlation. Assuming a direction dependence to the H_s measurement, the spatial field of cross correlation between the sites would follow a $|\cos\theta|$ relationship [left], where θ is the angle between sites. No such relationship was observed [right].
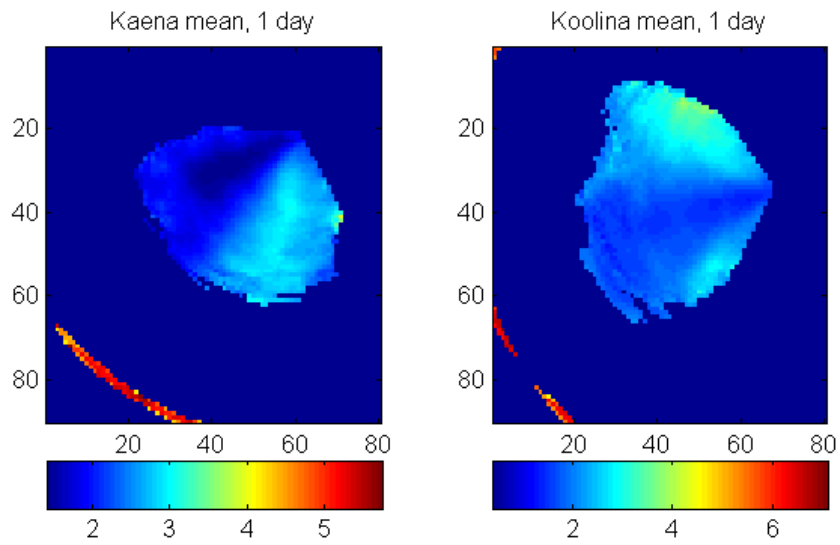
Figure 3.15: The spatial H_s variation is coherent over a 1 day mean.
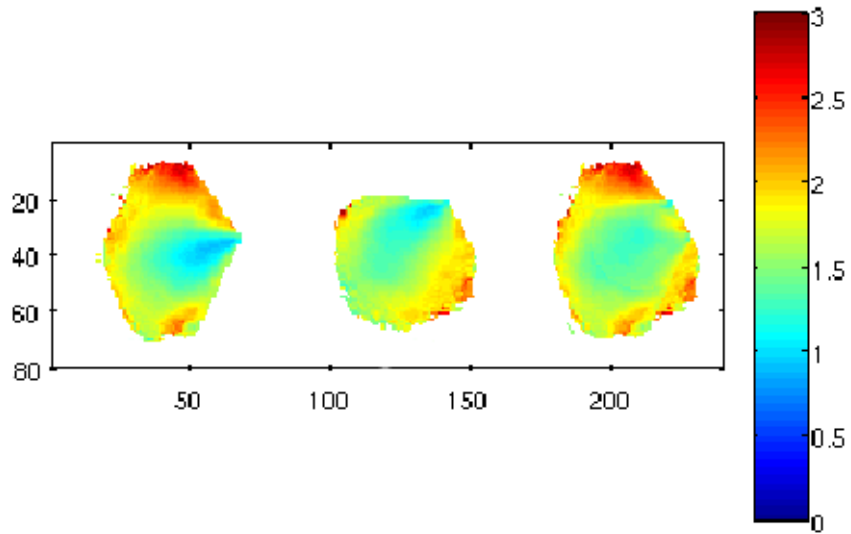
Figure 3.16: The 21 day median of the H_s field shows the spatial variation is coherent in time. The combined field [right] can be closely approximated with a site-average (Koolina [left] and Kaena [center]), although the WERA algorithm uses a more complicated method §B.

3.3 Noise Error

3.3.1 Introduction

It was hypothesized that the observed H_s variation could be attributed to noise sources in the radar measurement. There are two major categories of noise error in radar sampling. Defined by their effect, they are additive and multiplicative. Multiplicative noise is a consequence of radar operation, wherein gain factors are introduced, e.g. due to signal attenuation with range and variable channel strengths. Multiplicative noise is relatively easy to compensate for in processing, and is not discussed herein. Additive noise results from multiple real signals, e.g. the desired ocean scatter, external interference, ship echoes, and internal systematic noise. Internal system noise can be caused by aliased harmonics from the power supply and surrounding electronics, mechanical vibration, and from thermal noise in the conductors. Generated by the thermal excitation of electrons inside a conductor, thermal noise is approximately white with a very nearly Gaussian distribution [Nyquist, 1928]. The background, or minimal, variation of the Doppler spectra is electromagnetic and thermal [Gurgel et al., 2006].

External interference behaves additively [Ponsford et al., 2003] and is range-independent [Gurgel et al., 2006]. In the HF frequency band, the primary source of interference is anthropogenic transmissions, and thus commonly referred to as radio frequency interference (RFI). The dominating source of interference in the HF band is RFI [Molnar et al., 1990]. Due to the ionospheric propagation and reflection of HF EM waves, unoccupied frequencies of sufficient bandwidth (50-100 kHz) can be extremely difficult to find. Ionospheric conditions change with solar insolation, are more suited for reflecting interference sources at night [Ponsford et al., 2003], and can propagate signals over 1000's of kilometers.

Canceling additive noise is most difficult when its frequency matches the desired signal. From the Harmonic Addition Theorem, any linear combination of sine waves with equal frequency results in a sine wave with the same frequency, but modified amplitude and phase. Given two sinusoidal functions with the same frequency ω:

$$\psi_1 = A_1 \sin(\omega t + \delta_1) \tag{3.3.1}$$

$$\psi_2 = A_2 \sin(\omega t + \delta_2) \tag{3.3.2}$$

their sum ψ can be expressed as a sinusoidal function with frequency ω:

$$\psi \equiv \psi_1 + \psi_2 \equiv A \sin(\omega t + \delta) \tag{3.3.3}$$

where A and δ are defined as:

$$A^2 = A_1^2 + A_2^2 + 2A_1A_2\cos(\delta_1 - \delta_2) \tag{3.3.4}$$

$$\tan(\delta) = \frac{A_1\sin\delta_1 + A_2\sin\delta_2}{A_1\cos\delta_1 + A_2\cos\delta_2} \tag{3.3.5}$$

From Equation 3.3.4, the amplitude of the total sinusoid ψ does not behave additively. It depends on the phase difference $\delta_1 - \delta_2$. This non-additive behavior for the total amplitude A is the reason why simple techniques, e.g. averaging or subtraction, do not work to remove additive noise error. Noise at signal frequencies modifies the amplitudes unpredictably as a function of their phase relationship. The actual signal sinusoid ψ_1 can be recovered with knowledge of the total ψ and noise ψ_2 sinusoids.

3.3.2 Observations

Inspection of the raw antenna spectra (Figure 3.17) and beamformed noise levels (Figure 3.21) identified the characteristic noise sources. Thermal background noise was observed in samples with the highest SNR; up to 100 dB below the first order Bragg peaks (Figure 3.17). Samples with low SNR were contaminated with ringing, full-spectrum noise exhibiting range-independence. Broad spectral peaks at various ranges were due to 60 Hz harmonics of the power supply, and possibly other unknown sources (Figure 3.17). Observations by Gurgel et al. [2006] have shown similar noise characteristics (Figures 3.18). Beamforming (§C) and noise level estimation (§3.3.3) were used to investigate the spatial characteristics of noise sources (Figure 3.21). The deformation of Doppler spectra by RFI varied across the sampling field. In the direction of a RFI source, Bragg peaks were deformed, preventing detection of the S1:S2 null (Figure 3.20), and introduced amplitude noise in the S2 region. Outside of RFI source directions, samples at the same time and range were usable (Figure 3.19).

Additive noise of sufficient energy prevent accurate estimation of second order energy. Ideal spectra have sufficiently high SNR that both the first and second order signal are well above the noise floor (Figure 3.19). Unusable spectra have very low SNR due to the full-spectrum range-independent noise (Figure 3.20). In terms of accuracy and data quality control, such spectra are not a problem as they can be unambiguously rejected. Rather, samples with intermediate SNR pose the greatest difficulty. For intermediate SNR, Bragg peaks are easily identified, albeit with frequency errors due to noise energy in the centroid amplitude weighting. In contrast, the second order sidebands are completely contaminated. Noise energy introduces an amplitude ambiguity
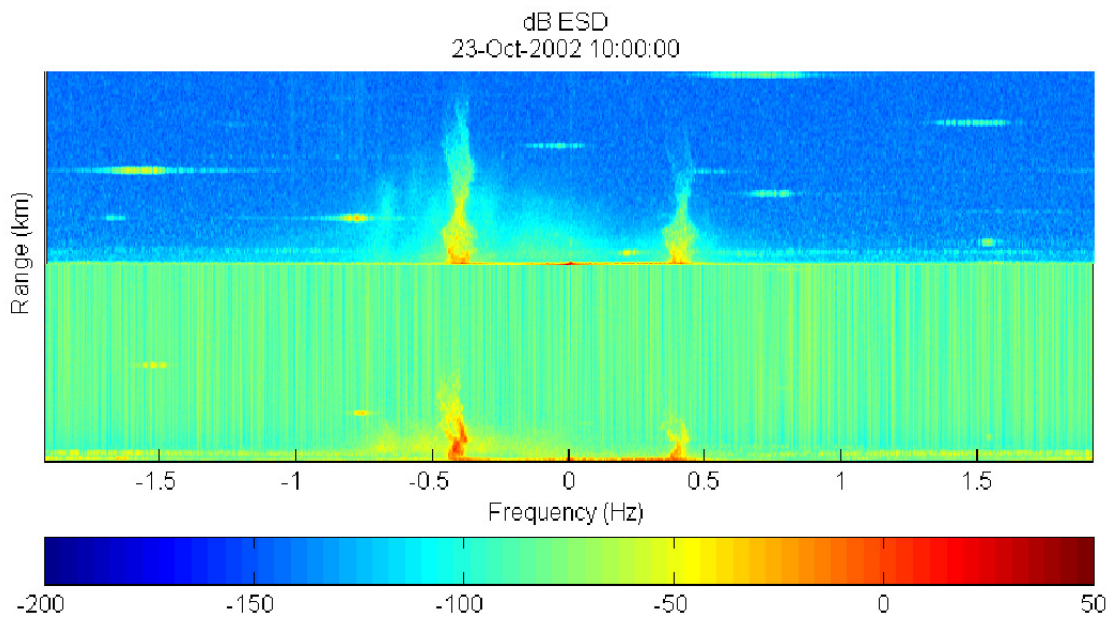
Figure 3.17: Two example spectra illustrating periods of low [top] and high [bottom] noise are given for a single channel. The thermal background is observed in the low noise example at 100 dB below the Bragg peaks. Broad spectral peaks at various ranges are due to 60 Hz harmonics and other systematic noise. The primary noise source is external interference, which is characterized by range-independence [bottom].
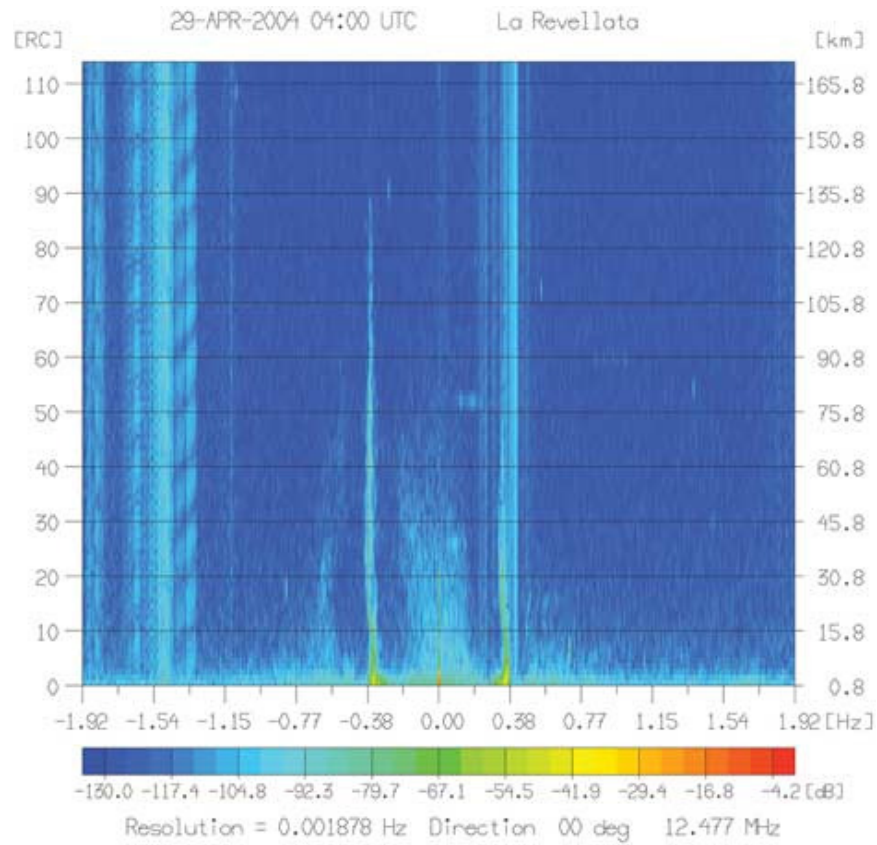
Figure 3.18: from Gurgel et al. [2006]. Backscatter spectrum versus range at 0^0 beam steering as measured by the WERA installed at La Revellata. This figure shows strong radio interference, which often arises in form of vertical lines, i.e. the interference is range independent. In the case show, the right first-order Bragg lines and the surrounding second-order sidebands are disrupted by interference.
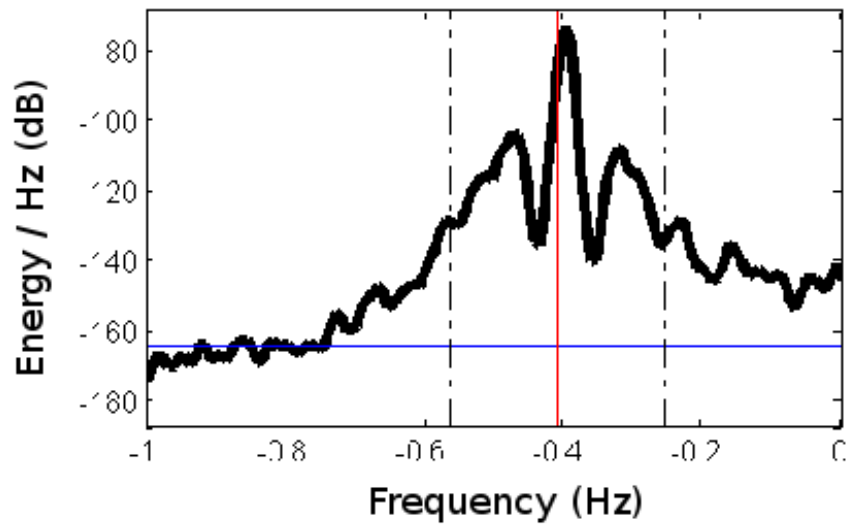
Figure 3.19: An ideal Doppler spectrum [black] showing a clearly defined first order peak and second order sidebands. The S1 width is defined, and detected by the processing algorithm, by the nulls on each side. Most of the S2 energy is above the noise level [blue].

which cannot be recovered. The result is erroneous H_s estimates due to the inclusion of noise in the energy integral.
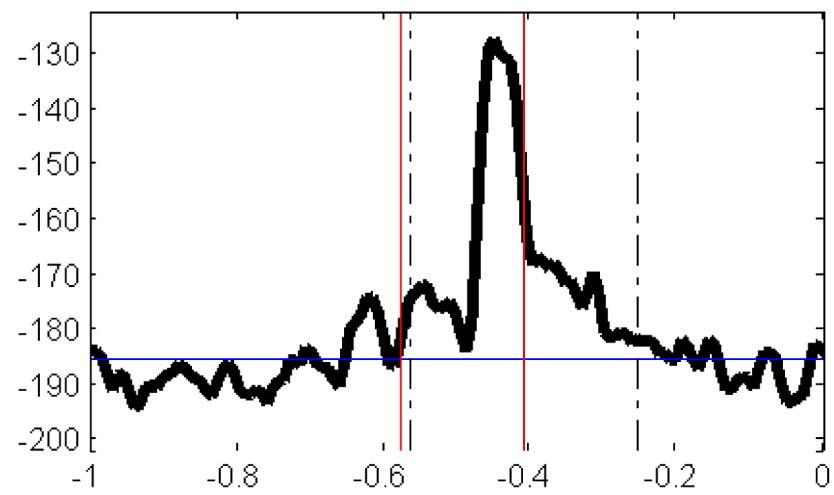
Figure 3.20: A contaminated Doppler spectrum [black], with deformed first order peak. A lack of clear nulls separating the S1 and S2 regions prevents accurate estimation of either energy. The S2 region is beneath the noise level [blue].
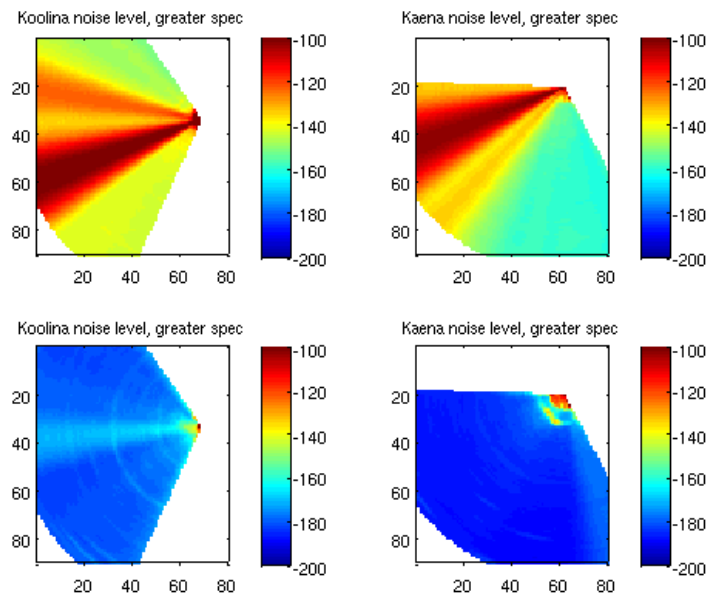
Figure 3.21: Two example noise fields illustrating period of low [bottom] and high [top] noise. Estimated noise levels are given in color. The primary noise source is external interference, which is characterized by range-independent beams from specific directions.

3.3.3 Noise Estimation

For estimating the noise level, Heron and Heron [2001] proposed fitting the entire Doppler spectrum to a statistical distribution for noise. By iteratively discarding signal, i.e. spectral points with large values, the distribution converged to a model for the noise. This method assumes the noise is white, and thus the power spectrum of noise is Rayleigh distributed.

The Rayleigh distribution has one parameter, p. The Rayleigh probability density and cumulative distribution functions are:

$$f(x; p) = \frac{x}{p^2} e^{\frac{-x^2}{2p^2}} \tag{3.3.6}$$

$$F(x; p) = 1 - e^{\frac{-x^2}{2p^2}} \tag{3.3.7}$$

$$\text{for } x \in [0, \infty) \tag{3.3.8}$$

The mean and variance of a Rayleigh random variable are:

$$\mu(X) = p\sqrt{\frac{\pi}{2}} \tag{3.3.9}$$

$$\sigma = p^2 \frac{4 - \pi}{2} \tag{3.3.10}$$

Given N independent and identically distributed Rayleigh random variables with parameter p, the maximum likelihood estimate (MLE) of p is:

$$\hat{p} = \sqrt{\frac{1}{2N} \sum_{i=1}^{N} x_i^2} \tag{3.3.11}$$

Four methods were evaluated for estimating the mean noise level. The first three were direct calculations of the spectral power mean, median, and maximum likelihood estimate (MLE). The fourth method followed Heron and Heron [2001]; a linear least squares regression of the ordered spectral data to a Rayleigh cumulative distribution function (CDF) (Figure 3.22). All methods used the same iterative scheme which discarded outliers based on the variance.

The MLE estimate did not converge to the noise distribution due to the x^2 weighting in its equation, which acts to bias it towards greater-valued signal. As a first approximation, the MLE is a poor fit to the sum of a Rayleigh and signal (unknown) distribution. Likewise, the median estimate performed better than the mean, as it was not weighted towards extreme signal values. Iterations
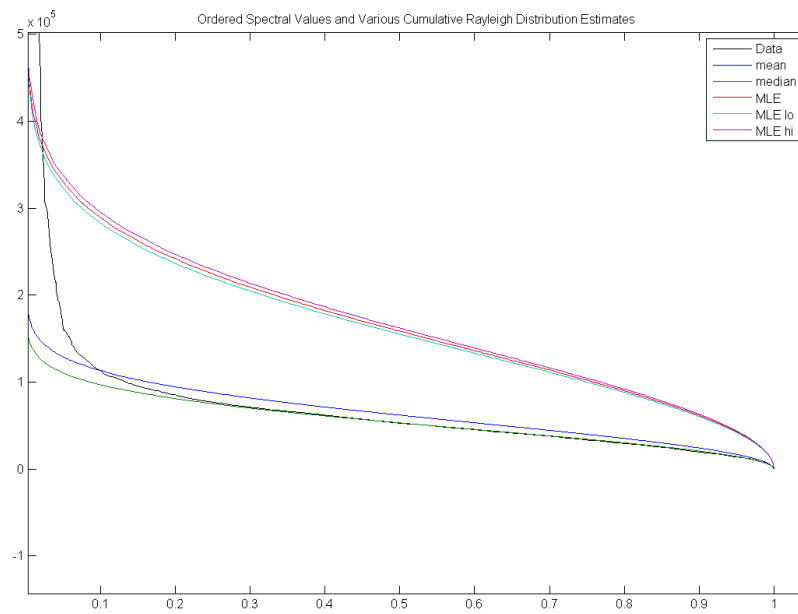
Figure 3.22: Ordered spectral values [black] compared to various direct methods for estimating the noise CDF. X-axis is CDF probability. Y-axis is spectral powers. Low-power noise $P < 1 \cdot 10^5$ comprises 90% of the CDF. The mean [blue] and median [green] closely approximate the noise distribution. The MLE [red] is biased towards larger signal values due to the x^2 weighting in its calculation.
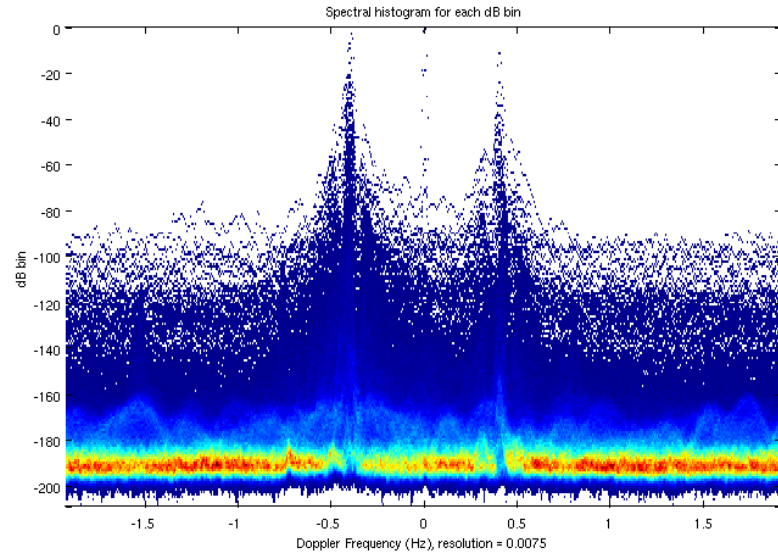
Figure 3.23: Spectral histogram of noise levels for one time sample. The background noise floor is -190 dB. Full-spectrum, ringing noise is seen from   -160 to -180 dB

converged quickly, to 95% and 99% of the final value within 3 and 5 iterations, respectively. Because only the greater outliers are discarded, iterations always act to decrease the noise estimate.

A spectral histogram indicated a noise floor of ~ -190 dB, probably limited by either thermal or numerical noise. Coherent, ringing noise was observed from ~ -160 to -180 dB (Figure 3.23). Distribution of noise estimates yielded a minimum noise level of -190 dB (Figure 3.24). The Koolina distribution was shifted towards greater noise levels because its angular coverage was directed more towards the north, and thus included more interference sourced from Asia.
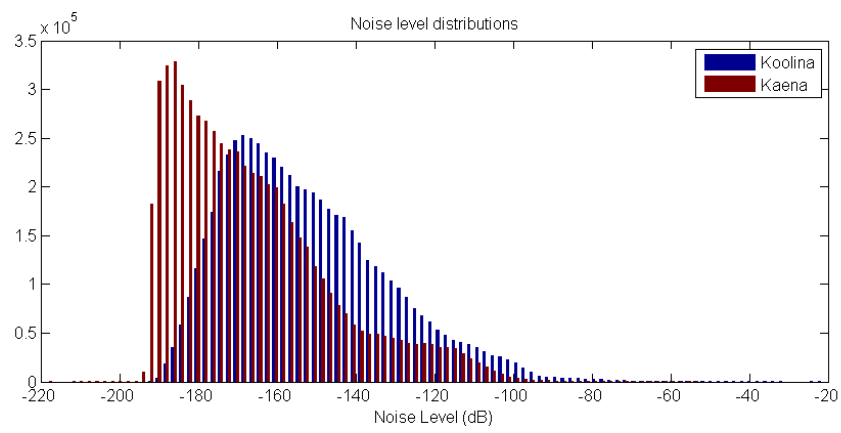
Figure 3.24: Noise distributions for Kaena [red] and Koolina [blue]. Background noise level is -190 dB. The Koolina distribution is shifted towards greater noise values because its angular coverage intercepts Asian RFI sources.
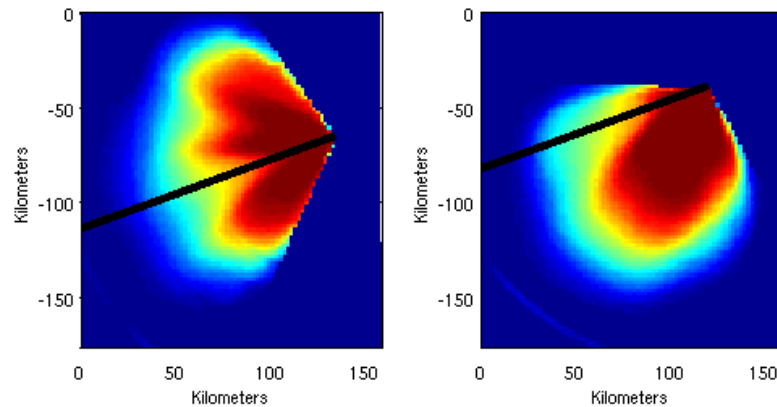
Figure 3.25: Cumulative SNR for the two radar sites. Koolina [left] and Kaena [right]. The external noise source at 201° cartesian [black] directly corresponds to the largest reduction in SNR.

Beamforming was then applied to the Doppler spectra to yield directional information. A consistent source was identified from the noise level estimates at a heading of $-111°$ compass, i.e. $201°$ cartesian. Agreement between independent station estimates was $< 2°$ (Figure 3.25). Range-independence indicated the noise was external interference. External noise sources were the primary cause for reduction in SNR; with the most significant being the $201°$ source.

A great circle with heading of $201°$ from the radar stations intersects Papua New Guinea and northern Australia (Figure 3.26). A possible source for this external interference is the Jindalee Over-the-Horizon Radar (JORN). JORN is a multistatic OTH-B radar developed by the Australian Department of Defence and completed in 2000. Using frequencies between 5 and 30 MHz at 560 kW total power, it achieves an official range of 3,000 km [Colegrove, 2000]. The JORN coverage map roughly corresponds to the $201°$ degree noise source (Figure 3.27).

For inspection of range and angle dependence, the noise level estimates were averaged into bins of both angle and range as a function of time (Figures 3.28, 3.29). Strong diurnal cycles were observed for both sites; the strongest at $201°$, with multiple lesser sources from all angles. The general characteristics were a diurnal cycle of range-independent noise reaching a maximum in the daytime, combined with exponential range-decay at night (Figure 3.29). The diurnal cycling of external interference can be attributed to greater human activity during daylight hours, and sun-driven ionospheric cycles. The exponential range-decay observed at night is characteristic of normal sea echoes
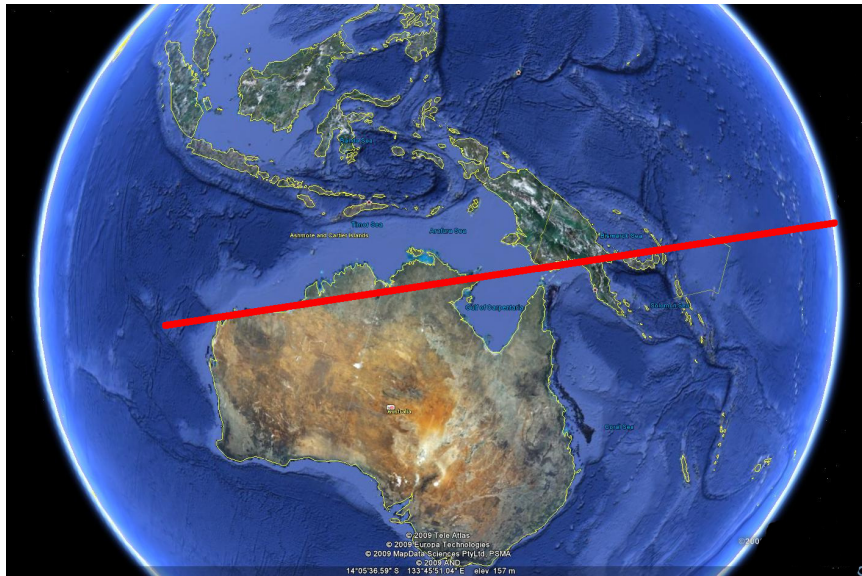
Figure 3.26: 201° vector [red] from radar stations on world map.
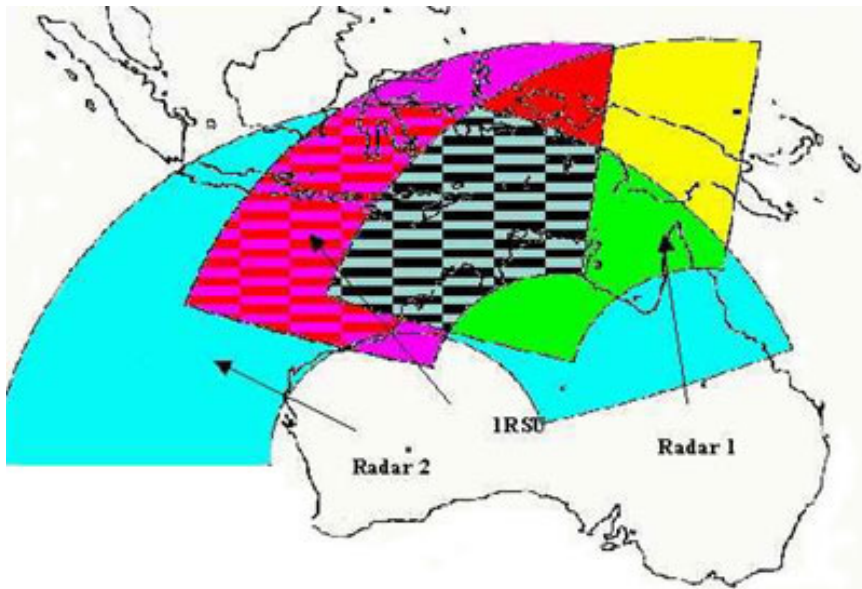
Figure 3.27: Spatial coverage map of the Jindalee Over-the-Horizon radar.
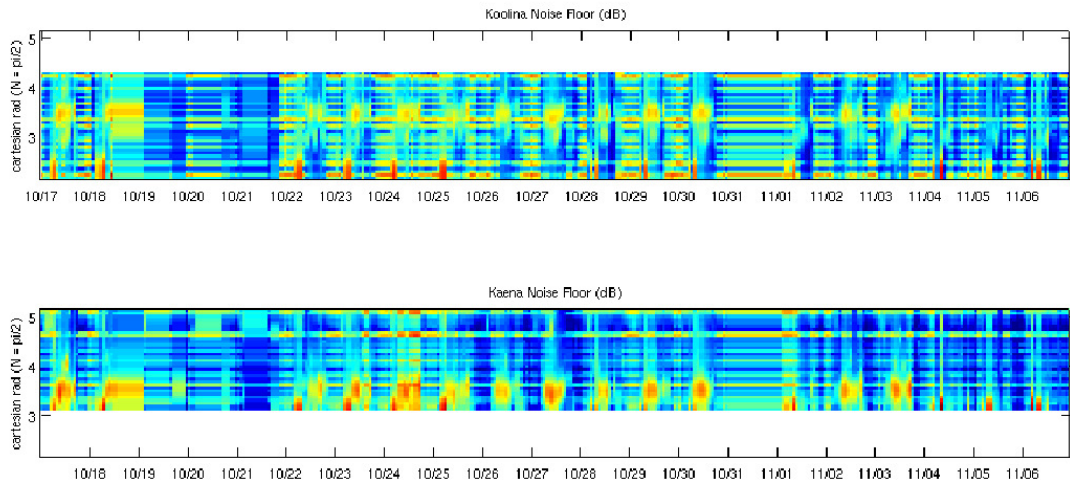
Figure 3.28: Noise as a function of angle and time. Angles have been averaged into 100 equal width bins. Time is on the X-axis. The Y-axis is absolute, i.e. world, angle. Thus a heading of West $= \pi$ would point at the same point at infinite range for both plots. Koolina [top] and Kaena [bottom]. Both sites exhibit a diurnal noise source at 3.5rad $\simeq 200°$.
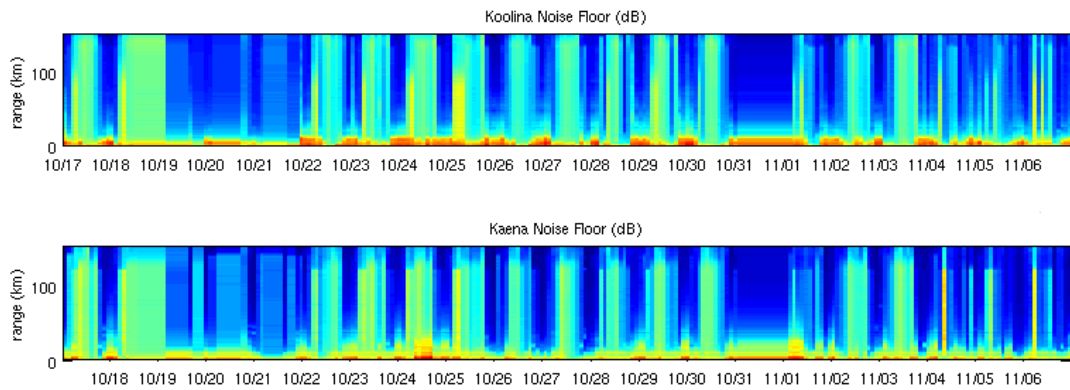
Figure 3.29: Noise as a function of range and time. External interference is seen as range-independent diurnal cycles. Time periods without external interference show exponential decay with range characteristic of normal radar echoes.

66
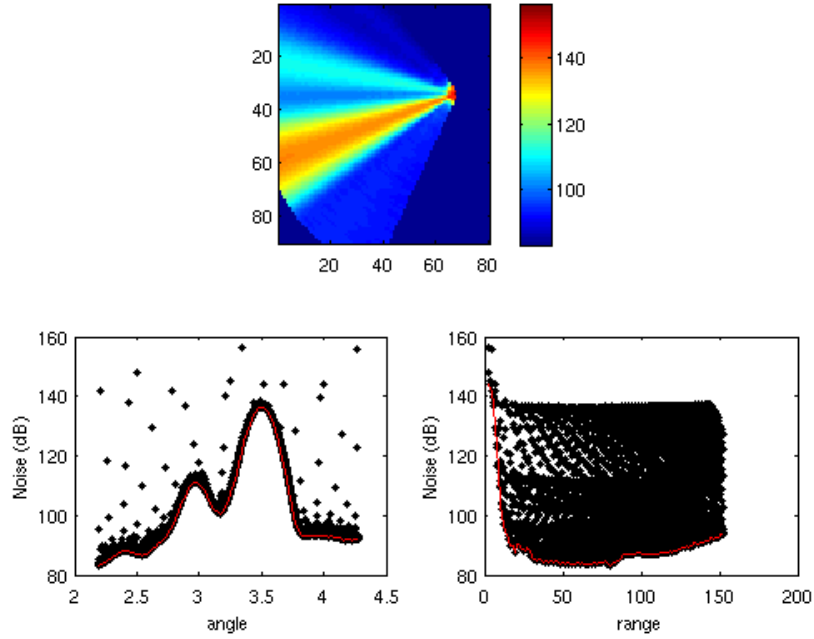
Figure 3.30: Modeling the noise field [top] as a summation of two terms $N = N_I(r) + N_E(\theta, t)$. Assuming both terms approach zero sufficiently often, a minimum-fit can be used to estimate each term. The $N_I(r)$ term exhibits exponential decay. Increasing values in the range minimum past $r = 75$ km are due to the lack of grid cells without external interference. The $N_I(\theta, t)$ term exhibits local maxima in the direction of external interference.

The noise field N can be modeled as a summation of two terms $N = N_I(r) + N_E(\theta, t)$. A time and direction invariant internal source identified by its range-decay function $N_I(r)$, and highly directional diurnal external interferences $N_E(\theta, t)$. Using this simple noise model, it is possible to estimate the two RHS terms assuming the other term reaches zero sufficiently often. From a single time sample with strong external interference, noise was plotted as a function of angle or range using a fit to the minimum values of $N(\theta, t)$ and $N(r)$ (Figure 3.30). This analysis performs slightly better than a bin average, as it allows for separation between the two terms. This method is not sufficiently accurate for further analysis, but is useful for representing the noise in functional form. The results were similar to the bin-average, but the $N(\theta, t)$ term is more coherent (Figure 3.31).

67
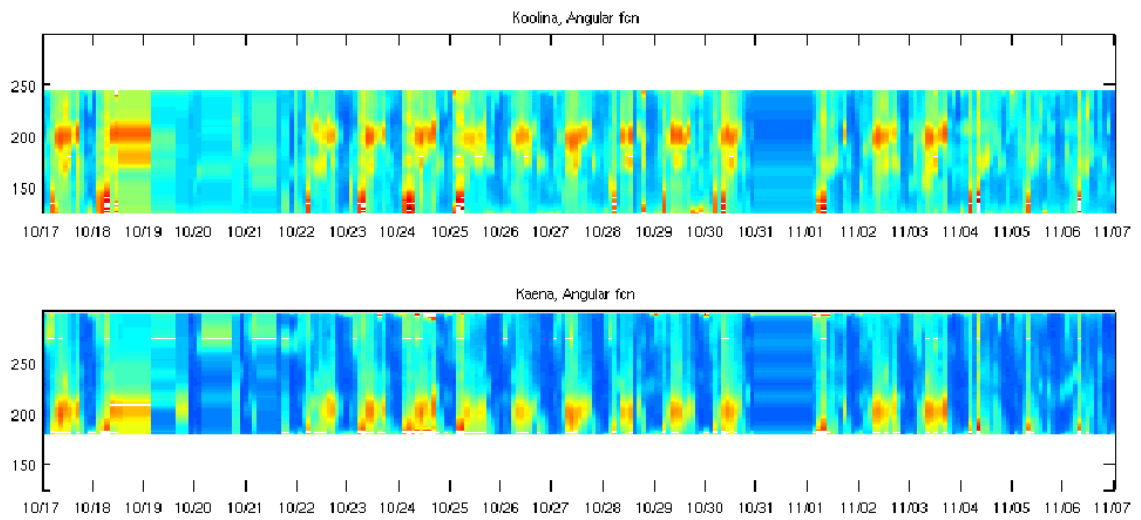
Figure 3.31: Results from the noise model; noise level as a function of angle and time $N_I(\theta, t)$. Both radar sites exhibit the 201° noise source, and Koolina has a very strong intermittent noise source at 125°

3.3.4 Noise Removal

For FMCW radar, transmit signal bandwidth is necessary for range resolution. Larger bandwidths increase the probability of coinciding frequencies with other radio sources. The linear frequency-ramp of FMCW causes periodic "crossings" where the FMCW signal and RFI have equal frequency, and thus the RFI is mixed with the desired ocean signal. This results in a series of amplitude spikes during data acquisition [Gurgel et al., 2006]. These RFI impulses have two distinct characteristics; relatively large amplitude compared to the ocean echo, and short duration approaching a Dirac delta function. The short duration of the RFI impulse is a consequence of the rapid frequency rate of the FMCW causing a short period of intersection. WERA systems operate on relatively low transmit power; made possible by their high dynamic range and amplification of the received echo. A suitable analogy is listening to quiet whispers with a sensitive microphone and amplified headphones. Within such a system, RFI has exceedingly large amplitude. Via the Fourier transform, RFI impulses create strong broad-spectrum noise in the Doppler spectrum.

Recovery of accurate ocean signal requires removal of the RFI, which can be modeled as a sinusoid with varying frequency. Unfortunately, anthropogenic RFI typically uses frequency variation to encode the data content, increasing the complexity of the waveform which must be estimated. This section details two methods employed for the estimation and removal of RFI; eigen-decomposition and direct estimation.

The Multiple Signal Classification (MUSIC) algorithm was developed by Schmidt [1986] as a general, unbiased estimator of radar signal sources from arbitrary locations. Some previous studies utilizing the MUSIC algorithm for noise reduction in oceanographic radar include Molnar et al. [1990] and Ponsford et al. [2003]. The MUSIC algorithm is essentially eigen-decomposition. As this is a well-developed analytical method, the fundamentals of eigen-analysis will not be discussed here. The interested reader is referred to von Storch and Zwiers [1999] for a comprehensive explanation. A summary is as follows:

The return signal is composed of multiple ocean scattering sources and possibly RFI, and can be modeled by the sum of multiple signals. Assume for each antenna n, for $n = 1,...,$N, the measured data at time t is:

$$x_n(t) = \sum_{m=1}^{M} s_m(t) e^{i\omega(t-\tau_{nm})} \tag{3.3.12}$$

where N is the number of antennas, M is the number of signal sources, $s_m(t)$ is the amplitude of the mth source, and τ_{nm} is the relative wavefront delay for a signal source arriving at antenna n

69

as a function of direction. In matrix notation, equation 3.3.12 can be written as $X = AS$. The covariance matrix of the measurements can then be expressed as:

$$R_{xx} = ASA^H \qquad (3.3.13)$$

where A is an $N \times M$ direction matrix, with the column vector a_m associated with the direction of the mth signal. A can also be understood as a beamforming array factor, as in equation C.0.33.

From spectral estimation theory, it is known that the N eigenvectors of R_{xx} can be partitioned into two subsets, spanning a signal and noise subspace, with respective eigenspace indices $m <= d, m > d$. Assuming that RFI corresponds to the largest eigenvalues, the threshold index d is chosen. The RFI-free signal can then be constructed as:

$$X_r = X - \sum_{m=1}^{d} \frac{e_m^H X e_m}{e_m^H e_m} \qquad (3.3.14)$$

Thus MUSIC is straightforward eigen-decomposition of the received signals, with the additional step of calculating beamformed spectra as a function of direction. The covariance matrix is calculated as antenna covariance. The threshold d can be data-adaptive or predetermined, with the goal of separating RFI from the uncorrelated ocean scatter.

The MUSIC algorithm was applied to a time period of strong RFI noise. The resulting eigenvalues had uniform difference, with no clear indication of noise vs. signal subspaces. The greatest eigenvalue was chosen to estimate the noise eigenspace. The resulting spectrum X_r had no significant reduction in noise (Figure 3.32).

A similar alternative to the MUSIC algorithm is an eigen-decomposition of the range covariance matrix [Jun et al., 2004]. Since RFI is known to have temporal range coherence, it is reasonable to expect this variation could be limited to a distinct subspace.

For this analysis, the same data sample was beamsteered directly at the RFI source using a linear array factor (Figure 3.33). Strong, range-independent eigenfunctions were found, indicative of RFI noise (Figure 3.34). The ocean signal energy did not map to a separate eigenspace, but rather overlapped the same eigenmodes as the RFI. To clarify, the form of the RFI eigenmodes was resolved by high-pass filtering the spectrum to include only the higher noise frequencies, i.e. remove all ocean signal (Figure 3.35). Attempts at filtering the spectra using only the stronger, range-independent noise eigenmodes were unsuccessful at removing the RFI.

An alternative effort was made to subtract the RFI via direct estimation of its amplitude and phase. The amplitude was estimated independently for each frequency as the mean energy for
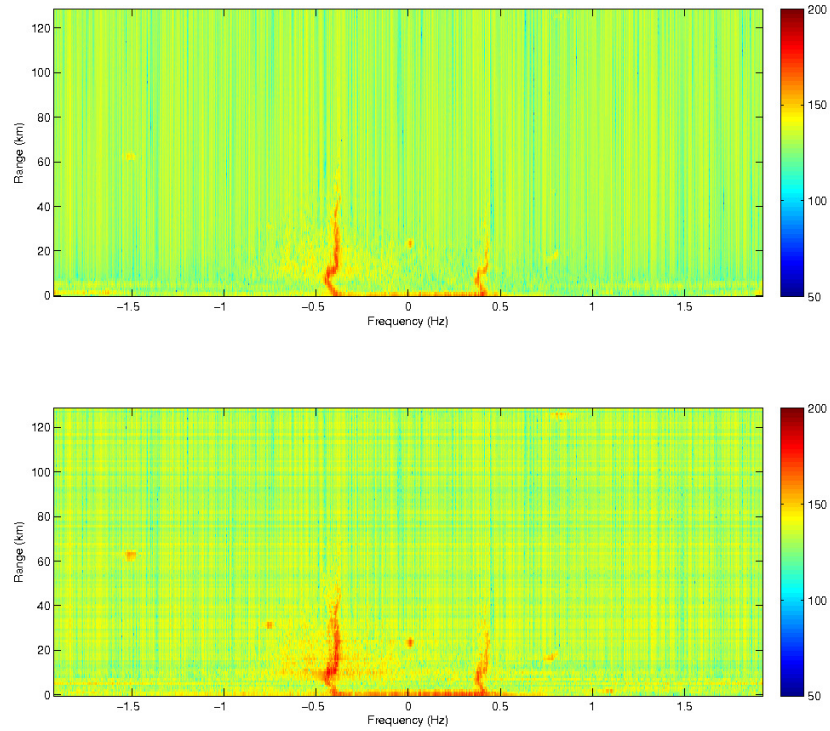
Figure 3.32: Results from the MUSIC algorithm. The original raw spectrum [top] was chosen for characteristically strong RFI noise, seen as range-independent bands spanning the entire frequency axis. The MUSIC-filtered spectrum [bottom] showed no significant reduction in noise.
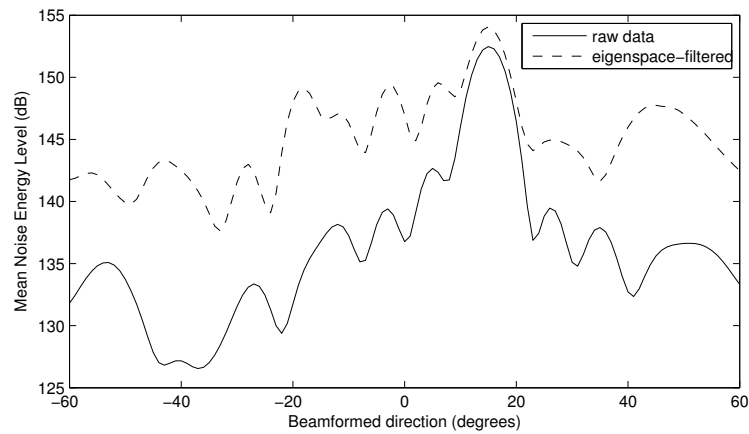
Figure 3.33: Mean noise level as function of beam-steered direction. Angles are taken relative to radar look direction, i.e. 0 degrees is straight ahead. The dominant RFI source is at 15°. Strong sidelobes are due to the linear array factor used, which is equivalent to a discrete space Fourier transform using a boxcar window. Eigenspace filtering actually increased the noise energy.

71
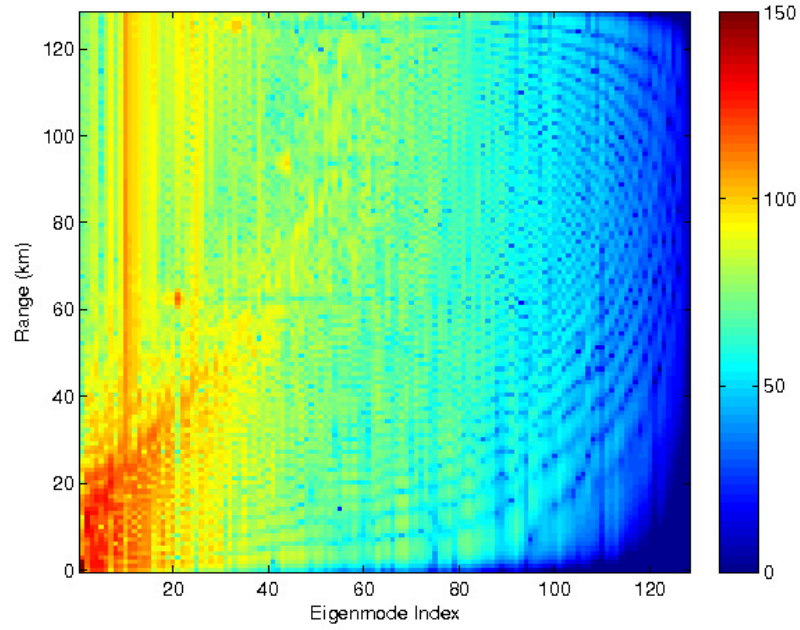
Figure 3.34: Range eigenfunctions. Strong, range-independent eigenfunctions are seen around index 20, indicative of RFI noise. The ocean signal energy is mapped across half of the eigenmodes (0:60), with no clear eigenspace structure.
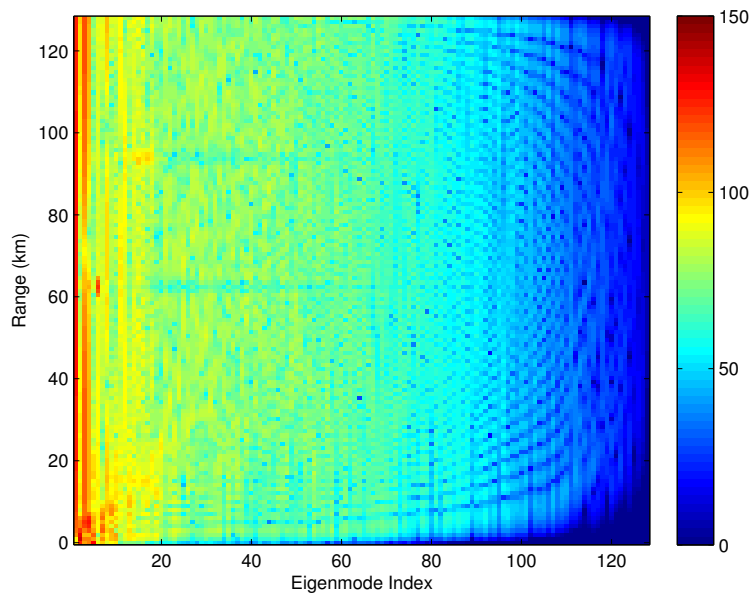
Figure 3.35: Range eigenfunctions of hi-pass filtered, noise-only data. The general form of the eigenfunctions remains unchanged, without the overlying ocean signal energy.
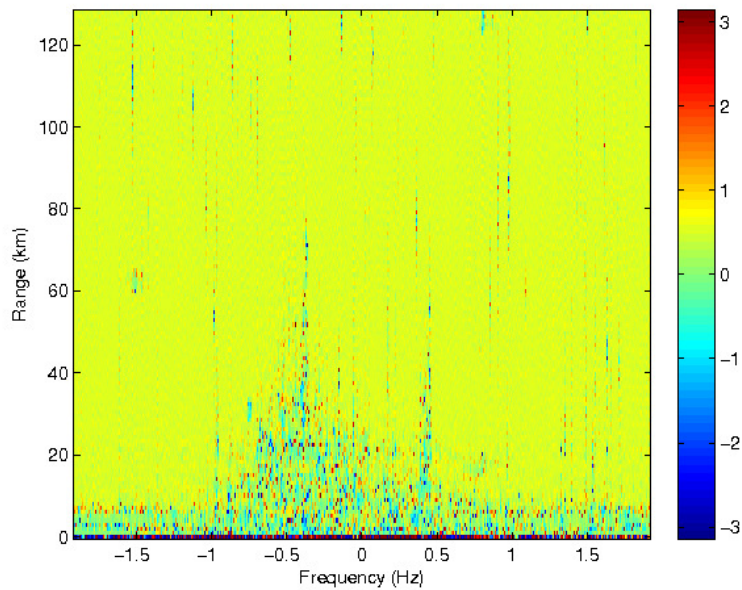
Figure 3.36: Phase difference of RFI with range. For this time sample, a constant gradient of 0.25 rad km^{-1} was observed. The phase difference becomes randomly distributed when the RFI is mixed with ocean signal.

the farthest 20 km of range cells, with the assumption the energy at this range is predominantly RFI or thermal. For spectra with strong RFI, the phase difference between ranges was nearly constant across all noise frequencies, suggesting a linear relationship between the FMCW waveform and RFI (Figure 3.36). In the nearfield, the received signal was a mix of RFI and ocean scatter, resulting in randomly distributed phase differences. Following the harmonic addition theorem, the phase difference between the desired ocean signal and RFI noise is a random variable, and consequently the received amplitude will randomly vary with constructive and destructive interference. Subtracting the estimated RFI resulted in a nearly 100% reduction for a narrow range band centered at the furthest ranges (Figure 3.37). Outside of this range band, the RFI rapidly returned to its original value. Inspection of individual frequency bands showed errors exceeding $O(0.01)$ rad in estimating the RFI phase caused additional energy to be added (Figure 3.38). Further efforts at estimating the correct RFI phase from data were unsuccessful.
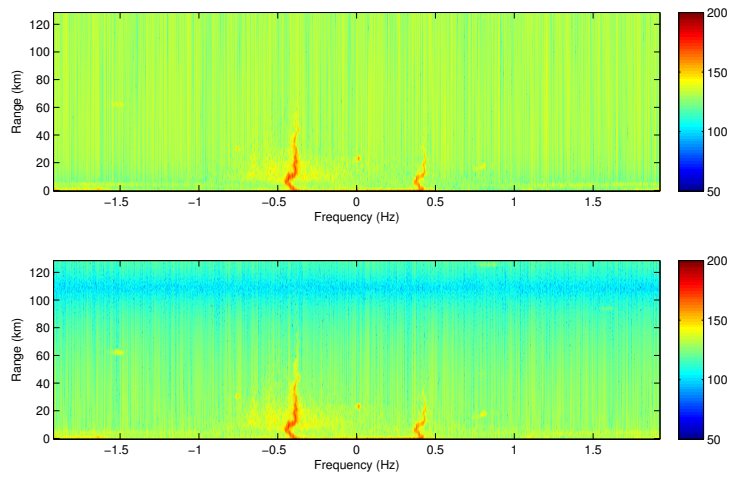
Figure 3.37: Estimated RFI subtraction. The simple linear subtraction works quite well for a narrow range band of 5 km centered at 110 km.
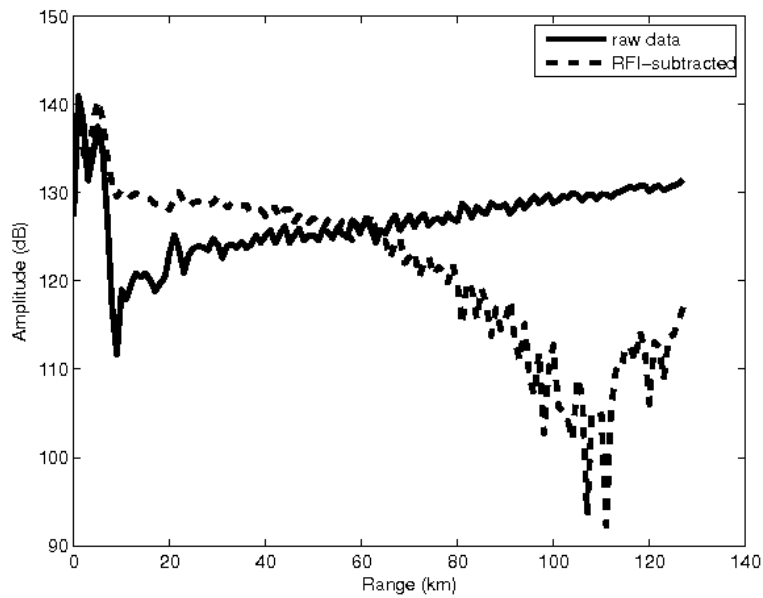
Figure 3.38: The effect of subtracting RFI noise with an incorrect phase estimate. A single frequency band is shown, chosen outside the frequency range of ocean scattering. Thus the raw data represents entirely RFI noise. At 110 km, the RFI phase estimate is accurate, and the amplitude is reduced ~ 30 dB. At 60 km, the phase estimate is $\pi/2$ radians out of phase, and no cancellation occurs. By 20 km, the phase estimate is π radians out of phase, and energy is added to the spectrum.

74

3.4   Significant Waveheight Regression Analysis

To further inspect the effects of RFI on radar-derived H_s estimates, linear regression analysis was performed on the H_s estimates from both algorithms. The 21 day study period, with N = 1222 temporal samples were linearly regressed to the CDIP buoy timeseries. Outside the directions of external interference, correlation coefficients were highest; 0.6 and 0.9 for the GS and WERA algorithms, respectively. Spatial regions with the highest correlation had slope and offset of 1,0 (Figures 3.39, 3.40). Combining estimates from both sites improved overall accuracy, but reduced peak accuracy; i.e. maximum correlation and RMS error, and introduced spatial discontinuities. Poor accuracy occurred near $200°$ cartesian, i.e. the direction of the dominant RFI source.

The same regression analysis was repeated after removing time samples with noise levels $N > 50$ dB, in an angular region centered at $200°$. The entire spatial field was removed for these time samples to prevent spatial bias in the correlation. Regression results were significantly improved in the region $200°$, yielding increased coefficients of determination and decreased RMS error (Figure 3.40, 3.41).
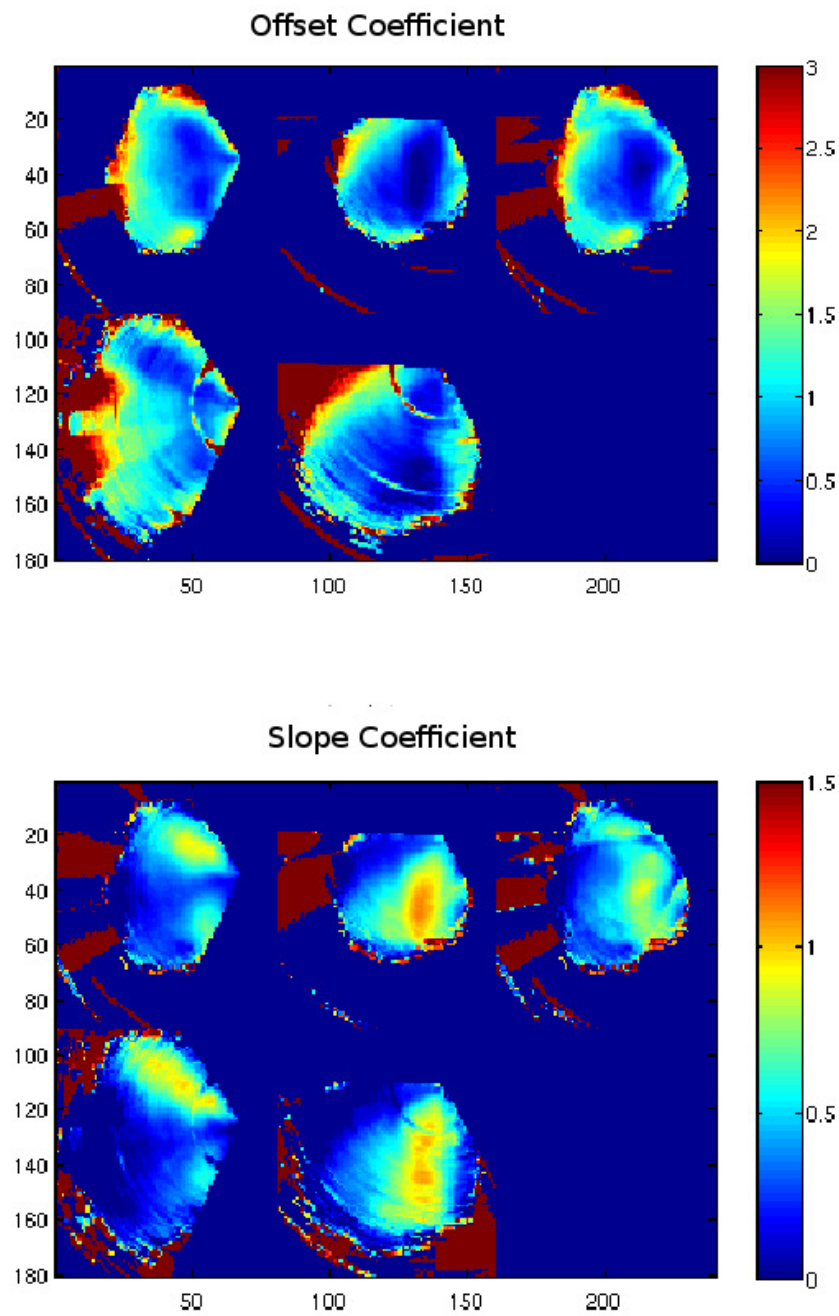
Figure 3.39: H_s linear regression coefficients. WERA [top] and GS algorithm [bottom]. Koolina [left], Kaena [center], site-combined [right]. Units for the offset are meters.

76
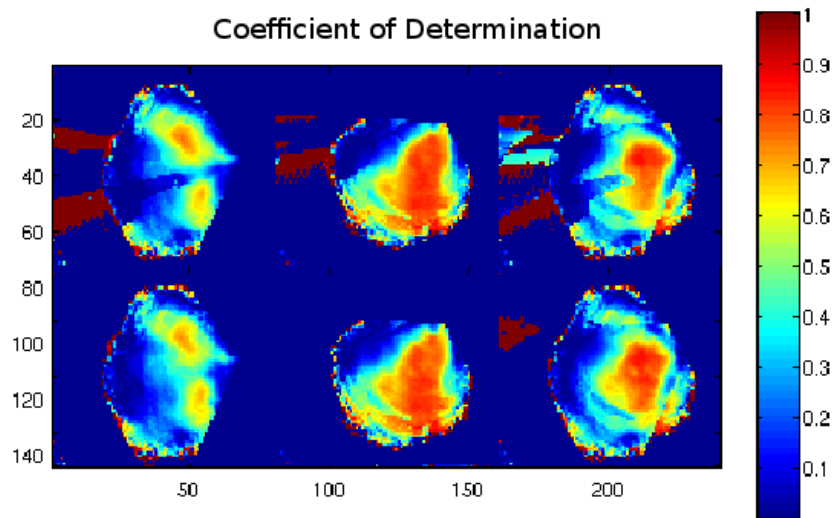
Figure 3.40: H_s linear regression coefficient of determination for the WERA algorithm. Before [top] and after [bottom] noise filtering in the direction of $200°$ cartesian. Koolina [left], Kaena [center], and site-combined [right]. Removing the noise-contaminated data improved accuracy, with similar results for the GS algorithm.
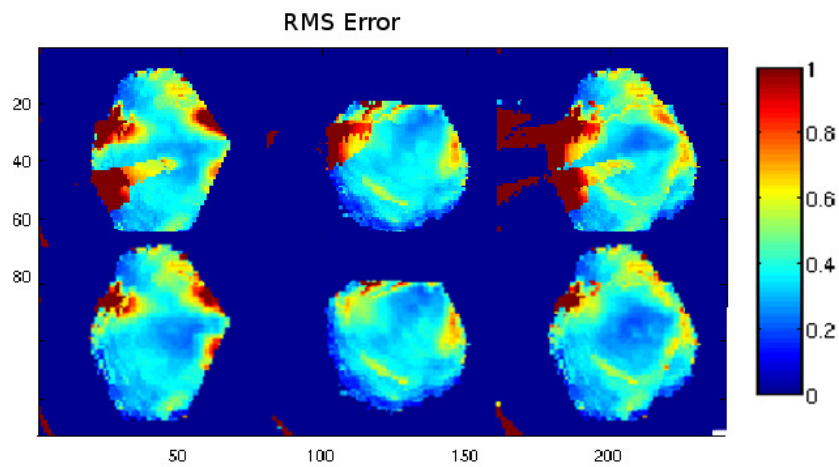
Figure 3.41: H_s RMS error between the Waimea buoy and radar regression model for the WERA algorithm. Before [top] and after [bottom] noise filtering in the direction of $200°$ cartesian. Koolina [left], Kaena [center], site-combined [right]. Again, accuracy is improved by removing noise-contaminated samples.

3.5 Electromagnetic Scattering: Second Order Integral

Weber and Barrick [1977] identified conditions in which the dominant wave direction is perpendicular to the radar beam as being error prone for the H_s equation 1.5.5. Barrick [1977] concluded the H_s equation was weakly dependent on the radar-wave direction. Maresca and Georges [1980] noted failure of the H_s equation on highly directional synthetic spectra, due to the increased sensitivity of the S2 energy to direction. As discussed in the proceeding section, the H_s spatial variation could not be fully explained in terms of a signal-to-noise relationship. Thus an analysis of the second order integral relation was motivated.

As derived by Derr [1972], the second order integral relation, hereafter S2 integral, is:

$$\sigma_{vv}(\omega_D) = 16\pi k_0^4 \sum_{\pm} \int_{-\infty}^{\infty} \int_{-\infty}^{\infty} d\boldsymbol{k} |\Gamma_T(\pm\boldsymbol{k_1}, \pm\boldsymbol{k_2})|^2 W(\pm\boldsymbol{k_1}) W(\pm\boldsymbol{k_2}) \delta(\omega_D \pm \omega_1 \pm \omega_2) \quad (3.5.1)$$

where $\sigma_{vv}(\omega_D)$ is the second order Doppler energy, $\boldsymbol{k_1}, \boldsymbol{k_2}$ are the interacting first order ocean wavevectors, $W(\boldsymbol{k})$ is the directional spatial waveheight spectrum of the ocean, and Γ_T is the combined electromagnetic and hydrodynamic coupling coefficient, hereafter coupling coefficient.

The first fundamental theoretical constraint for second order scattering is the Bragg resonance condition $\boldsymbol{k_1} + \boldsymbol{k_2} = \boldsymbol{k_B}$, where $\boldsymbol{k_B}$ is the Bragg wavevector. For this discussion and dataset, a backscattering configuration was used, and thus the Bragg wavevector is exactly twice the radar wavevector; $\boldsymbol{k_B} = 2\boldsymbol{k_r}$. The second constraint is expressed in the S2 integral as $\delta(\omega_D \pm \omega_1 \pm \omega_2)$. That is, the observed Doppler frequency ω_D for a given pair of ocean wavevectors is determined by their frequency sum. To clarify, the integral is over all ocean wavevector space, allowing for all possible second order combinations. The two $W(\boldsymbol{k})$ terms are restricted to the Bragg resonance vector relation. Similarly for the coupling coefficient. The Doppler frequency ω_D at which each second order wavevector combination will be observed, is determined by their frequency sum $\omega_D \pm \omega_1 \pm \omega_2$. Additional complexity is added by the summation term $\sum_{\pm}$, which is a consequence of deriving the S2 integral as an average.

For numerical evaluation and visualization, it is easiest to express the ocean wavevectors as symmetrical about the integration wavevector $\boldsymbol{k_1} = 1/2\boldsymbol{k_r} + \boldsymbol{k}$, $\boldsymbol{k_2} = 1/2\boldsymbol{k_r} - \boldsymbol{k}$.

The two aforementioned constraints on second order scattering define four independent Doppler frequency surfaces in wavevector space (Figure 3.42). The $\omega_D + \omega_1 + \omega_2$ and $\omega_D - \omega_1 - \omega_2$, hereafter summation frequencies, only contribute to Doppler frequencies $|\omega_D| > f_B$. Conversely, the the $\omega_D + \omega_1 - \omega_2$ and $\omega_D - \omega_1 + \omega_2$, hereafter difference frequencies, only contribute to Doppler
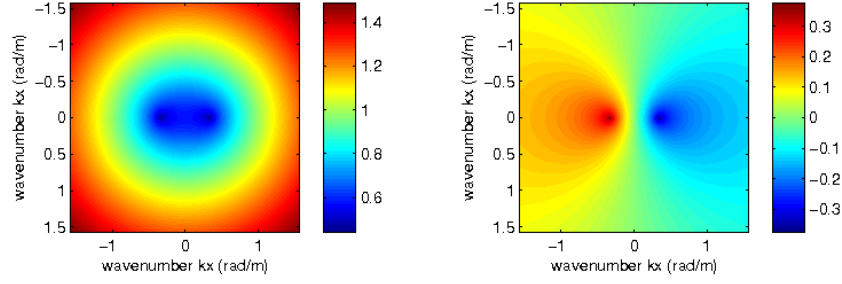
Figure 3.42: Observed Doppler frequency as a function of ocean wavevector as defined by the second order integral. Horizontal and vertical axis correspond to ocean wavenumber to the East and North, respectively. The color axis defines Doppler frequencies in Hz. The left and right figures correspond to ocean summation and difference frequencies, respectively. Note that the figures are separated by the Bragg frequency of 0.48 Hz. The left figure corresponds to absolute Doppler frequencies *greater* than the Bragg peak, i.e. outer S2 bands. The right figure corresponds to absolute Doppler frequencies *less* than the Bragg peak, i.e. inner S2 bands.

frequencies $|\omega_D| < f_B$. The energy at a given Doppler frequency ω_D is the sum of contour integrals in each of these wavevector spaces.

Wavevector singularities occur at $|\omega_D| = 2^{1/2} f_B$. An interesting result of this analysis is that the summation frequencies approach a nearly linear relation to ocean wavenumbers for $k > 1.5$ rad m^{-1}, corresponding to Doppler frequencies $|\omega_D| > 1.5$ Hz (Figure 3.42, left plot). For the difference frequencies, the relationship is quite different, as the contour integrals are over wide range of ocean wavenumbers. The integral spans a greater range of wavenumbers as the Doppler frequency decreases. This explains the fundamentally different Doppler spectral shapes observed for the inner and outer second order sidebands.

The coupling coefficient Γ_T is the sum of an electromagnetic Γ_{EM} and hydrodynamic Γ_H terms. They arise as a result of the second order perturbation expansion for the electromagnetic and hydrodynamic equations, respectively. A major consequence of the H$_s$ equation is that these terms are taken as an average for each Doppler frequency. The electromagnetic term is more significant in nearly all directions, and is the exclusive contributor at Doppler frequency $\omega_D = 2^{3/4} f_B$ (Figure 3.43). The response at this frequency seems to scale as the sine of the angle between the radar and ocean wavevectors. These results agree with the coupling coefficient description given in Barrick and Weber [1977]. Averaging the total coupling coefficient over all directions results in a spatial-mean coupling coefficient as a function of Doppler frequency (Figure 3.45). Inspection of this mean coupling coefficient shows the hydrodynamic $2^{1/2} f_B$ and EM $2^{3/4} f_B$ contributions remain, despite
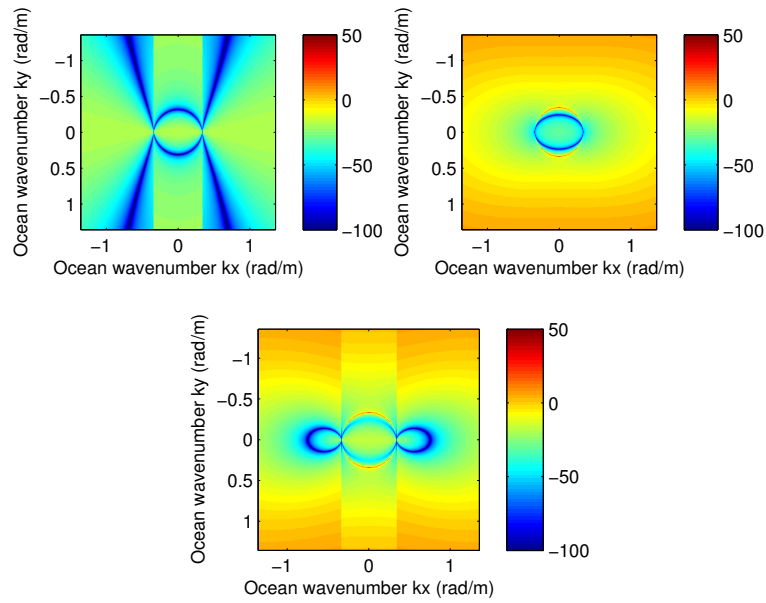
Figure 3.43: The hydrodynamic [top left], electromagnetic [top right], and combined [bottom] coupling coefficients. The electromagnetic term has a strong response at Doppler frequency $\omega_D = 2^{3/4} f_B$, orthogonal to the radar beam.

their decay to zero for some directions. This is a consequence of averaging; strong contributions for a narrow range of directions will dominate the average.
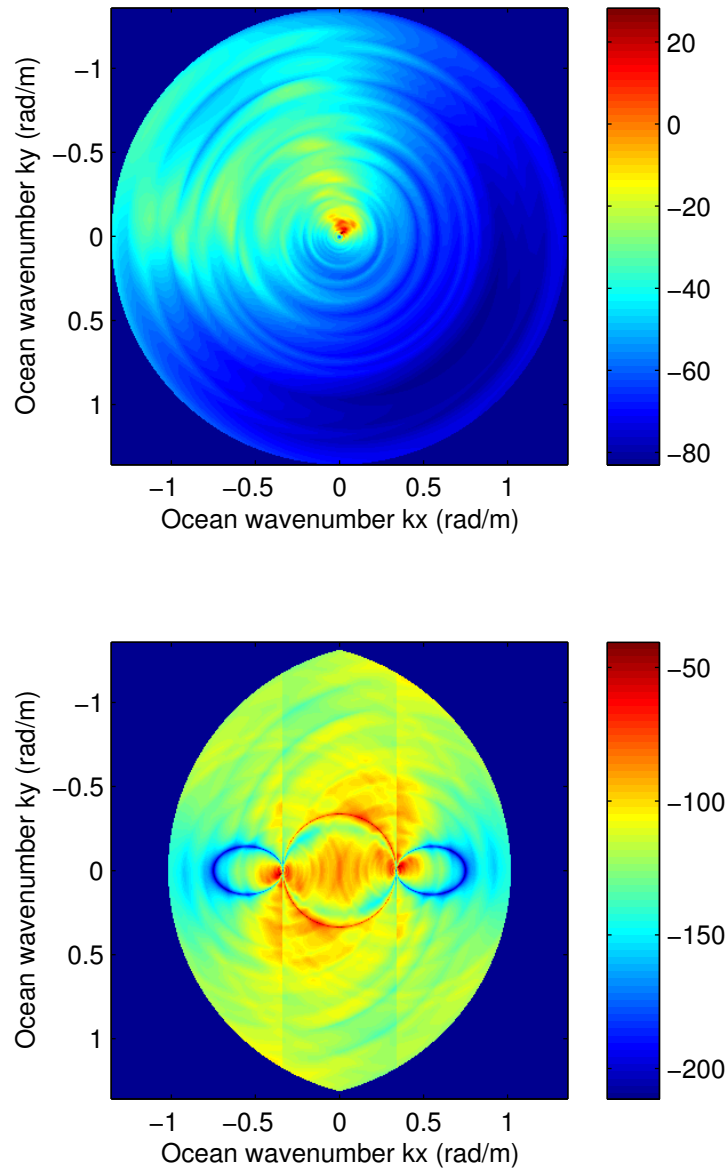
Figure 3.44: An example of the S2 integral using a buoy directional spectrum. No clear distinction or mapping of the ocean wavevectors can be found
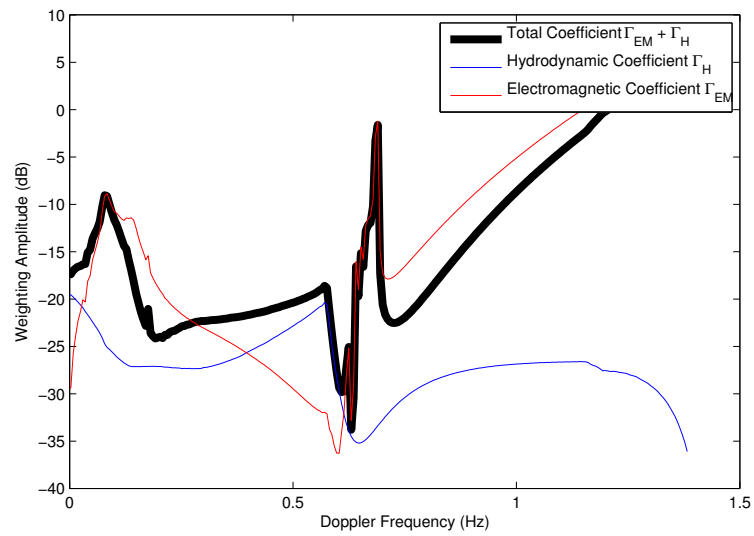
Figure 3.45: The Doppler frequency-averaged Coupling coefficient. The total coefficient Γ_T [black], is shown with its contributions from EM term Γ_{EM} [red] and hydrodynamic term Γ_H [blue]. The hydrodynamic $2^{1/2}f_B$ and EM $2^{3/4}f_B$ contributions remain, despite their decay to zero for some directions.
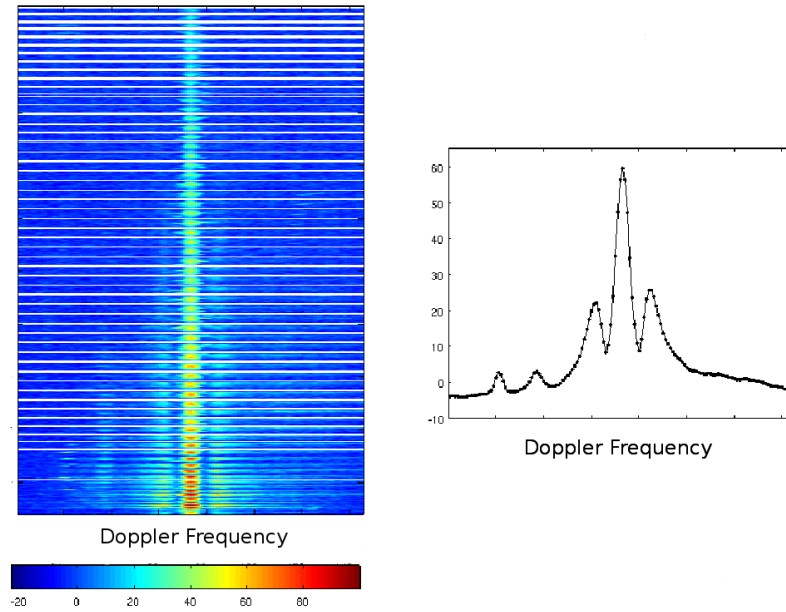
Figure 3.46: An example of spectral averaging. Spectra from a single time sample with sufficient SNR [left] are averaged over frequency to yield a mean Doppler spectrum [right]. Because the spectra have not been normalized by the S1 energy, the result is biased towards the greater SNR spectra.

3.6 Spectral Averaging

Various methods of Doppler spectral-averaging were investigated as a possible means to reduce H_s error. Prior to averaging, the Doppler shift was estimated and removed. Two conditions restrict spectral averaging to a small spatial region. First, spectra should not be averaged over a wide range of angles, as first and second order energies vary with angle (see §3.5). Second, spectra should not be averaged over a wide range of SNR, as the resulting mean spectrum will have S2 sidebands which have been whitened and biased low from noise energy (Figure 3.46). Normalizing the spectra by their respective S1 prior to averaging will increase the sideband amplitudes, but does not add accuracy to the H_s result (Figure 3.47). Discarding spectral outliers decreased the accuracy (Figure 3.50). Coefficients of determination were $r^2 = 0.31, 0.87$ and RMS error was 1.24,0.46 m for outlier rejection and median average, respectively.

Averaging spectra which exceed a threshold SNR did not improve the H_s estimate. The mean spectra were contaminated by strong noise peaks(Figure 3.48). The Bragg peak had relatively

83
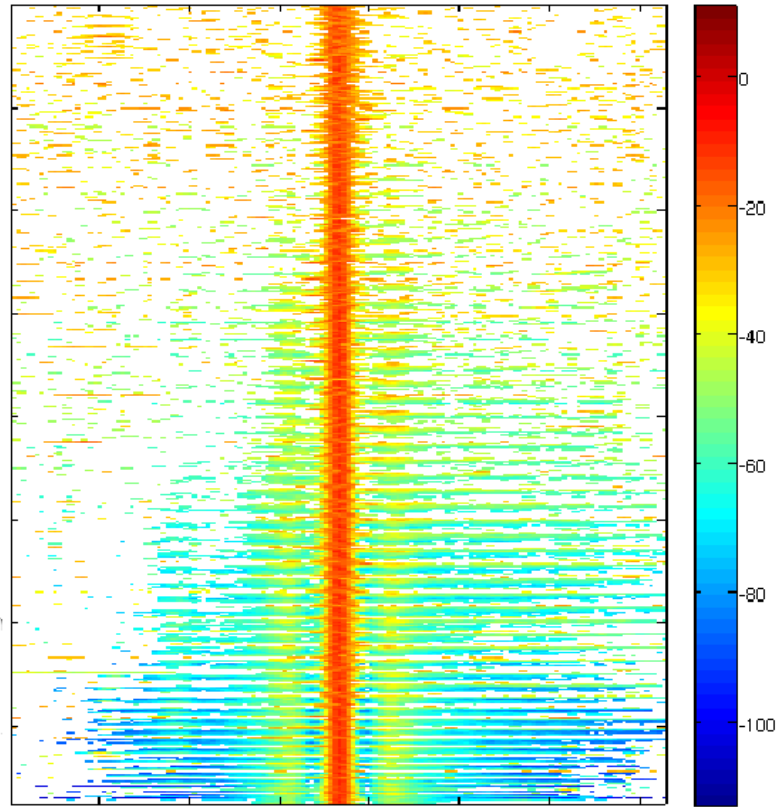
Doppler Frequency

Figure 3.47: Example spectrogram normalized by S1 energy. Spectra are from a single time sample. Spectral frequencies below the noise floor have been removed. Noise energy persists at the farthest ranges due to variance about the mean noise level. The y-axis corresponds roughly to increasing range.
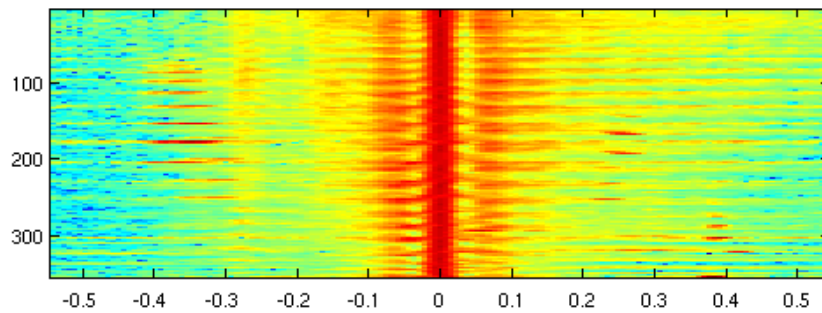
Figure 3.48: A close-up of a spectrogram normalized by S1 energy. Spectra below a threshold SNR have been removed. Strong S2 sidebands and S1:S2 nulls are evident in most spectra. Multiple spurious noise peaks exist for some S2 sidebands.
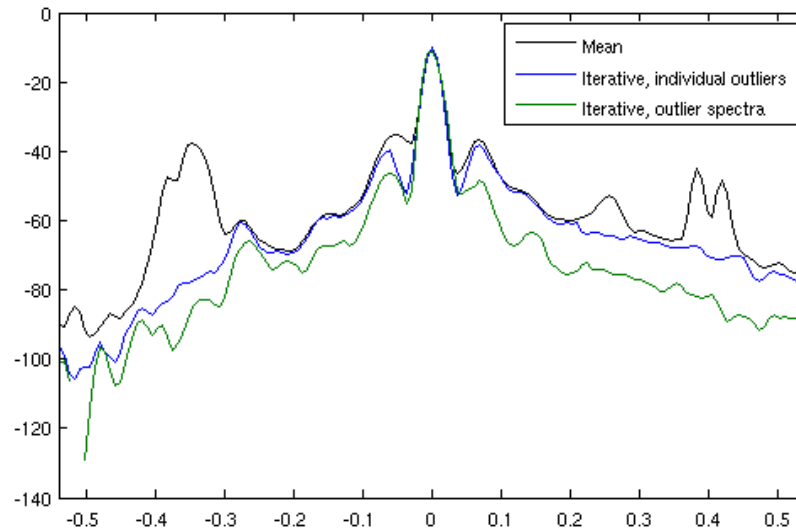
Figure 3.49: Two methods for improving the spectral average by removing outliers (3σ). The mean spectrum [black] is contaminated with noise peaks at ~ 0.4 Hz. Removing individual outliers retains more S2 energy [blue], while discarding entire spectra decreases S2 energy [green]. For a buoy H_{m0} of 4.42 m, the corresponding radar estimates were 4.97, 3.48, and 2.06 m, in legend order.

little amplitude variation. Iteratively discarding large variation (3σ) spectral outliers improved the form of the sidebands; retaining physical features while discarding noise peaks (Figure 3.49). Although this method produced visually improved spectra, H_s accuracy did not increase.

Spectral averaging was used to investigate the time evolution of the Doppler spectra. The sidebands exhibited low-frequency peaks moving towards higher frequencies with time, analogous to the arrival of distant swell (Figure 3.51). Following scattering theory, the frequency difference between first and second order peaks decreased for more energetic swell.
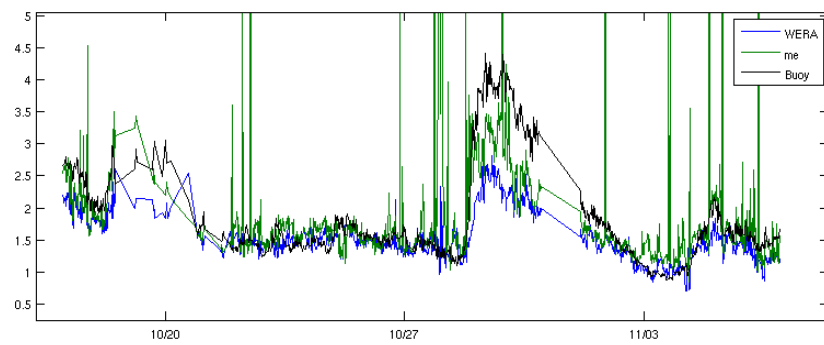
Figure 3.50: Comparison of H_s timeseries for buoy [black], WERA median [blue], and spectral-average [green]. The spectral average was calculated using spectra with sufficient SNR, and discarding 3σ outliers. Coefficient of determination was $r^2 = 0.87, 0.31$, and RMS error was 0.46, 1.24 m for this method and a median average, respectively.
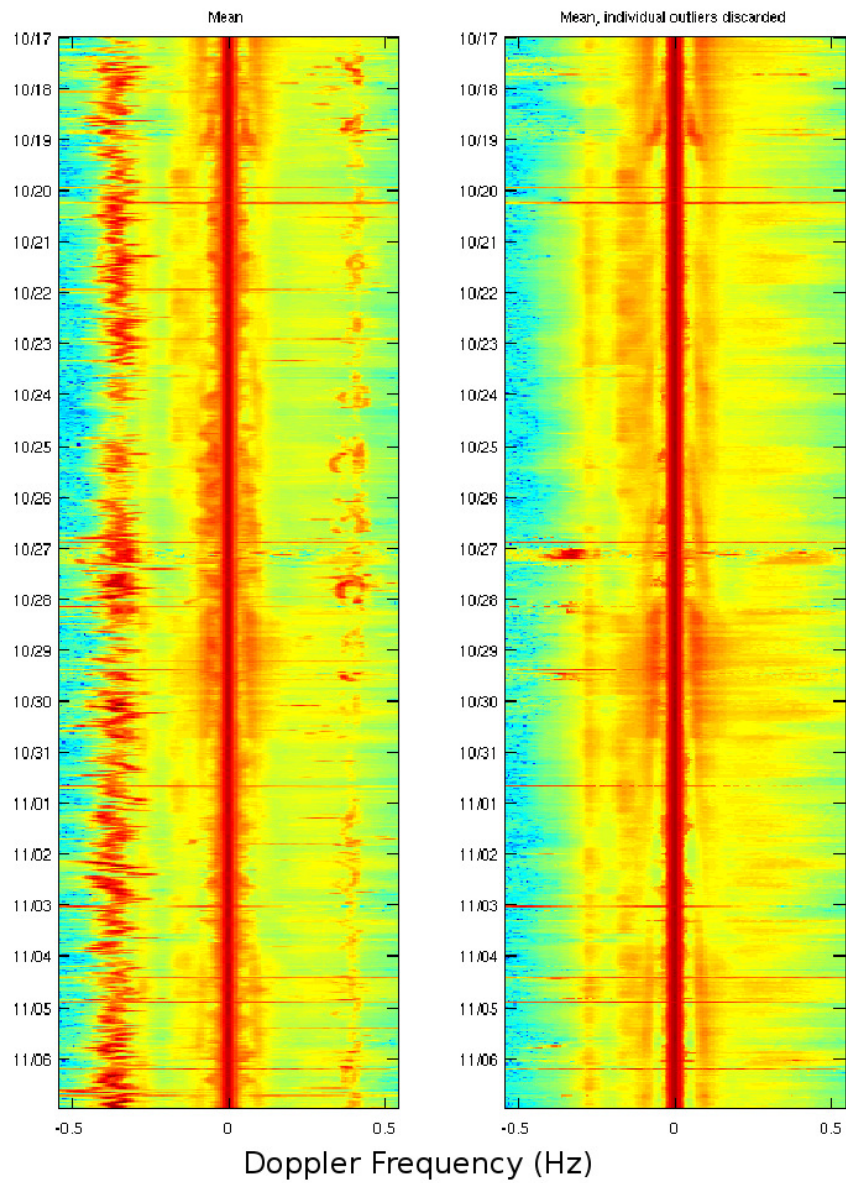
Figure 3.51: Time evolution of spectra, showing improvement to the spectral mean by removing spectral outliers. The mean spectrum [left] is contaminated with noise peaks at $\pm$ 0.4 Hz. After removing outliers [right], time-varying characteristics of the S2 region are revealed.

Chapter 4

Discussion

4.1 Wind Estimates

The Bragg-ratio method of Long and Trizna [1973] has remained essentially unmodified since its inception, although debate over the directional spreading model continues. Its utility for physical analysis is somewhat reduced because it can not estimate wind magnitude. A possible method for adding magnitude to the wind estimates would require inferring the ocean Bragg wave amplitudes from the Doppler spectra (see Eqn. A.4.5), and entering these into an appropriate wind-wave model. Inference of Bragg wave amplitudes from the second order spectrum would require inversion of the second order integral equation. Provided the Bragg wave amplitudes could be reasonably estimated, considerations must be made for growth and response times due to changing winds [Masson, 1990].

Complex correlation between radar and modeled wind directions was quite poor. Conversely, radar wind directions were highly correlated ($r^2 = 0.83$) to QuickSCAT measurements. Agreement between these two empirical measurements is additional validation of the Long and Trizna [1973] wind direction method. The bimodal wind fields observed in the radar measurements are interesting features warranting further investigation.

Further analysis of the radar wind fields must take consideration for the imposed directional spreading function, and the limited dynamic range of observable Bragg ratios, which constrain the measurable angles. This effect has been noted by previous researchers [Maresca and Georges, 1980, Harlan and Georges, 1994, Wyatt, 2001, Gurgel et al., 2006], and was observed in this study. For winds nearly parallel to the radar beam, the radar-to-wind angle exceeds it measurable range and a discontinuity in the spatial field is created. An algorithm is necessary which accounts for this expected discontinuity without introducing a directional bias.

4.2 Significant Waveheight Estimates

Theoretical and observational analysis shows the H_s equation is inaccurate for $k_0 h_{rms} <$ 0.1 [Barrick, 1977]. Combining the upper and lower validity limits gives $0.1 < k_0 h_{rms} < 4$. H_s observations from this study varied from 0 to 5 m, and were thus within the constraints of theoretical validity. For the HOME radar, the lower limit of theoretical validity was 0.5 m.

Correlation analysis between the Waimea buoy and the radar-derived H_s showed external interference as the primary cause for radar H_s error. The lower SNR of the second order region reduces the wave measurements to 50% of the range for current measurements. Station-averaging H_s estimates with varying SNR created spatial discontinuities in accuracy unsuitable for further analysis. Removing low SNR data was shown to improve correlation and RMS error. Maximum accuracy did not correspond with maximum SNR, possibly due to non-linear effects in the radar receivers for the nearest range cells. Poor correlation at outermost angles of the measurement field may be attributed to decreased beamforming directionality, i.e. wider centerlobes and greater side-lobes. A variety of different averaging and filtering methods were unsuccessful at improving H_s accuracy.

The decreasing frequency separation for first and second order peaks is a possible explanation for additional error in H_s estimation. Peak second order values occur closest to the Bragg peak, and move closer to the Bragg peak for lower frequency peak ocean swell [Barrick, 2005a]. An instrumental limit is reached when the S1:S2 separation is less than the spectral resolution (which will exceed df due to spectral filters). At this limit, the S1 and S2 energies are convolved, causing H_s to be underestimated by biasing the S2/S1 ratio towards unity. This effect explains the observed underestimation of H_s at large H_s (Figure 4.1). For this experiment, the saturation limit was $H_s = 11.9$ m, whereas S1:S2 merging was possibly observed at 4 m. This suggests the merging is due to spectral resolution, and not a physical limitation of the radar. Further evidence of S1:S2 merging is the under-estimation of H_s for peak swell in the timeseries.

Evaluation of the S2 integral equation showed the coupling coefficient varied significantly with direction. Previous researchers have concluded the H_s equation is insensitive to direction [Barrick, 1977, Maresca and Georges, 1980]. Although, their evaluations were based on synthetic wave models with symmetric directional spread and no representation for multi-mode seas. Barrick [1977] estimated the error associated with the assumption of a mean coupling coefficient on the order of 15%. Both researchers noted increased H_s error for $k_0 h < 0.3$ m. This suggests the
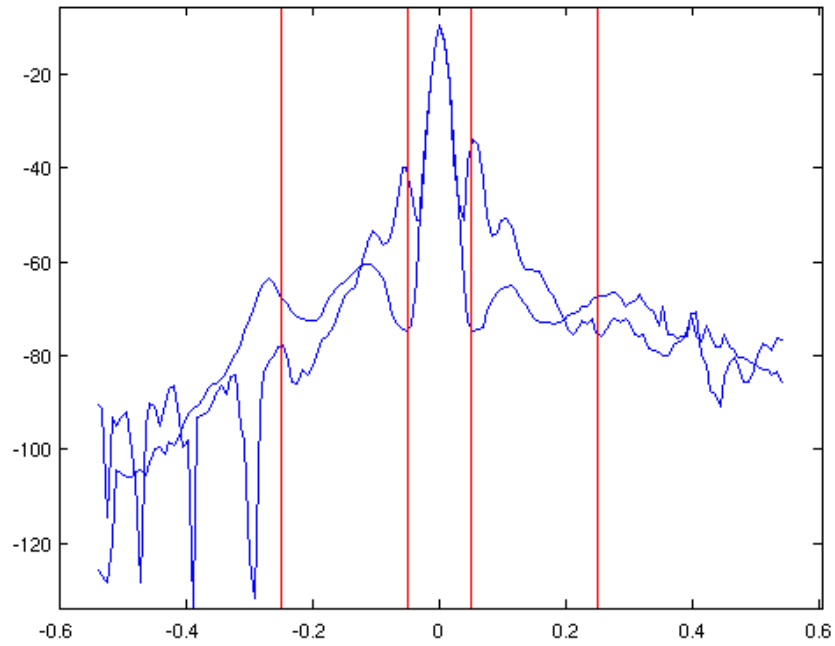
Figure 4.1: Merging of first and second order peaks. Spectrum from two different time samples are shown, corresponding to greater and lesser H_s. The lesser H_s is characterized by decreased second order peaks separated by a greater frequency difference from the Bragg peak. Note that both spectra have equal Bragg peak amplitude, i.e. equal signal gain. WERA algorithm S2 integration frequency limits are indicated in red.

coupling coefficient becomes more directionally dependent for higher ocean frequencies. Maresca and Georges [1980] noted poor accuracy for highly directional spectra.

The S2 integral summation frequencies approach a nearly linear relation to ocean wavenumber for $k > 1.5$ rad m^{-1}, corresponding to Doppler frequencies $|\omega_D| > 1.5$ Hz. The frequencies are far outside the significant contribution to second order energy. This raises questions about the theoretical validity of empirical fits between the scalar ocean spectrum and the Doppler spectrum, as used in the WERA algorithm. The energetic lower Doppler frequencies are integrals over a large range of ocean wavenumber and direction. Theoretical work by Barrick [1972], Weber and Barrick [1977], Barrick and Weber [1977] has shown this simple proportionality to be incorrect. Furthermore, linear regression between the Doppler spectrum and ocean spectrum is unlikely to resolve or correct the following observed second-order coupling coefficient features; $2^{1/2} f_B$ hydrodynamic peak, $2^{3/4} f_B$ EM peak, and exponential gain with higher Doppler frequency.

——————————-

Previous researchers have also encountered significant, sometimes limiting, H$_s$ error due to RFI noise. Wyatt and Green [2002] reported significant decrease in spatial and temporal coverage due to RFI. Despite highly directional RFI, the SNR was reduced in all directions. Wyatt et al. [2006] concluded the OSCR radar data had insufficient quality for wave measurements, due to low SNR and antenna sidelobes.

RFI noise creates spurious signals due to its additive effect. These signals can either deform or completely mask the desired ocean signal. Previous researchers have noted the difficulty in recovering usable first or second order ocean signal in the presence of RFI noise [Gurgel et al., 2006, Gurgel and Barbin, 2008]. Accuracy, range, and temporal coverage are all reduced.

The assumption of Rayleigh distributed noise compared well with observations. Fitting a Rayleigh distribution to the ordered spectral energies is shown to perform significantly better at estimating the mean noise value than a simple mean over a smaller range of frequencies. The Rayleigh regression resulted in percent errors of 0.01%. Although, this level of accuracy for the noise estimate is unwarranted, as the noise amplitude does not enter into the equations for ocean parameters. Rather, it is used as a quality control parameter, and in this context high accuracy is not needed. Ordered statistics is most useful when the Doppler spectra is a combination of white noise and relatively greater narrow band sources, e.g. RFI, power supply, or ship echoes. The ordered statistics method is capable of separating the two sources using the energy distribution.

Inspection of the noise level estimates yielded a background noise level of ~ -80 dB, with peak values of ~ -45 dB. The primary contribution to the noise field was external interference.

Both stations identified the strongest source at a heading of 201°, with similar amplitude sources from other headings. A simple mathematical model $N = N_I(r) + N_E(\theta, t)$ described the noise as a function of range, angle, and time. The constant range-decay term $N_I(r)$ was relatively insignificant compared to the directional external interferences $N_E(\theta, t)$. These external interferences had a strong diurnal cycling attributed to greater human activity during daylight hours and sun-driven ionospheric cycles.

Spectral, i.e. frequency, averaging was evaluated for improving H_s estimates without success. Because S1 and S2 vary with direction, spectral averaging should only be done for $\theta \simeq$ constant. The effect of averaging spectra with varying SNR was shown to bias the H_s estimate high due to the integration of noise energy in S2. Thus spectra should only be averaged over a narrow angle and range.

Neither eigen-decomposition or a simple model based approach were successful in reducing the RFI. Eigen-decomposition was not capable of representing the RFI in a few energetic modes. Furthermore, the RFI and ocean signal were not separated in eigenspace, preventing removal of specific modes. A plausible explanation is that the ocean scatter does not have a coherent signal across either antenna or range. Thus it randomly maps into the coherent modes of RFI. For eigen-decomposition to work, the the majority of the RFI energy must map into only a few independent eigenmodes. It is questionable if the assumption of orthogonality is appropriate for representing RFI signals.

The model based approach of estimating the RFI sinusoids showed some promise. The RFI energy was entirely rejected in a narrow range band. Rejection of RFI energy for all ranges was not possible due to errors in estimating the RFI phase. The assumption of a constant RFI frequency in the model is the most likely explanation. Clearly, most anthropogenic signals will have frequency modulation on a scale similar to the FMCW modulation. Additional phase models would be worth pursuing. A fundamental problem with the model-based method is it introduces erroneous energy if the RFI phase is not accurately estimated.

There are alternative solutions for reducing RFI not examined in this thesis. One proactive method is to dynamically choose an unused HF bandwidth to operate the radar. Gurgel and Barbin [2008] discusses adaptive bandwidth allocation with ambient monitoring. In some situations, quiet channels may not be found. Linear prediction filtering may be used to remove the impulse noise of RFI from the time domain [Ponsford et al., 2003]. Linear prediction requires a relatively large ratio of clean, i.e. RFI-free, samples to work. The RFI observed in this thesis was the dominant feature in both the time and frequency domain. Adaptive beamforming is another well-developed method

for canceling point-sourced RFI [Molnar et al., 1990], wherein noise sources are minimized via the principle of interference and carefully chosen filters.

Chapter 5

Conclusion

With proper calibration and data processing, oceanographic radar is capable of providing wide-area measurements that are difficult or impossible to make any other way. The theory and operation of oceanographic radars has been discussed and evaluated. Much of the analysis in this thesis has focused on errors and uncertainties in the radar-derived H_s measurement. All measurements, *in-situ* or remotely-sensed, have uncertainties and associated error due to the relationship between physical process and sensor. In the case of second-order EM scattering from the sea surface, the theoretical relationship is fairly well understood. Because the interaction mechanism is second-order, direct unambiguous measurement of a specific ocean wavelength is not possible.[1] Rather, integrated properties such as H_s, mean period, and mean direction are estimated.

The first and second order EM-ocean interaction mechanisms are separated by how the information content is encoded in the radar signal. First order scattering carries ocean surface velocity information in the Doppler frequency, and is a relatively robust measurement. The Bragg peak occupies a narrow frequency bandwidth and is consequently less likely to share noise frequencies. Conversely, second order scattering is an amplitude based measurement over a comparatively large frequency bandwidth, making it far more susceptible to external interference. Accuracy of the H_s estimate was shown to be dependent on a sufficiently high signal-to-noise ratio. Insufficient SNR results in biasing of the S2 energy by the mean noise level. The effect of the bias depends on the noise conditions. For a quiescent noise environment, i.e. primarily thermal noise, the H_s estimate is biased low. For RFI-dominated conditions, the H_s estimate is biased high with excessive variation.

In this thesis and much of the literature, the removal of RFI from data is a difficult task which may not be fully possible. To this end, two suggestions are made. Reduce the amount of RFI by monitoring the radio frequency environment and selecting unoccupied bandwidths, e.g. Gurgel

---

[1] Caveats to this statement are the $2^{1/2} f_B$ and $2^{3/4} f_B$ singularities.

and Barbin [2008]. Increase the amplitude of the desired ocean signal relative to any noise sources. Forgoing a discussion of logistical and legal difficulties, this is achieved by increasing the transmit power. Ongoing development of a bistatic ocean radar would allow for a substantial increase in transmit power over the current monostatic configuration.

Analysis of the spatial variation of H_s across the measurement domain is dependent on a minimal level of accuracy which was not obtained in this study. The primary cause for error was identified as externally sourced radio frequency interference which limited the radar performance in space and time. Further analysis of physical processes, e.g. land shadowing and current refraction of waves, was not warranted because RFI noise dominated the measurement variation. Efforts to statistically diminish or extract the noise were unsuccessful. Despite the strong RFI noise, the spatially-averaged H_s timeseries was highly correlated to the reference buoy.

Appendix A

Electromagnetic Scattering Derivations

This appendix is intended as a convenient summary and reference to Barrick's derivations of electromagnetic scattering from the ocean surface. The reader is referred to the original publications for completeness [Barrick, 1970, 1971a,b, 1972, Derr, 1972, Weber and Barrick, 1977, Barrick and Weber, 1977].

A.1   Ground Wave Propagation

Barrick [1970] investigated the attenuation of a vertically polarized EM ground-wave due to sea surface roughness. The sea surface roughness causes a scattered EM field, which Barrick [1970] represents as a summation of modes in the total EM field. The strength of the scattered EM modes are directly proportional to the ocean wave modes. The equations result in both propagating and evanescent modes, separated by the Bragg wavelength of the scatterers. Only ocean waves longer than the Bragg wavelength contribute to the resistive portion (Figure A.1). These longer waves are responsible for the removal of energy from the guided waves and scatter into all directions in the upper hemisphere [Barrick, 1970]. Oceans waves of less than the Bragg wavelength result in inductive reactance, and do not scatter the EM wave. Rather, they produce a perturbation on the local field at the surface that does not propagate, and exists only near the region between the waves, i.e. evanescent [Barrick, 1970].

Barrick [1970, 1971b] numerically investigated the attenuation of an EM ground-wave as a function of sea state, transmit frequency and antenna height above the sea surface using a standard ESSA Fortran ground-wave program. Semi-empirical wind-wave models were used as inputs (Neumann-Pierson and [Phillips, 1958]). Attenuation increased with sea state, higher EM frequencies, and longer ranges [Barrick, 1971b]. Attenuation due to sea state was small compared to background loss, i.e. for a smooth sea. For example, the attenuation due to a smooth sea was
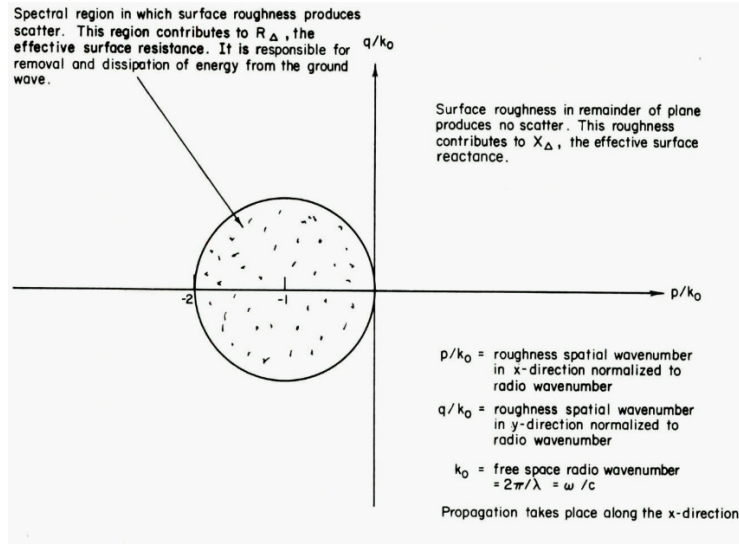
Figure A.1: from Barrick [1970]. Effect of various regions of spatial roughness spectrum on effective surface impedance.

approximately 100 dB at 100 km for a 15 MHz radar (Figure A.2), whereas additional attenuation due to sea state was 5 dB. Attenuation due to normal sea state variations was found to be negligible below about 2 MHz but produced a maximum loss at about 10 to 15 MHz* [Barrick, 1971b]. Sea state becomes less important above 15 MHz, because the seawater impedance increases with frequency [Barrick, 1971b]. Barrick [1970, 1971b] notes that all his calculations were for Tx and Rx near the surface. Cliff deployments might fit the transmission loss curve provided the first range cell is discarded. Table/figures for vertical Tx and Rx offsets, e.g. cliff deployments, are given.

The sea surface is represented as:

$$\zeta(x,y) = \sum_{m,n=-\infty}^{\infty} P(m,n)e^{ia(mx+ny)} \tag{A.1.1}$$

where $a = 2\pi/L$, L is defined as the spatial period of the surface and of the Fourier expansion. $P(m,n)$ is the coefficient of the m,nth Fourier component, with P being zero for $m = n = 0$.

Barrick [1970, 1971a] accounts for the increased attenuation due to sea state using an effective surface impedance:

$$\overline{\Delta} \equiv \Delta + A_{00} \tag{A.1.2}$$

If the surface height is a random variable, the average effective surface impedance becomes:

97
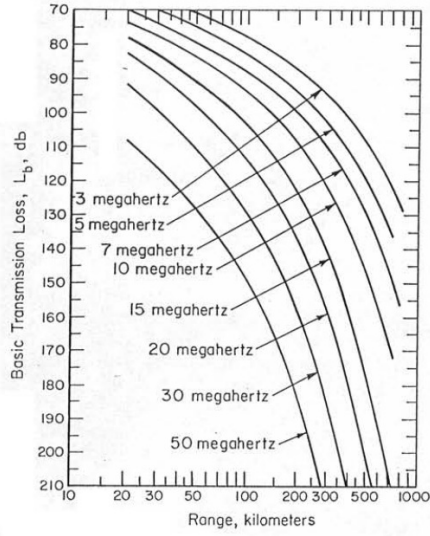
Figure A.2: from Barrick [1971b]. Basic transmission loss across the ocean between points at the surface of smooth spherical Earth. Conductivity is 4 mhos/m and an effective Earth radius factor of 4/3 is assumed.

$$\overline{\Delta} \equiv \langle \Delta + A_{00} \rangle = \Delta + \langle A_{00} \rangle \tag{A.1.3}$$

Following a standard perturbation approach, the solution for $\langle A_{00} \rangle$ to second order is given in Barrick [1970, 1971a, Eq.11,Eq.24]:

$$\overline{\Delta} = \Delta + \frac{1}{4} \int_{-\infty}^{\infty} \int_{-\infty}^{\infty} F(p,q)W(p,q)dpdq \tag{A.1.4}$$

where

$$F(p,q) = \frac{p^2 + b'\Delta(p^2 + q^2 - k_0p)}{b' + \Delta(b'^2 + 1)} + \Delta(\frac{p^2 - q^2}{2} + k_0p)b' = \frac{1}{k_0}\sqrt{k_0^2 - (p + k_0)^2 - q^2} \tag{A.1.5}$$

where $W(p,q)$ is the ocean wave spectrum.

A.2 Ground Wave Scatter

The random sea surface is represented as a Fourier series in space and time, and first-order expressions are derived for the received Doppler spectrum. The scattered EM field is represented

as a Fourier series, with the solution coefficients representing modes of the scattered field. The previous section (Ground Wave Propagation) discussed how the scattered modes can be propagating or non-propagating (Figure A.1). Barrick [1970, 1972] emphasizes the importance of the EM field coefficients: "The direction of propagation of the scattered mode is directly related to the Fourier component of the surface, and for propagation modes, this direction is the Bragg direction required by a periodic surface with wavenumbers am and an."

Barrick [1970, 1972] derived the scattered EM field using a perturbation method [Kline, 1951] and boundary conditions at the surface. Necessary assumptions for the perturbation method include; 1) the sea surface height, ζ, above a mean plane is small in terms of the EM wavelength; and 2) the sea surface slope, $\nabla\zeta$, is small for these longer ocean waves. The Leontovich impedance boundary condition requires 3) the ocean-water medium is highly conducting. For HF, condition 1) is met by ocean waves, and condition 3) is met by seawater [Barrick, 1970, 1972]. Condition 2) becomes an operational limitation and is discussed in §2.2. Limits on the mathematical validity of the solution are given in terms of frequency and sea state [Barrick, 1972, pg.7].

The following derivations are taken directly from [Barrick, 1970]. They illustrate how the received Doppler spectrum is derived from electromagnetic and hydrodynamic first-principles.

The sea surface height is expressed as a Fourier expansion in space and time:

$$\zeta(x,y,t) = \sum_{m,n,l=-\infty}^{\infty} P(m,n,l)e^{ia(mx+ny)-iwlt} \tag{A.2.1}$$

where $a = 2\pi/L$, $w = 2\pi/T$, L and T are defined as the spatial and temporal periods of the surface and of the Fourier expansion. $P(m,n)$ is the coefficient of the m,nth Fourier component, with P being zero for $m = n = 0$.

Following Kline [1951] define an average spatial-temporal spectrum $W(p,q,\omega)$ of the surface height in terms of the Fourier coefficients as

$$W(p,q,\omega) = \frac{1}{\pi^3} \iiint_{-\infty}^{\infty} \langle \zeta(x_1,y_1,t_1)\zeta(x_2,y_2,t_2)\rangle e^{ip\tau_x+iq\tau_y-i\omega\tau} d\tau_x d\tau_y d\tau =$$
$$\frac{L^2 T}{\pi^3} \langle P(m,n,l)P(-m,-n,-l)\rangle \quad \text{(A.2.2)}$$

where $\langle P(m_1,n_1,l_1)P(m_2,n_2,l_2)\rangle$ is zero when $m_2 \neq -m_1$, $n_2 \neq -n_1$, and $l_2 \neq -l_1$ because the Fourier coefficients are uncorrelated. Also, $p = am$, $q = an$, $\omega = wl$, $\tau_x = x_2 - x_1$, $\tau_y = y_2 - y_1$, and $\tau = t_2 - t_1$. The angular braces denote a statistical ensemble average. Also, $\langle P(m,n,l)\rangle = 0$ for all m,n,l.

The perturbed electric fields arising from a vertically polarized wave at grazing incidence passing over the surface are represented as:

$$E_x = \Delta E(h, 0, z, l) + \sum_{m,n,l=-\infty}^{\infty} A_{mnl} E(m+h, n, z, l) \tag{A.2.3}$$

$$E_y = \sum_{m,n,l=-\infty}^{\infty} B_{mnl} E(m+h, n, z, l) \tag{A.2.4}$$

$$E_z = E(h, 0, z, l) + \sum_{m,n,l=-\infty}^{\infty} C_{mnl} E(m+h, n, z, l) \tag{A.2.5}$$

$$E(m+h, n, z, l) = E_0 e^{i(a(m+h)x + any + b(m+h,n)z + (wl - \omega_0)t)} \tag{A.2.6}$$

$$b(m+h, n) = \sqrt{k_0^2 - a^2(m+h)^2 - a^2 n^2} \tag{A.2.7}$$

where $h = k_0 \sin\theta_i / a$. The definition of b above is such that A.2.3 satisfy the Helmholtz wave equation. The magnetic fields H are not given, but are determined from Maxwell's equations. From A.2.3, the electric field E is complex in general so it has a magnitude and a phase. Δ is the normalized surface impedance at grazing for a medium below the smooth interface of complex permittivity ϵ_1 and permeability μ_1

$$\Delta = \frac{1}{120\pi} \sqrt{\frac{\mu_1}{\epsilon_1}} \times \sqrt{1 - \frac{\epsilon_0 \mu_0}{\epsilon_1 \mu_1}} \simeq \frac{1}{120\pi} \sqrt{\frac{\mu_1}{\epsilon_1}} \text{ for } \epsilon_1 \gg \epsilon_0 \tag{A.2.8}$$

Included in ϵ_1 is the effect of conductivity, i.e. $\epsilon_1 = \epsilon_{r1} + i\sigma_1/\omega_0$, where ϵ_{r1} is the real dielectric constant of the medium and σ_1 is it conductivity. For sea water at 10 MHz, for example, $\epsilon_{r1} \simeq 80\epsilon_0$, $\sigma_1 \simeq 4$ mhos/m, $\epsilon_1 \simeq \epsilon_0(80 + i7200)$, and $\Delta \simeq 1.18 \cdot 10^{-2} \exp -i\pi/4$.

The solution of the problem consists of finding $A_{mnl}, B_{mnl}, C_{mnl}$. This is done using the Kline [1951] perturbation expansion with Leontovich boundary conditions at the surface. Only first order terms are retained. The solution for the coefficients is:

$$A_{mnl} = \frac{N_A}{D(m,n)} P(m, n, l) \tag{A.2.9}$$

$$B_{mnl} = \frac{N_B}{D(m,n)} P(m, n, l) \tag{A.2.10}$$

$$C_{mnl} = \frac{-a[(m+h)N_A - nN_B]}{b(m+h,n)D(m,n)} P(m, n, l) \tag{A.2.11}$$

where

$$N_A = -iam[1 + \frac{\Delta k_0}{b}(1 - \frac{a^2(m+h)^2}{k_0^2})] + ian\frac{\Delta k_0}{b}\frac{a^2n(m+h)}{k_0^2} \qquad (A.2.12)$$

$$N_B = -ian[1 + \frac{\Delta k_0}{b}(1 - \frac{a^2n^2}{k_0^2})] + iam\frac{\Delta k_0}{b}\frac{a^2n(m+h)}{k_0^2} \qquad (A.2.13)$$

$$D(m,n) \simeq 1 + \frac{\Delta k_0}{b(m+h,n)}(1 + \frac{b^2(m+h,n)}{k_0^2}) \qquad (A.2.14)$$

Again: the first-order coefficients of the scattered EM mode are directly related to the Fourier coefficients of the surface mode, e.g. $A_{mnl} = \frac{N_A}{D(m,n)}P(m,n,l)$. The direction of propagation for the EM mode being the same as the Bragg wavenumber of the surface m,n mode, i.e. $\hat{k}_B = 1/2(m\hat{x} + n\hat{y})$.

A.3 Far Field Scatter

Thus far, Barrick [1970] has derived modal, plane-wave expansions A.2.3,A.2.9 for the scattered EM fields above a surface of infinite extent, given the Fourier expansion of the surface. Barrick [1970] proceeds to derive an expression for the received EM field at a distant antenna. The analysis begins with a previously derived [Ruck et al., 1970] expression for the scattered *magnetic* far-field A.3.1, which is a function of the electric and magnetic fields at a point (Figure ref-fig:barrick:1970:3). This vector integral is obtained using the vector analog of Green's Theorem on Maxwell's equation [Ruck et al., 1970]. It is often called the Chu-Stratton integral, and under simplifying assumptions, the physical optics integral. Thus the EM far-field is derived from electromagnetic first principles.

Consider a patch of sea surface dS of finite extent. Choose a square patch of side L, with the condition that L is much larger than the wavelength λ but much smaller than R_0 the distance from the patch to the observation point, i.e. $\lambda \ll L \ll R_0$. When the scattering patch is considerably smaller in extent than R_0 (Figure 1.8), we can employ the following equation for the scattered *magnetic* field [Ruck et al., 1970]:

$$\boldsymbol{H}^s(R_0, t) \simeq$$
$$\frac{ik_0e^{ik_0R_0}}{4\pi R_0}\int_{-L/2}^{L/2}\int_{-L/2}^{L/2}[\hat{k}_0^s \times (\hat{z} \times \boldsymbol{H}^s) - \sqrt{\frac{\epsilon_0}{\mu_0}}(\hat{z} \times \boldsymbol{E}^s) + \sqrt{\frac{\epsilon_0}{\mu_0}}\hat{k}_0^s \cdot (\hat{z} \times \boldsymbol{E}^s)\hat{k}_0^s]e^{-ik_0\hat{k}_0^s \cdot \boldsymbol{r}'}dxdy$$

$$(A.3.1)$$

where $\boldsymbol{E}^s$ and $\boldsymbol{H}^s$ in the integrand are the fields evaluated at the surface element $dxdy$ on the $z = 0$ plane. $\boldsymbol{H}^s$ is determined from $\boldsymbol{E}^s$ using Maxwell's equations. The vector $\boldsymbol{r}'$ points from the origin to the local area increment, $dxdy$, on the surface of integration, i.e. $\boldsymbol{r}' = x\hat{x} + y\hat{y} + z\hat{z}$. $\hat{k}_0^s$ is a unit vector pointing in the desired observation direction, i.e. $\hat{k}_0^s = \sin\theta_s \cos\phi_s \hat{x} + \sin\theta_s \sin\phi_s \hat{y} + \cos\theta_s \hat{z}$ (Figure 1.8).

For the scattered H-field normal to the scatter plane, i.e. the $\hat{\varphi}_s$ component of $\boldsymbol{H}^s(R_0, t)$, the integral becomes:

$$H_\varphi^s(R_0, t) = \frac{ik_0 e^{ik_o R_0}}{4\pi R_0} \sum_{m,n,l} \int_{-L/2}^{L/2} \int_{-L/2}^{L/2} f_\varphi(m, n) P(m, n, l)$$
$$e^{i(a(m+h)x + any + (wl - \omega_0)t)} e^{-ik_0(\sin\theta_s \cos\varphi_s x + \sin\theta_s \sin\varphi_s y)} dxdy \quad \text{(A.3.2)}$$

where $f_\varphi(m, n)$ is a factor containing N_A, N_B, and $\hat{k}_0^s$, determined from A.3.1.

A.3.2 can be integrated over the square patch to give:

$$H_\varphi^s(R_0, t) = \frac{ik_0 e^{ik_0 R_0}}{\pi R_0} \sum_{m,n,l} f_\varphi(m, n) P(m, n, l)$$
$$\left[\frac{\sin\frac{L}{2}(a(m+h) - k_0 \sin\theta_s \cos\varphi_s)}{a(m+h) - k_0 \sin\theta_s \cos\varphi_s}\right] \left[\frac{\sin\frac{L}{2}(an - k_0 \sin\theta_s \sin\varphi_s)}{an - k_0 \sin\theta_s \sin\varphi_s}\right] e^{i(wl - \omega_0)t} \quad \text{(A.3.3)}$$

Barrick then proceeds to show how the effective surface impedance $\overline{\Delta}$ is accounted for Barrick [1970, see §3.3]. In short, the solution is found by evaluating the scattering equation for zero impedance $\Delta = 0$, and multiplying by the Norton attenuation factor $2F'$. The only factor affected by this step is f_φ.

A.4 Average Scattered Signal Spectrum

At this point, we are ready to consider averaging over ensembles of surfaces whose Fourier expansion coefficients $P(m, n, l)$ are random variables. To this end, form $H_\phi^s(R_0, t_1)H_\phi^s *(R_0, t_2)$ from A.3.3 and average to obtain $R^s(\tau)$, where $\tau = t_1 - t_2$. This implies stationarity in the temporal sense so that $R^s(\tau)$ depends only on the difference, τ, and not upon t_1 or t_2.

$$R^s(\tau) = \frac{k_0^2 L^4 F'^2}{32\pi^2 R_0^2} \int \int \int_{-\infty}^{\infty} |f_\varphi^c(p,q)|^2$$

$$\left[\frac{\sin \frac{L}{2}(k_0 \sin \theta_s \cos \varphi_s - k_0 - p)}{\frac{L}{2}(k_0 \sin \theta_s \cos \varphi_s - k_0 - p)} \right]^2 \left[\frac{\sin \frac{L}{2}(k_0 \sin \theta_s \sin \varphi_s - k_0 - q)}{\frac{L}{2}(k_0 \sin \theta_s \sin \varphi_s - k_0 - q)} \right]^2 W(p,q,\omega) e^{i(\omega-\omega_0)\tau} dp\,dq\,d\omega$$

<div align="right">(A.4.1)</div>

where f_φ^c is f_φ evaluated at $\Delta \to 0$. The six summations have been reduced to the triple integral by using the statistical independence of the Fourier coefficients and the definition of the spatial and temporal surface height spectrum A.2.2. Since all quantities in the integrand now apply to a perfectly conducting surface, ah becomes k_0 Barrick [1970].

Equation A.4.1 is simplified by employing the previous assumption that the scattering patch size L is much greater than the wavelength, so that $k_0 L >> 1$. Under these conditions, the $[\sin x/x]^2$ functions in the integrand become impulse functions:

$$L \left[\frac{\sin \frac{L}{2}(k_0 \sin \theta_s \cos \varphi_s - k_0 - p)}{\frac{L}{2}(k_0 \sin \theta_s \cos \varphi_s - k_0 - p)} \right]^2 \Rightarrow 2\pi\delta[p - k_0(\sin \theta_s \cos \varphi_s - 1)] \quad\quad \text{(A.4.2)}$$

This simplification is key, because the impulse function reduces the integral over all wavenumbers to only those satisfying the Bragg wavelength. These impulse functions permit integration of A.4.1 over p and q to give

$$R^s(\tau) = \frac{k_0^2 L^2 F'^2}{8R_0^2} \left[f_\varphi^c(k_0(\sin \theta_s \cos \varphi_s - 1), k_0 \sin \theta_s \sin \varphi_s) \right]^2$$

$$\int_{-\infty}^{\infty} W(k_0(\sin \theta_a \cos \varphi_s - 1), k_0 \sin \theta_s \sin \varphi_s, \omega) e^{i(\omega-\omega_0)\tau} d\omega \quad \text{(A.4.3)}$$

The power density spectrum of the scattered signal is the Fourier transform of the correlation function:

$$P^s(\omega) = \frac{1}{\pi} \int_{-\infty}^{\infty} R^s(\tau) e^{-i\omega\tau} d\tau$$

$$= \frac{k_0^2 L^2 F'^2}{4R_0^2} \left[f_\varphi^c(k_0(\sin \theta_s \cos \varphi_s - 1), k_0 \sin \theta_s \sin \varphi_s) \right]^2$$

$$W(k_0(\sin \theta_s \cos \varphi_s - 1), k_0 \sin \theta_s \sin \varphi_s, \omega - \omega_0) \quad \text{(A.4.4)}$$

Now simplify f_φ^c by noting that as $\Delta \to 0, N_A \to -ip = -ik_0(sin\theta_s \cos\varphi_s - 1), N_B \to -iq = -ik_0 \sin\theta_s \sin\varphi_s$, and $D(m,n) \to 1$.

$$P^s(\omega) = \frac{k_0^4 L^2 F'^2 H_0^2}{4R_0^2}(sin\theta_s - \cos\varphi_s)^2 W(k_0(\sin\theta_s \cos\varphi_s - 1), k_0 \sin\theta_s \sin\varphi_s, \omega - \omega_0) \quad \text{(A.4.5)}$$

where $H_0 = \frac{k_0}{\omega_0\mu_0}E_0$. Convert to $\sigma(\omega)$, the range-independent bistatic scattering cross section per unit surface area per radian s^{-1} bandwidth by multiplying by $4\pi R^2/L^2 H_0^2 F'^2$ to obtain:

$$\sigma(\omega) = \pi k_0^4(\sin\theta_s - \cos\varphi_s)^2 W(k_0(\sin\theta_s \cos\varphi_s - 1), k_0 \sin\theta_s \sin\varphi_s, \omega - \omega_0) \quad \text{(A.4.6)}$$

Integrate over all frequencies to obtain the average bistatic scattering cross section per unit area:

$$\sigma^0 = \pi k_0^4(\sin\theta_s - \cos\varphi_s)^2 W(k_0(\sin\theta_s \cos\varphi_s - 1), k_0 \sin\theta_s \sin\varphi_s) \quad \text{(A.4.7)}$$

Both spectra have the wavenumbers p, q replaced by $k_0(\sin\theta_s \cos\phi_s - \sin\theta_i), k_0 \sin\theta_s \sin\phi_s$. The latter are precisely the wavenumbers required of a diffraction grating which is to scatter a wave incident from θ_i into directions θ_s, ϕ_s.

A.5   First Order Spectrum

This section applies the gravity wave dispersion relation to simplify 1.4.2 and yield the final first order relationship between the ocean wave directional spectrum and Doppler spectrum 1.4.5. The derivation is from Barrick [1970, 1972].

The first-order surface gravity wave dispersion relation makes it possible to relate the spatial-temporal height spectrum $W(p, q, \omega)$ to the simpler spatial spectrum $W(p, q)$.

$$\omega_{g\pm}^2 = \pm g\sqrt{p^2 + q^2} = \pm g\sqrt{(am)^2 + (an)^2} \quad \text{(A.5.1)}$$

Therefore, A.2.1 is rewritten as follows:

$$\zeta(x, y, t) = \sum_{m,n=-\infty}^{\infty} P_\pm(m, n)e^{i(amx + any + \omega_{g\pm})} \quad \text{(A.5.2)}$$

The spatial-temporal spectrum then becomes:

104

$$W(p, q, \omega) = 2W_+(p, q)\delta(\omega + \omega_+) + 2W_-(p, q)\delta(\omega + \omega_-) \qquad \text{(A.5.3)}$$

where $W_\pm(p, q) = \langle |P_\pm(m, n)|^2 \rangle L^2/\pi^2$, the $\pm$ signs refer to the direction of motion of the waves, and $\omega_\pm$ is given in 1.4.3.

The spatial-temporal waveheight spectrum for a given p,q (spatial wavenumbers) consists of only two possible discrete temporal frequencies, ω_+ and ω_-, which are related to p and q through 1.4.3 [Barrick, 1970].

Substituting 1.4.4 into 1.4.2:

$$\sigma(\omega) = 4\pi k_0^4 (\sin\theta_s - \cos\varphi_s)^2 \left[W_+(k_0(\sin\theta_s \cos\varphi_s - 1), k_0 \sin\theta_s \sin\varphi_s)\delta(\omega + \omega_+ - \omega_0) \right.$$
$$\left. + W_-(k_0(\sin\theta_s \cos\varphi_s - 1), k_0 \sin\theta_s \sin\varphi_s)\delta(\omega + \omega_- - \omega_0) \right] \quad \text{(A.5.4)}$$

A.6   Second Order Spectrum

The vertical displacement of the surface due to waves is represented as a spatial and temporal Fourier series:

$$\eta(\boldsymbol{r}, t) = \sum_{\boldsymbol{k}, \omega} \eta(\boldsymbol{k}, \omega) \exp i(\boldsymbol{k} \cdot \boldsymbol{r} - \omega t) \qquad \text{(A.6.1)}$$

where $\boldsymbol{r} = x\hat{x} + y\hat{y}$ is the position in the x,y plane. The velocity potential is:

$$\Phi(\boldsymbol{r}, z, t) = \sum_{\boldsymbol{k}, \omega} \Phi(\boldsymbol{k}, \omega) \exp kz + i(\boldsymbol{k} \cdot \boldsymbol{r} - \omega t) \qquad \text{(A.6.2)}$$

The fact that $\eta(\boldsymbol{r}, t)$ and $\Phi(\boldsymbol{r}, z, t)$ are real physical quantities requires $\eta^*(\boldsymbol{k}, \omega) = \eta(-\boldsymbol{k}, -\omega)$ and $\Phi^*(\boldsymbol{k}, \omega) = \Phi(-\boldsymbol{k}, -\omega)$. The Fourier coefficients for waveheight $\eta(\boldsymbol{k}, \omega)$, velocity potential $\Phi(\boldsymbol{k}, \omega)$ and frequency ω are expanded in perturbation series as follows:

$$\eta(\boldsymbol{k}, \omega) = \eta_1(\boldsymbol{k}, \omega) + \eta_2(\boldsymbol{k}, \omega) + ..., \qquad \text{(A.6.3)}$$
$$\Phi(\boldsymbol{k}, \omega) = \Phi_1(\boldsymbol{k}, \omega) + \Phi_2(\boldsymbol{k}, \omega) + ..., \qquad \text{(A.6.4)}$$
$$\omega = \omega_0 + \omega_1 + \omega_2 + ..., \qquad \text{(A.6.5)}$$

First order terms are equated to yield:

$$\omega_0^2 - gk \tag{A.6.6}$$

At this point, the notation $\boldsymbol{K}, \Omega$ is used for second order waves to indicate their exclusion from the first order dispersion relation A.6.6. The spatial wavenumber of the second order wave $\boldsymbol{K}$ is the vector sum of the wavenumbers of the first order waves present. The same is true for the frequencies.

$$\boldsymbol{K} = \boldsymbol{k} + \boldsymbol{k}' \text{ and } \Omega_0 = \omega_0 + \omega_0' \tag{A.6.7}$$

(to lowest order, where $\omega_0 = \sqrt{gk}$ and $\omega_0' = \sqrt{gk'}$). The second-order waveheight:

$$\eta_2(\boldsymbol{K}, \Omega) = \sum_{\boldsymbol{k}, \omega} \sum_{\boldsymbol{k}', \omega'} A(\boldsymbol{k}, \omega, \boldsymbol{k}', \omega') \eta_1(\boldsymbol{k}, \omega) \eta_1(\boldsymbol{k}', \omega') \times \delta_{\boldsymbol{K}}^{\boldsymbol{k} + \boldsymbol{k}'} \delta_{\Omega}^{\omega + \omega'} \tag{A.6.8}$$

where the expression has been written in a symmetrical form with the help of the Kronecker delta functions, and where

$$A(\boldsymbol{k}, \omega, \boldsymbol{k}', \omega) = \begin{cases} \frac{1}{2}[k + k' + \frac{\omega_0 \omega_0'}{g}(1 - \hat{k} \cdot \hat{k}')(\frac{gK + \Omega_0^2}{gK - \Omega_0^2})] \\ 0 \text{ if } \boldsymbol{k}' = -\boldsymbol{k} \text{ and } \omega' = -\omega \end{cases} \tag{A.6.9}$$

$\boldsymbol{k}$ and $\eta_1(\boldsymbol{k}, \omega$ are taken as the independent variables of the problem, and all other quantities are dependent upon these variables. Thus, to lowest order $\omega \approx \omega_0$ as derived in A.6.6, and is seen to be a function of $k \equiv |\boldsymbol{k}|$. Therefore, η_1 is actually only a function of $\boldsymbol{k}$. The Kronecker deltas can be removed from A.6.9, since they essentially express that frequency terms in the summations are not independent variables, (functions of k), so the sums can be over $\boldsymbol{k}$ only.

The solution is then carried to third order to solve for the first nonzero correction to the lowest order dispersion relation A.6.6. $\omega = \omega_0 + \omega_2$. ($\omega_1 = 0$)

$$\omega_2 = \omega_0 \sum_{\boldsymbol{k}', \omega'} C(\boldsymbol{K}, \omega, \boldsymbol{k}', \omega') |\eta_1(\boldsymbol{k}', \omega')|^2 \tag{A.6.10}$$

where

$$C(\boldsymbol{k}, \omega, \boldsymbol{k}', \omega') = \frac{1}{2}\left[k'^2 + \frac{\omega_0'}{\omega_0}\boldsymbol{k} \cdot \boldsymbol{k}'(2 + \frac{k}{k'})\right](1 - \frac{1}{2}\delta_{\omega'}^{\omega}\delta_{\boldsymbol{k}'}^{\boldsymbol{k}} - \frac{1}{2}\delta_{\omega'}^{-\omega}\delta_{\boldsymbol{k}'}^{-\boldsymbol{k}})$$
$$+ A(\boldsymbol{k}, \omega, \boldsymbol{k}', \omega')\left[-k' + \frac{\omega_0'}{\omega_0}\frac{\boldsymbol{k} \cdot \boldsymbol{k}'}{k'}\right] - \frac{B(\boldsymbol{k}, \omega, \boldsymbol{k}', \omega')}{i\omega_0}\left[\boldsymbol{k} \cdot (\boldsymbol{k} + \boldsymbol{k}') - k|\boldsymbol{k} + \boldsymbol{k}'| + \frac{\omega_0' k}{\omega k'}\boldsymbol{k}' \cdot (\boldsymbol{k} + \boldsymbol{k}')\right]$$
$$\tag{A.6.11}$$

where

$$B(\boldsymbol{k}, \omega, \boldsymbol{k}', \omega') = \frac{-i\Omega_0 \omega_0 \omega_0' (1 - \hat{k} \cdot \hat{k}')}{gK - \Omega_0^2} \tag{A.6.12}$$

The gravity wave dispersion relation can be expressed (to second order):

$$\omega(\boldsymbol{k}) = \omega_0 + \omega_2 = \omega_0(1 + \frac{\omega_2}{\omega_0}) = \sqrt{gk}(1 + \frac{\omega_2}{\omega_0}) \tag{A.6.13}$$

and hence

$$v_{ph} = \sqrt{gk}(1 + \frac{\omega_2}{\omega_0}) = \sqrt{gk}(1 + \Delta v_{ph}(\boldsymbol{k})) \tag{A.6.14}$$

The waveheights $\eta_1(\boldsymbol{k}, \omega)$ are in general complex random variables whose statistics change over areas and times larger that those required for energy transfer [Weber and Barrick, 1977]. The analysis continues by performing statistical averaging of the Fourier series solutions; yielding average waveheight spectra.

Using statistical assumptions, the surface waveheight spectrum is defined in terms of the height coefficients (for each order) as:

$$\langle \eta_n(\boldsymbol{k}, \omega) \eta_n^*(\boldsymbol{k}', \omega') \rangle = \begin{cases} \frac{(2\pi)^3}{L_x L_y T} S_n(\boldsymbol{k}, \omega) & \text{for } \boldsymbol{k}' = \boldsymbol{k} \text{ and } \omega' = \omega \\ 0 & \text{for other } \boldsymbol{k}', \omega' \end{cases} \tag{A.6.15}$$

where $\langle f \rangle$ denotes an ensemble average of f, and $S_n(\boldsymbol{k}, \omega)$ is the nth order directional waveheight spectrum for arbitrary spatial wave vector $\boldsymbol{K}$ and frequency ω. The waveheight coefficients are taken to have zero mean: $\langle \eta_1(\boldsymbol{k}, \omega) \rangle \equiv 0$ for all $\boldsymbol{k}, \omega$.

The waveheight spectra are defined with the following normalization with respect to root-mean-square waveheight h:

$$h^2 = \langle \eta^2(\boldsymbol{r}, t) \rangle = \int_{-\infty}^{\infty} \int_{-\infty}^{\infty} d^2k \int_{-\infty}^{\infty} d\omega S(\boldsymbol{k}, \omega) \tag{A.6.16}$$

The periodic, nonrandom, Fourier series descriptions of waves A.6.8 is converted to integrals representing average spectra. Using A.6.8, an expression for the second order waveheight spectrum $S_2(\boldsymbol{K}, \Omega)$ is derived in terms of the first order waveheight spectra:

$$S_2(\boldsymbol{K}, \Omega) = \frac{1}{2} \int_{-\infty}^{\infty} \int_{-\infty}^{\infty} d^2\boldsymbol{\kappa} \sum_{u,l} \sum_{u,l} A^2(\boldsymbol{k}, \pm\sqrt{gk}, \boldsymbol{k}', \pm\sqrt{gk'}) S_1(\pm\boldsymbol{k}) S_1(\pm\boldsymbol{k}') \delta(\Omega \mp \sqrt{gk} \mp \sqrt{gk'}) \tag{A.6.17}$$

107

$$\sigma_2(\omega_d) = 2^4 \pi k_0^4 \int \int_{-\infty}^{\infty} |\Gamma(\vec{k_1}, \vec{k_2})|^2 S(\vec{k_1}) S(\vec{k_2}) \delta(\omega_d - \omega_1 - \omega_2) d\vec{k} \qquad \text{(A.6.18)}$$

where $\boldsymbol{k} \equiv 1/2\boldsymbol{K} + \boldsymbol{\kappa}$, $\boldsymbol{k'} \equiv 1/2\boldsymbol{K} - \boldsymbol{\kappa}$, and the summation indices refer to the upper and lower signs in the equation. The Dirac-delta function permits evaluation of one integral, leaving the other to be done numerically.

Defining the mean wave frequency in a centroid sense:

$$\overline{\omega} = \frac{\int_0^{\infty} \omega S(\omega) d\omega}{\int_0^{\infty} S(\omega) d\omega} \qquad \text{(A.6.19)}$$

The radar mean wave period τ_0 is [Barrick, 1977]:

$$\frac{\omega_B \tau_0}{2\pi} = \frac{\int_{0,1}^{1,\infty} \sigma_2(\omega_B \nu)/W(\nu) d\nu}{\int_{0,1}^{1,\infty} |\nu - 1| \sigma_2(\omega_B \nu)/W(\nu) d\nu} \qquad \text{(A.6.20)}$$

where the integrations could be over [0,1] or [1,∞].

Appendix B

WERA Significant Waveheight Algorithm

The following is a summary of the WERA method for calculating H$_s$ as described in more detail in Gurgel et al. [2006]. It is based on the assumption of a directional spreading function for ocean waves, combined with a empirical fit of the second order Doppler spectrum to the scalar ocean wave spectrum.

First, the greater first-order Bragg peak is identified, and its associated second-order sidebands are normalized by this Bragg peak. Gurgel et al. [2006] then assumes the measured Doppler spectrum S_k depends on the ocean waveheight spectrum measured by a buoy H_k by

$$\alpha_k S_{mk} = H_k F(\varphi_k - \varphi_r) \tag{B.0.21}$$

$$\alpha_k S_{pk} = H_k F(\varphi_k - \varphi_r + \pi) \tag{B.0.22}$$

where the indices m and p of S refer to negative and positive Doppler shifts *relative* to the first-order Bragg peak, respectively, and $k = 1, ...$ counts the spectral frequencies. F is an angular spreading function, discussed in detail in §1.5.2. φ_k is the mean wave direction measured by a wave buoy, and φ_r is the radar look direction, both counting clockwise from north, i.e. compass coordinates.

Assuming simple directional spreading functions of the form

$$F = cos^2(0.5\varphi) \qquad\qquad \text{with} s = 2 \text{and} s = 4 \tag{B.0.23}$$

The solutions are:
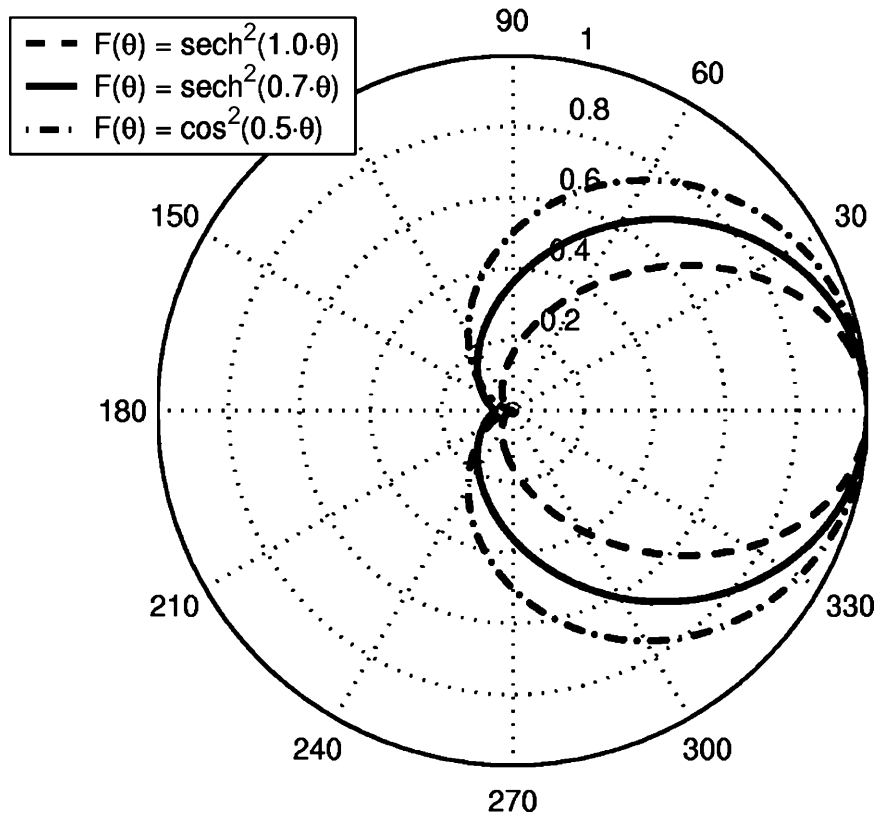
Figure B.1: from Gurgel et al. [2006]. Three different functions to approximate the angular distribution of short scattering ocean waves.

$$H_k = \alpha_k(S_{mk} + S_{pk}) \qquad\qquad \text{for } s = 2 \qquad \text{(B.0.24)}$$

$$H_k = \alpha_k(S_{mk} + S_{pk} + 2\sqrt{S_{mk}S_{pk}} \qquad\qquad \text{for } s = 4 \qquad \text{(B.0.25)}$$

Assuming $s = 2$, the regression coefficients α_k are determined by regressing radar spectra to *in-situ* observations, e.g. directional buoy spectra [Gurgel et al., 2006]. A constant spreading function is used for all wave frequencies.

The single site direction ambiguity is resolved using two sites and minimizing:

$$\left[\gamma_{1k} - \frac{F(\varphi_k - \varphi_1)}{F(\varphi_k - \varphi_1 + \pi)}\right]^2 + \left[\gamma_{2k} - \frac{F(\varphi_k - \varphi_2)}{F(\varphi_k - \varphi_2 + \pi)}\right]^2 \qquad \text{(B.0.26)}$$

$$\Rightarrow \text{minimum at } \gamma_k = \frac{S_{mk}}{S_{pk}} \qquad \text{(B.0.27)}$$

where $r = 1$ and $r = 2$ refer to the two radar sites. The solution does not depend on the regression coefficients α_k.

Gurgel et al. [2006] estimates the direction of the wind sea waves using the following directional spreading model:

$$F(\varphi) = A_s sech^2 \left[0.8(\varphi - \varphi_0)\right] \qquad \text{(B.0.28)}$$

where φ_0 is the mean wave direction, and

$$A_2 = 1/\int_0^{2\pi} sech^2(0.8\varphi)d\varphi \qquad \text{(B.0.29)}$$

is a normalization constant. The directional distribution is intersected at an angle of θ, referring to the energy of the waves running towards and away from the radar. Using the Bragg ratio R_B of Long and Trizna [1973], the quotient

$$\gamma = \frac{sech^2 \left[0.8(\theta + \pi - \varphi_0)\right]}{sech^2 \left[0.8(\theta - \varphi_0)\right]} \qquad \text{(B.0.30)}$$

is evaluated to give the direction φ_0 of the Bragg waves.

The radar wave spectra estimates are the arithmetic mean of both stations. The waveheight is computed by integrating the spectral values, and the mean wave direction is the mean weighted by the spectral amplitudes.

Appendix C

Beamforming

Beamforming is combining multiple omni-directional signals, from receivers separated in space, to yield a single directional signal. The analogy to a beam of energy in a specific direction is quite appropriate, with little difference between transmitted and received energy. To understand beamforming, consider a complex EM wave incident on multiple receiving antennas. The measured signal follows the wave equation:

$$A(x) = e^{i(\boldsymbol{k} \cdot \boldsymbol{x} - \omega t)} \tag{C.0.31}$$

where A is typically measured voltages for each antenna located at vector position $\boldsymbol{x}$. The frequency ω and time t of the measurements are known. The EM wavenumber $k_0 = |\boldsymbol{k}|$ is also known. The unknown is the direction of the EM wavevector $\boldsymbol{k}$. The vector dot product $\boldsymbol{k} \cdot \boldsymbol{x}$ describes the phase rate of the incident wave. Thus the unknown direction of an incident EM wave can be (non-uniquely) determined from the relative phases of the measured signal $A(x)$. Likewise, the measured signals can be beamformed in a desired direction:

$$A_B(\theta) = \sum A(x) e^{i(\boldsymbol{k_B}(\boldsymbol{\theta}) \cdot \boldsymbol{x})} \tag{C.0.32}$$

where $\boldsymbol{k_B}$ is the EM wavevector from the desired incident direction θ and wavenumber k_0. The summation creates an interference between the antenna signals; those in the desired direction will be constructive, other directions will be destructive. Equation C.0.32 is essentially a discrete space Fourier transform.

The effect of beamforming is visualized using a plot of field strength vs. direction referred to as the array pattern (Figure C.1). Common features of array patterns are the large centerlobe,
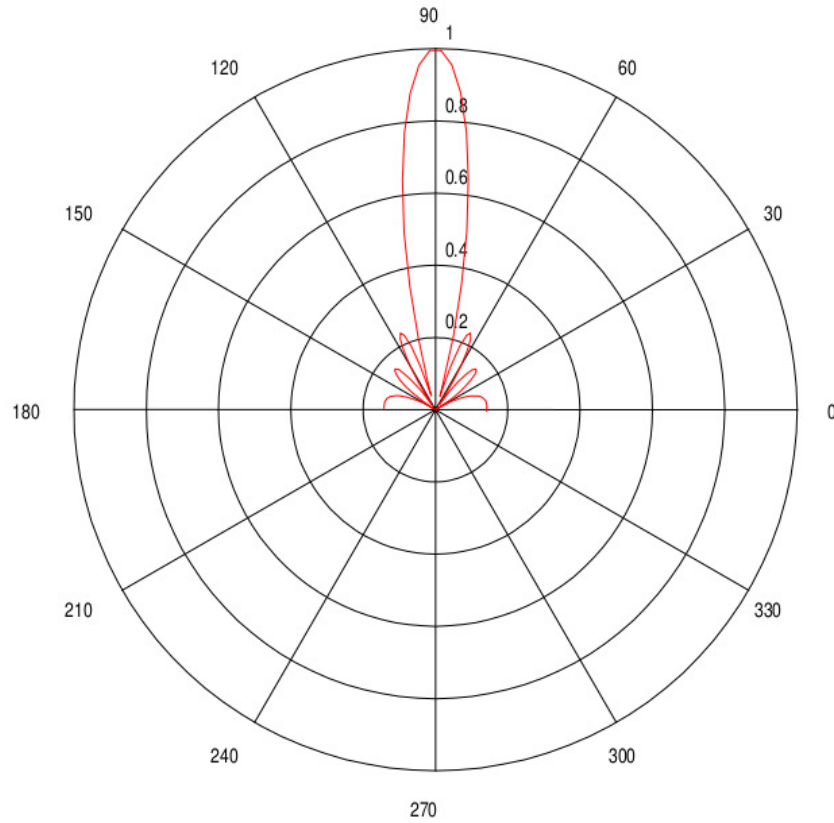
Figure C.1: An example array pattern for a 7 element linear array of total length $L = 3\lambda$. The centerlobe is at $90°$, with 6 smaller sidelobes to the left and right.

smaller amplitude sidelobes, and zero-gain nulls between lobes. Comparative properties of the centerlobe are the halfpower beamwidth and full width at half maximum (FWHM).

Beamforming cannot uniquely determine signal from a specified direction. The phase rate given by $\boldsymbol{k_B}(\boldsymbol{\theta_0}) \cdot \boldsymbol{x}$ may be closely approximated by other directions $\theta_1, \theta_2, ... theta_n$. This spatial frequency aliasing is highly analogous to time-domain spectral aliasing. Improving the number and spacing of antennas can, for all intensive purposes, negate the effects of spatial aliasing. Increasing the total width L decreases the centerbeam width. Increasing the number of antenna elements decreases the sidelobes. If the antenna spacing exceeds $\lambda/2$, the centerbeam width continues to decrease, but the sidelobes become excessively large. At $d \geq \lambda$ more than one centerlobe appears in the pattern. Such second centerbeams are called grating lobes. Thus, the optimal array design is a maximum number of antennas spaced at $\lambda/2$. The angular resolution that can be obtained from an array with a total aperture of L is roughly λ/L radians. With $\lambda/2$ spacing of n antennas, this simplifies to an angular resolution of $2/n$. The array pattern varies with steering angle. As the

radiation pattern is steered broadside to endfire, i.e. orthogonal to parallel with the array, the width of the centerbeam becomes larger.

Applying only phase shifts to each antenna in C.0.32 corresponds to a boxcar filter in the space domain and a sinc function convolution in the spatial frequency domain. Judicious use of windowing functions can improve the array pattern. The sinc function has a FWHM of $1.21 \, \mathrm{df}/2\pi$ with a peak sidelobe of $\simeq 22\%$. The Hanning window gives $2 \, \mathrm{df}/2\pi$ with a peak sidelobe of $\simeq 2.6\%$. Combining an amplitude windowing function with the beamsteering phase shift, i.e. a complex weight, improves control over side lobe levels at the expensive of centerlobe width. The complex array factor $w(\vec{k})$ acts as a transfer function:

$$w_k = a_k e^{i\theta_k} \tag{C.0.33}$$

where w_k are the complex weights for each k antenna element, a_k is the relative amplitude of the weight, and θ_k is the phase shift of the weight. For uniformly spaced arrays, array factor design methods are identical to the methods for designing FIR digital filters in signal processing. As well as controlling the centerlobe width and sidelobe levels, the position of a null can be controlled.

A variety of errors can affect beamforming. It is important that the amplitude and phase response of the antennas is well known and incorporated into the array factor. Antenna ground planes, cables, buried conductors, fences, and ground conductivity all contribute to the array factor. Land path propagation of the EM wave can have a varying response with direction. Much of the array factor error can be corrected by careful calibration of the radar system.

114

Appendix D

Vector Correlation

The following is from a short paper on vector correlation [Hanson et al., 1992].

Consider the correlation between n pairs of two dimensional vectors, represented as complex numbers z_j and w_j. Variance and covariance can be defined as:

$$\sigma_z^2 = \frac{1}{n} \sum_{j=1}^{n} (z_j - \overline{z})^*(z_j - \overline{z}) = \sigma_x^2 + \sigma_y^2 \tag{D.0.34}$$

$$\boldsymbol{\sigma_{zw}} = \frac{1}{n} \sum_{j=1}^{n} (z_j - \overline{z})^*(w_j - \overline{w}) = (\sigma_{xu} + \sigma_{yv}) + i(\sigma_{xv} - \sigma_{yu}) \tag{D.0.35}$$

where * indicates complex conjugate.

The variance of z_j is the sum of the component variances while the covariance is a vector. The real portion $\sigma_{xu} + \sigma_{yv}$ is the sum of the covariances between corresponding components of the variables. The imaginary portion $\sigma_{xv} - \sigma_{yu}$ measures the "twisting" of one vector's components into the opposite components of the other vector. Twisting implies a direction (from one vector into another) so vector covariance contains the asymmetry $\boldsymbol{\sigma_{zw}} = \boldsymbol{\sigma_{wz}^*}$ not found in scalar covariance.

The vector correlation is defined as:

$$\boldsymbol{\rho_{zw}} = \frac{\boldsymbol{\sigma_{zw}}}{\sigma_z \sigma_w} \tag{D.0.36}$$

which is analogous to scalar correlation. The squared magnitude of the correlation $\boldsymbol{\rho_{zw}} \boldsymbol{\rho_{zw}^*}$ is the proportion of the variance in w_j explained by the regression equation. The magnitude of the correlation is in the range zero to one and is unaffected by linear transformation of either z_j or w_j.

Consider the regression equation

$$w_j = \beta z_j + \alpha + \epsilon_j \tag{D.0.37}$$

with the complex regression coefficients $\beta = b_0 + ib_1$ and $\alpha = a_0 + ia_1$. Fit error associated with the jth observation is ϵ_j. A least-squares regression then requires that α and β minimize $\sum \epsilon_j \epsilon_j^*$. The regression coefficients are:

$$\beta = \rho_{zw} \frac{\sigma_w}{\sigma_z} \tag{D.0.38}$$

and

$$\alpha = \overline{w} - \beta \overline{z} \tag{D.0.39}$$

Equation D.0.37 implies a transformation that involves translation, rotation, and scaling of the vector z_j. The intercept α defines a translation of coordinates. Rotation and scaling are contained in β, in the magnitude and phase of β, respectively. The phase angle Θ of β can be derived directly from the correlation:

$$\tan \Theta = \frac{\mathrm{Im}\rho_{zw}}{\mathrm{Re}\rho_{zw}} = \frac{\sigma_{xv} - \sigma_{yu}}{\sigma_{xu} + \sigma_{yv}} \tag{D.0.40}$$

These are useful quantities. The magnitude of β is a scaling factor that describes relative magnitudes of vector components. The phase of β describes a consistent phase offset. Neither the correlation magnitude nor the magnitude of β retain a sign. The phase Θ carries the information analogous to sign in scalar correlation, but with more possibilities.

Equation D.0.34 can be modified to obtain a correlation that describes a reflectional relationship between two sets of vectors.

$$\sigma_{z^*w} = \frac{1}{n} \sum_{j=1}^{n} (z_j^* - \overline{z}^*)^* (w_j - \overline{w}) = (\sigma_{xu} - \sigma_{yv}) + i(\sigma_{xv} + \sigma_{yu}) \tag{D.0.41}$$

As with the rotation, reflectional correlation magnitude expresses goodness-of-fit, and the magnitude of β is the scaling factor. The phase Θ of β indicates twice the axis of reflection - the direction of the line about which variations in the paired observations are approximately symmetric. Owing to the symmetry of the reflectional correlation, Θ keeps the same value regardless of whether z or w is the independent vector.

Whether rotation or reflection is the better model can be determined by calculating the rotation/reflection index:

116

$$\xi = \sigma_{xu}\sigma_{yv} - \sigma_{xv}\sigma_{yu} \tag{D.0.42}$$

When ξ is positive, rotation is a better model, whereas if ξ is negative, reflection is better. The physical interpretation of a reflectional relationship is somewhat confusing. Regardless, it is a fundamentally different correlation estimate than rotational vector correlation. This is evident from the 4 independent terms in D.0.42, which boil down to $\sum \boldsymbol{z}^*\boldsymbol{w}$ vs. $\sum \boldsymbol{zw}$. Thus the rotation/reflection index D.0.42 should be included in any correlation analysis as a check on which model is more appropriate.

Appendix E

Least-Expensive-Radar (LERA)

This section regards initial development and evaluation of the Least Expensive Radar (LERA) analog to digital synthesis.

During the week of Dec 1st, 2008 I tested the M-Audio™Delta 1010LT analog-digital conversion board, hereafter M-Audio. The M-Audio is a consumer grade board, retailing for $250. It has 8 unbalanced and 2 SP/DIF I/O channels. It supports external word clock up to 100 KHz, and S/PDIF clock. The internal DSP is 36-bit, with 24-bit data resolution and 96 kHz sampling frequency. The manual states 101.5 and 99.6 dB dynamic range for D/A and A/D conversion, respectively. The decibel rating is not qualified with a suffix, so the reference quantity is ambiguous. Likely possibilities are dBV (1 volt rms) or dBu,dBv (0.7746 volts rms). Likewise, the line-levels for the various inputs can be configured with an ambiguous -10 to +5 dB offset.

Initial tests were performed on a Mini-Box™mini-ITX (cpu model,RAM) running Windows™XP SP3 and Matlab™v.2007a. Resource limitations on this setup have not yet been observed. Software control of the M-Audio was implemented using Playrec, a Matlab™and Octave™utility (MEX file) that provides access to soundcards using PortAudio, an audio I/O library. Both Playrec and PortAudio are free, cross platform, and open-source. Playrec is compatible with a variety of host APIs; including ASIO, WMME and DirectSound under Windows™. A second system employing Ubuntu Linux with identical software setup was also tested (Figure E.1). The logging script does not appear to be affected by the choice of operating system, but a cross comparison has not been performed.

Audio Stream Input/Output (ASIO) is a computer soundcard driver protocol for digital audio specified by Steinberg™, providing a low-latency and high fidelity interface between a software application and a computer's sound card. Whereas Microsoft™DirectSound is commonly used by non-professional users, ASIO bypasses the normal audio path from the user application through layers of intermediary Windows operating system software, allowing the application to
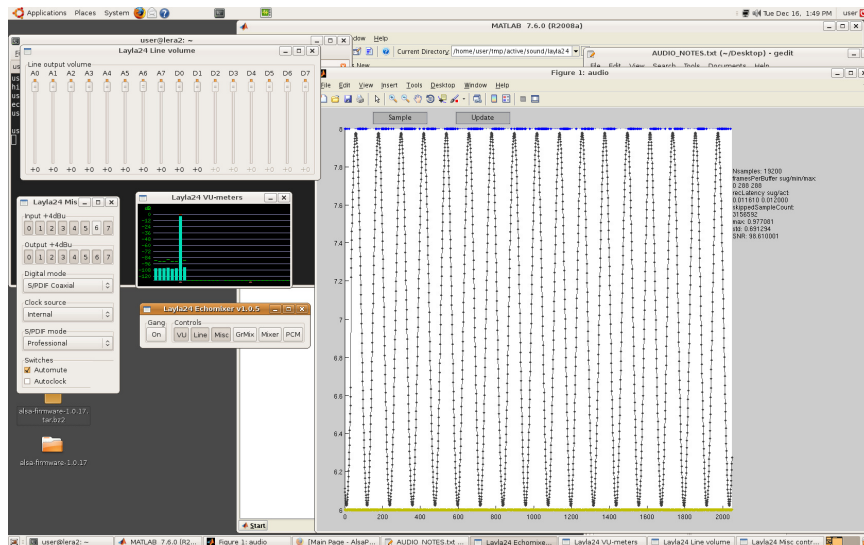
Figure E.1: A screenshot from the current LERA GUI. Software used is the Ubuntu 64-bit Linux operating system, ALSA soundcard drivers, 64-bit Matlab, and the Playrec audio utility.

connect directly to the soundcard hardware. Each layer bypassed means a reduction in latency, the delay between an application sending sound to the sound being reproduced by the soundcard. ASIO offers a relatively simple way of accessing multiple audio inputs and outputs independently. Its primary strength lies in its method of bypassing the inherently high latency of Windows audio mixing kernels (KMixer), allowing direct, high speed communication with audio hardware. Unlike KMixer, an unmixed ASIO output is "bit identical", that is, the bits sent to the sound card are identical to those contained in the software signal. ASIO support is normally restricted to Microsoft Windows, since other operating systems (e.g. Apple's Mac OS X or Linux) do not have such mixer latency problems (see Core Audio and ALSA)(not a qualified or tested statement). ASIO allowed for synchronous control of the M-Audio channels within Matlab, whereas the Windows sound layer did not.

The current Matlab implementation uses a timer object to ensure a buffer of recording pages is queued at all times, and a similar buffer of recorded pages is retained. The number of pages (queue length) is variable, as well as other relevant variables. It displays a text output of real-time performance statistics, e.g. latency and skipped samples.

Preliminary settings resulted in latencies of 1 to 3 ms and 30 samples skipped between each page at a recording rate of 96,000 samples per second for 10 min. This was reduced to zero skipped samples across pages by manually increasing the DMA buffer length in the M-Audio control panel. Apparently the playrec utility was not modifying the DMA buffer length.

119

With current hardware, it would not be possible to hold an entire sampling burst in memory, e.g. 32 channels × 24 bits × 96,000 kHz × 1080 s (18 min) = 9.3 GB. This is not a sampling limitation, as the matlab implementation streams to disk. But, this is a considerable challenge to any processing algorithms requiring the entire timeseries.

The **root mean square** (RMS) is a statistical measure of the magnitude of a varying quantity. It is especially useful when variates are positive and negative, e.g. sinusoids. The RMS of a collection of n values $x_1, x_2, ..., x_n$ is:

$$x_{rms} = \sqrt{\frac{1}{n} \sum_{i=1}^{n} x_i^2} \tag{E.0.43}$$

The corresponding formula for a continuous function $f(t)$ defined over the interval $T_1 \leq t \leq T_2$ is

$$f_{rms} = \sqrt{\frac{1}{T_2 - T_1} \int_{T_1}^{T_2} f(t)^2 dt} \tag{E.0.44}$$

and the RMS for a function over all time is:

$$f_{rms} = \lim_{T \to \infty} \sqrt{\frac{1}{2T} \int_{-T}^{T} f(t)^2 dt} \tag{E.0.45}$$

The RMS value of a continuous function or signal can be approximated by taking the RMS of a series of equally spaced samples. The RMS over all time of a periodic function is equal to the RMS of one period of the function. For example, using E.0.44 the RMS value of both $y = a\sin(x)$ and $y = a\cos(x)$ to be $y_{rms} = a/\sqrt(2)$.

Often we need to know the power P dissipated by an electrical resistance R. This is easy to calculate for a constant current I:

$$P = I^2 R \tag{E.0.46}$$

For a time-varying current $I(t)$, the average power is:

$$\langle P \rangle = \langle I(t)^2 R \rangle = \langle I(t)^2 \rangle R = I_{rms}^2 R \tag{E.0.47}$$

And using Ohm's Law, $I = V/R$, the average power is:

$$\langle P \rangle = V_{rms}^2 / R \tag{E.0.48}$$

When referring to measurements of amplitude it is usual to consider the ratio of the squares of measured A_1 over reference A_0 amplitude. This is because in most applications power is proportional to the square of the amplitude:

$$L_{dB} = 10 \log_{10}(\frac{A_1^2}{A_0^2}) = 20 \log_{10}(\frac{A_1}{A_0}) \tag{E.0.49}$$

Although decibel measurements are always relative to a reference level, if the numerical value of that reference is explicitly stated, then the decibel measurement is called an "absolute" measurement, in the sense that the exact value of the measured quantity can be recovered using E.0.49. Some industry standards encountered using the M-Audio were: dBV; V_{rms} relative to $1V_{rms}$, and dBu; V_{rms} relative to $0.77459667\ V_{rms}$. It can be shown that the relationship between two "absolute" decibel scales of equal units is:

$$L_{dB_2} = L_{dB_1} + 20 log_{10}(\frac{V_1}{V_2}) \tag{E.0.50}$$

where $V_{1,2}$ are RMS voltages. For example, $0 dBV = 2.218 dBu$.

The M-Audio operates by receiving an input voltage on any of the 8 analog input channels, hereafter input, where it is digitized using 24-bit precision. The input is then amplified by the line level, a variable setting within the M-Audio software driver. The line level gain is numerical, not electrical. The resulting data ranges from $\pm$ 1 V.

Evaluation of the M-Audio was performed using the aforementioned logging script and a signal generator. It was found that $4.0 \pm 0.01\ V_{rms}$ input was the maximum threshold before clipping would occur, regardless of line level. Thus, $4.0\ V_{rms}$ is the fundamental upper limit of the M-Audio hardware. Varying the line level gain could potentially result in an additional source of clipping; exceeding the the $\pm$ 1 V range of digitization. Thus the ideal line level gain for this system, given a known input voltage $V_{rms,input}$ is:

$$G_{dB,ideal} = 20 \log_{10}(\frac{1}{\sqrt{2}V_{rms,input}}) \tag{E.0.51}$$

The "Monitor Mixer" within the software control panel displays the current level in dB of the digitized data (referenced to $1V = 0.7071 V_{rms}$). This level should not be confused as a reading of the input signal, it comes after line level gain and digitization.

The line level controls have 3 presets ("+4 dBu","consumer", and "-10 dBV"), or an unlabeled slider with 15 discrete levels. Evaluating E.0.49 for 3 unique input voltages at each line level

yielded the following results:

setting	gain (dB)
minimum	-21.4
+4 dBu	-15
consumer	-9
-10 dBV	-3
maximum	+2.8

A line level setting was found that closely approximated 0 dB gain.

The dynamic range, i.e. signal to noise ratio (SNR), was evaluated using E.0.49, with the RMS data voltage as A_1 and the RMS voltage of a quiescent channel as A_0. Both input voltage and line level gain were varied within the constraints of E.0.51. Exceeding E.0.51 would result in clipping of the data. Varying the sample length did not affect the SNR. This is to be expected, since RMS is a mean, i.e. normalized by the number of samples. Increasing the input voltage improved the SNR. A maximum SNR of 94 dB was achieved using 4.0 V_{rms} and -15 dB line level.

E.1 Results

The unfiltered periodograms of the M-Audio and Layla-24 were very similar. Signal channels had a noise floor at ~ -100 dB far outside of the signal frequency. Near the signal frequency, the noise floor approached ~ -60 dB. The M-Audio exhibited a pronounced spectral ringing.

Applying an 8th order Butterworth lowpass filter (6 KHz cutoff frequency) resulted in a 7.4 dB increase in SNR. Consecutively applying a 16 sample sliding average improved the SNR by another 1.4 dB. Consecutively downsampling by a factor of 16 had no significant effect on the SNR, as the energy had already been rejected. Clearly the low-pass filter rejected high frequency noise energy. Varying the processing steps; A) low-pass B)sliding filter as A,B; A; B, yielded very similar results, all around 7-8 dB SNR gain. This is because the sliding average is a boxcar convolution kernel; effectively the same as the Butterworth.

The signal frequency of 800 Hz was specifically chosen to be an integer divisor of the sampling frequency (96 kHz), thus the periodicity of the timeseries was optimized for the Fourier transform, i.e. to prevent spectral spreading due to end discontinuities in the timeseries. Applying a Hamming window to the timeseries did not improve the SNR. Further analysis is necessary. One possible cause are the observed variations in the initial upslope of each sinusoid (Figure E.4). It is worth noting the quiescent channel was a pretty good approximation to white noise, although some harmonics of the input signal were observed.

Figure E.2: An unfiltered Layla-24 periodogram. Input signal was an 800 Hz sinusoid [blue]. Reference "quiet" channel [green] was at ~ -150 dB

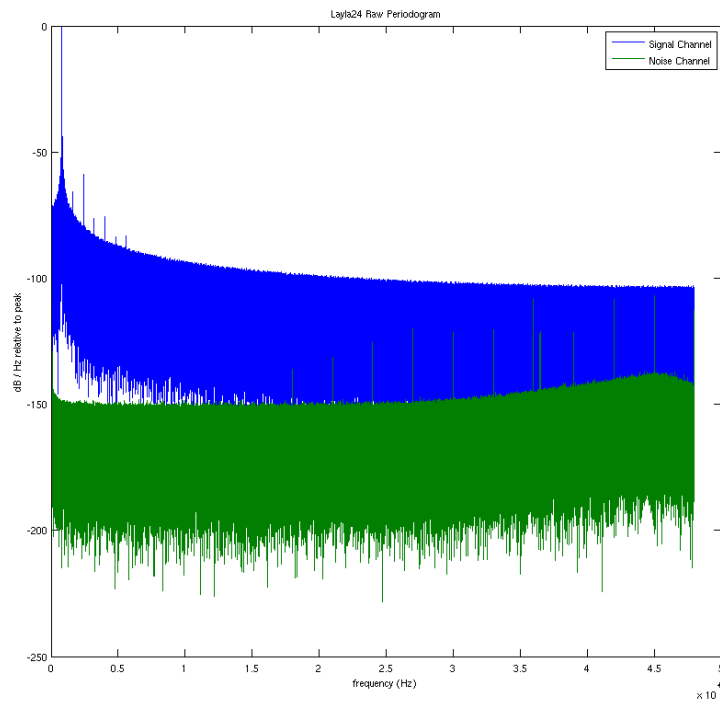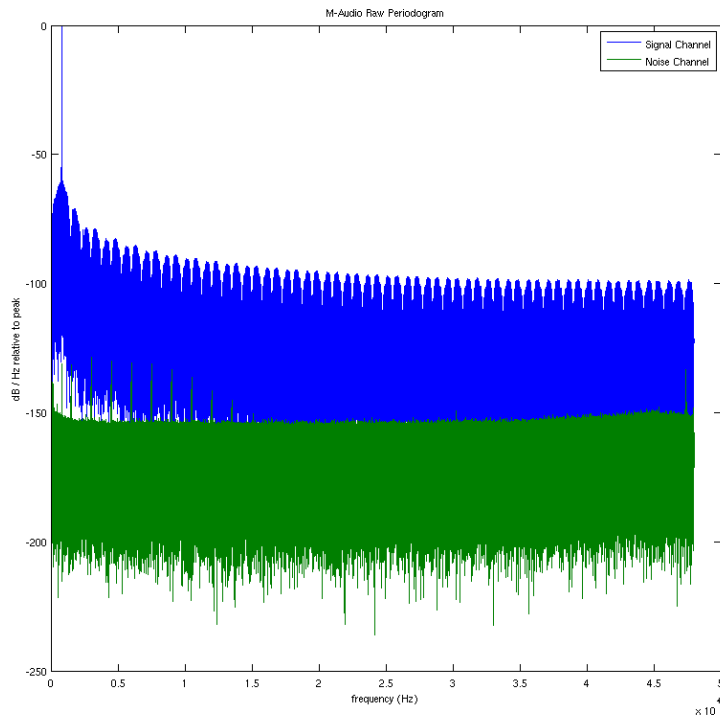Figure E.3: An unfiltered M-Audio periodogram. Input signal was an 800 Hz sinusoid. Reference "quiet" channel [green] was at ~ -150 dB
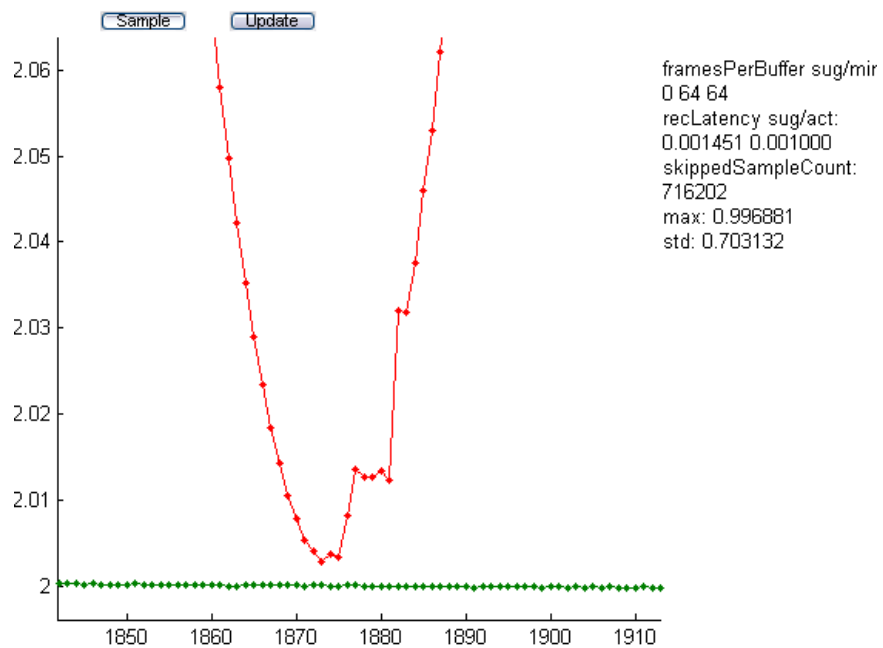
Figure E.4: An example distorted waveform from the LERA data acquisition. This characteristic distortion was often observed in the data; always in the same position- on the immediate upslope of the minimum. It has been suggested this could be a capacitor "unloading"

Bibliography

M.L. Banner and I.R. Young. Modeling spectral dissipation in the evolution of wind waves. part i: Assessment of existing model performance. *J. Phys. Oceanogr.*, 24:1550–1571, 1993.

D.E. Barrick. The interaction of hf/vhf radio waves with the sea surface and its implications. In *AGARD Conference Proceedings*, number 77 in Electromagnetics of the Sea, Sprinfield, VA., 1970. Clearinghouse for Federal Scientific and Technical Information. accession no. AD716305.

D.E. Barrick. Theory of hf and vhf propagation across the rough sea, 1, the effective surface impedance for a slightly rough highly conducting medium at grazing incidence. *Radio Science*, 6(5):517–526, 1971a.

D.E. Barrick. Theory of hf and vhf propagation across the rough sea, 2, application to hf and vhf propagation above the sea. *Radio Science*, 6(5):527–533, 1971b.

D.E. Barrick. First-order theory and analysis of mf/hf/vhf scatter from the sea. *IEEE Trans. Antennas Propagat.*, AP-20:2–10, 1972.

D.E. Barrick. Extraction of wave parameters from measured hf radar sea-echo doppler spectra. *Radio Science*, 12(3):415–424, 1977.

D.E. Barrick. Accuracy of parameter extraction from sample-averaged sea-echo doppler spectra. *IEEE Transactions on Antennas and Propagation*, AP-28(1):1–11, 1980.

D.E. Barrick. Effects of shallow water on radar measurements. Codar report, CODAR Ocean Sensors, January 2005a.

D.E. Barrick. Geometrical dilution of statistical accuracy (gdosa) in multi-static hf radar networks. CODAR reference document, January 2005b.

D.E. Barrick and B.J. Lipa. The role of the gravity-wave dispersion relation in hf radar measurements of the sea surface. *Oceanic Engineering, IEEE Journal of*, 11(2):289–292, 1986.

D.E. Barrick and B.L. Weber. On the nonlinear theory for gravity waves on the ocean's surface. part ii: Interpretation and applications. *J. Phys. Oceanogr.*, 7(1):11–21, 1977.

D.E. Barrick, M.W. Evans, and B.L. Weber. Ocean surface currents mapped by radar. *Science*, 198: 138–144, 1977.

W.L. Bragg. The diffraction of short electromagnetic waves by a crystal. *Proceedigns of the Cambridge Philosophical Society*, 17:43–57, 1913.

S.I. Caires. *Comparative study of HF radar measurements and wave model hindcasts of waves in shallow water*. PhD thesis, University of Sheffield, September 2000.

C. Chavanne. *Observations of the Impact of Mesoscale Currents on Internal Tide Propagation*. PhD thesis, University of Hawaii, USA, 2007.

C. Chavanne, I. Janekovic, P. Flament, P.M. Poulain, M. Kuzmic, and K.W. Gurgel. Tidal currents in the northwestern adriatic: High-frequency radio observations and numerical model predictions. *J. Geophys. Res.*, 112:CO3S21, 1–18, 2007.

S.B. Colegrove. Project jindalee: from bare bones to operational othr. In *The Record of the IEEE 2000 International Radar Conference, 2000*, pages 825–830, Alexandria, VA, May 2000.

D.D. Crombie. Doppler spectrum of sea echo at 13-56 mc/s. *Nature*, 175:681–682, 1955.

D.D. Crombie. Spectral characteristics of hf ground wave signals backscattered from the sea. In *Electromagnetics of the Sea*, number 77 in AGARD Conference Proceedings, 1970.

D.D Crombie. Resonant backscatter from the sea and its application to physical oceanography. In *IEEE International Conference Proceedings on Engineering in the Ocean Environment*, pages 174–179, New York, 1972. IEEE.

V.E. Derr, editor. *Remote Sensing of the Troposphere*, chapter Remote Sensing of Sea State by Radar, pages 12–1–12–46. U.S. National Oceanic and Atmospheric Administration; for sale by the Supt. of Docs., U.S. Govt. Print. Off., Washington, 1972.

M.A. Donelan, Hamilton.J., and W.H. Hui. Directional spectra of wind-generated waves. *Philosophical Transactions of the Royal Society of London*, 315:509–562, 1985.

H.H. Essen, K.W. Gurgel, and T. Schlick. Measurement of ocean wave height and direction by means of hf radar: an empirical approach. *Ocean Dynamics*, 1999.

D.M. Fernandez, H.C Graber, J.D Paduan, and D.E. Barrick. Mapping wind direction with hf radar. *Oceanography*, 10(2):93–95, 1997.

D.B. Gilhousen. A field evaluation of ndbc moored data buoy winds. *J. Atmos. Oceanic Technol.*, 4:94–104, 1987.

H.C. Graber, D.R. Thompson, and R.E. Carande. Ocean surface features and currents measured with synthetic aperture radar interferometry and hf radar. *J. Geophys. Res.*, 101(C11):25,813–25,832, 1996.

K.W. Gurgel and Y. Barbin. Suppressing radio frequency interference in hf radars. *Sea Technology*, pages 39–42, March 2008.

K.W. Gurgel and H.H Essen. On the performance of a ship-borne current mapping hf radar. *IEEE Journal of Oceanic Engineering*, 25(1):183–191, 2000.

K.W. Gurgel, G. Antonischki, H.H. Essen, and T. Schlick. Wellen radar (wera), a new ground-wave based radar for ocean remote sensing. *Coastal Engineering*, 37:219–234, 1999a.

K.W. Gurgel, H.H. Essen, and S.P. Kingsley. Hf radars: Physical limitations and recent developments. *Coastal Engineering*, 37:201–218, 1999b.

K.W. Gurgel, H.H. Essen, and T. Schlick. An empirical method to derive ocean waves from second-order bragg scattering: Prospects and limitations. *IEEE Journal of Oceanic Engineering*, 31(4): 804–811, 2006.

B. Hanson, K. Klink, K. Matsuura, S.M. Robeson, and C.J. Willmott. Vector correlation: Review, exposition, and geographic application. *Annals of the Association of American Geographers*, 82 (1):103–116, 1992.

J. Harlan and T. Georges. An empirical relation between ocean-surface wind direction and the bragg line ratio of hf radar sea echo spectra. *J. Geophys. Res.*, 99:7971–7978, 1994.

K. Hasselmann. Feynman diagrams and interaction rules of wave-wave scattering processes. *Reviews of Geophysics*, 4(1):1–32, 1966.

K. Hasselmann. Determination of ocean-wave spectra from doppler radio return from the sea surface. *Nature*, 299:16–17, 1971.

M.L. Heron and S.F. Heron. Cumulative probability noise analysis in geophysical spectral records. *Internaional Journal of Remote Sensing*, 22(13):2537–2544, 2001.

M.L. Heron, P.E. Dexter, and B.T. McGann. Parameters of the air-sea interface by high-frequency ground-wave doppler radar. *Aust. J. Mar. Freshwater Res.*, 36:655–670, 1985.

M.L. Heron, H.C. Graber, and S.F. Heron. Validation of routine waveheight measurements on hf ocean radars. In *OCEANS 1998 Conference Proceedings*, volume 1, pages 454–458, 1998.

Y. Jun, W. Biyang, and W. Shicai. Method to suppress radio-frequency interference in hf radars. *Electronics Letters*, 40(2):145–146, 2004.

K.E. Kenyon. Stokes drift for random gravity waves. *J. Geophys. Res.*, 74(28):6991–6994, 1969.

M. Kline, editor. *Theory of Electromagnetic Waves*, chapter Reflection of electromagnetic waves from slightly rough surfaces, pages 351–378. Interscience and Dover, New York, 1951.

P.M. Kosro, J.A. Barth, and P.T. Strub. The coastal jet: Observations of surface currents over the oregon continental shelf from hf radar. *Oceanography*, 10(2):53–56, 1997.

P.K. Kundu, I.M. Cohen, and H.H. Hu. *Fluid Mechanics*, chapter 7, pages 238–240. Elsevier Academic Press, 3rd edition, 2004.

K. Laws, J.D. Paduan, and D.M. Fernandez. Effect of stokes drift on hf radar measurements. In H.C. Graber and J.D. Paduan, editors, *Radiowave Oceanography: The First International Workshop*, pages 51–57, April 2001.

B.J. Lipa and D.E. Barrick. Least-squares method for the extraction of surface currents from codar crossed-loop data: Application at arsloe. *IEEE J. Ocean Eng.*, 8:226–253, 1983.

B.J. Lipa and B. Nyden. Directional wave information from the seasonde. *IEEE Journal of Oceanic Engineeering*, 30(1):221–231, 2005.

A.E Long and D.B. Trizna. Mapping of north atlantic winds by hf radar sea backscatter interpretation. *IEEE Trans. Antennas Propag.*, AP-21:680–685, 1973.

M.S. Longuet-Higgins and O.M. Phillips. Phase velocity effects in tertiary wave interactions. *Journal of Fluid Mechanics*, 12:333–336, 1962.

M.S. Longuet-Higgins, D.E. Cartwright, and N.D. Smith. *Ocean Wave Spectra*, chapter Observations of the Directional Spectrum of Sea Waves using Motions of a Floating Buoy. Prentice-Hall, Englewood Cliffs, NJ, 1963.

A. Lygre and H.E. Krogstad. Maximum entropy estimation of the directional distribution in ocean wave spectra. *J. Phys. Oceanogr.*, 16(12):2052–2060, 1986.

J.W. Maresca and T. Georges. Measuring rms wave height and the scalar ocean wave spectrum with hf skywave radar. *J. Geophys. Res.*, 85(C5):2759–2771, 1980.

D. Masson. Observations of the response of sea waves to veering winds. *J. Phys. Oceanogr.*, 20: 18876–1885, 1990.

K.J. Molnar, W. Lin, and M. O'Donnell. Beamforming and aberration correction in hf radar. In *Record of the IEEE 1990 International Radar Conference*, pages 90–95, 1990.

W.A. Nierenberg and W.H. Munk. Sea spectra and radar scattering. In *Working Paper, 1969 Jason Summer Study*. ''", Boulder, CO, 1969.

H. Nyquist. Thermal agitation of electric charge in conductors. *Physical Review*, 32(1):110–113, 1928.

A.M Peterson, C.C. Teague, and G.L. Tyler. Bistatic-radar observation of long-period, directional ocean-wave spectra with loran a. *Science*, 170(3954):158–161, 1970.

O.M. Phillips. The equilibrium range in the spectrum of wind-generated ocean waves. *J. Marine Res.*, 16:231–245, 1958.

O.M. Phillips. *Dynamics of the Upper Ocean*. Cambridge University Press, London, 1966.

W.J. Pierson Jr. Examples of, reasons for, and consequences of the poor quality of wind data from ships for the marine boundary layer: Implications for remote sensing. *J. Geophys. Res.*, 95: 13,313–13,340, 1990.

A.M. Ponsford, R.M. Dizaji, and R. McKerracher. Hf surface wave radar operation in adverse conditions. In *Proceedings of the International Conference on Radar*, pages 593–598, 2003.

D. Prandle. The fine-structure of nearshore tidal and residual circulations revealed by h.f. radar surface current measurements. *J. Phys. Oceanogr.*, 17(2):231–245, 1987.

D. Prandle and D.K. Ryder. Measurement of surface currents in liverpool bay by high frequency radar. *Nature*, 315:128–131, 1985.

D. Prandle and D.K. Ryder. Comparison of observed and modeled nearshore velocities. *Continental Shelf Research*, 9(12):1029–1104, 1989.

G.T. Ruck, D.E. Barrick, W.D. Stuart, and C.K. Krichbaum. *Radar Cross Section Handbook*, volume 1. Plenum Press, New York, 1970. pg. 53.

J.A. Saxton, editor. *Advances in Radio Research*, volume 1, chapter Electromagnetic surface waves, pages 157–217. Academic, New York, 1964.

R.O. Schmidt. Multiple emitter location and signal parameter estimation. *IEEE Trans. Antennas Propag.*, 34:276–280, 1986.

L.K. Shay. Internal wave-driven surface currents from hf radar. *Oceanography*, 10(2):60–63, 1997.

L.K. Shay, H.C. Graber, D.B. Ross, and R.D. Chapman. Mesoscale ocean surface current structure detected by high-frequency radar. *Journal of Atmospheric and Oceanic Technology*, 12(4):881–900, 1995.

E.D. Shearman and L.R. Wyatt. Dekametric radar for surveillance of sea-state and oceanic winds. *The Journal of Navigation*, 35:397–40, 1982.

V.I. Shrira, D.V. Ivonin, P. Broche, and J.C. de Maistre. On remote sensing of vertical shear of ocean surface currents by means of a single-frequency vhf radar. *Geophysical Research Letters*, 28(20):3955–3958, 2001.

R.H. Stewart and J.R. Barnum. Radio measurements of oceanic winds at long ranges: An evaluation. *J. Phys. Oceanogr.*, 10:128–143, 1975.

R.H. Stewart and J.W. Joy. Hf radio measurements of ocean surface currents. *Deep Sea Research*, 21:1039–1049, 1974.

G.G. Stokes. On the theory of oscillatory waves. *Transactions of the Cambridge Philosophical Society*, 8:441–445, 1847.

C.C. Teague. *High-Frequency Resonant Scattering Techniques for Observation of Directional Ocean-Wave Spectra*. PhD thesis, Stanford University, Stanford, California, 1971.

C.C. Teague, J.F. Vesecky, and D.M. Fernandez. Hf radar instruments, past to present. *Oceanography*, 10(2):40–44, 1997.

G.L. Tyler, W.E. Faulkerson, A.M. Peterson, and C.C. Teague. Second-order scattering from the sea: Ten-meter radar observations of the doppler continuum. *Science*, 177(4046):349–351, 1972.

G.P. van Vledder and L.H. Holthuijsen. The directional response of ocean waves to turning winds. *J. Phys. Oceanogr.*, 23(2):177–192, 1993.

J.F. Vesecky, J. Drake, C.C. Teague, F.L. Ludwig, K. Davidson, and J. Paduan. Measurement of wind speed and direction using multifrequency hf radar. In *Geoscience and Remote Sensing Symposium*, IGARSS, pages 1899–1901. IEEE International, 2002.

H. von Storch and F.W. Zwiers. *Statistical analysis in climate research*. Cambridge University Press, Cambridge, 1999.

B.L. Weber and D.E. Barrick. On the nonlinear theory for gravity waves on the ocean's surface. part i: Derivations. *J. Phys. Oceanogr.*, 7(1):3–10, 1977.

L.R Wyatt. The ocean wave directional spectrum. *Oceanography*, 10:85–89, 1997.

L.R. Wyatt. Hf radar wind measurement - present capabilities and future prospects. In H.C. Graber and J.D. Paduan, editors, *Radiowave Oceanography: The First International Workshop*, pages 82–87, April 2001.

L.R. Wyatt and J.J. Green. The availability and accuracy of hf radar wave measurements. In *2002 IEEE International Geoscience and Remote Sensing Symposium*, pages 515–517, 2002.

L.R. Wyatt, S.P. Thompson, and R.R. Burton. Evaluation of high frequency radar measurement. *Coastal Engineering*, 37:259–282, 1999.

L.R. Wyatt, J.J. Green, K.W. Gurgel, J.C. "Nieto Borge", K. Reichert, K. Hessner, H. Günther, W. Rosenthal, O. Saetra, and M. Reistad. Validation and intercomparisons of wave measurements and models during the eurorose experiments. *Coastal Engineering*, 48:1–28, 2003.

L.R Wyatt, G. Liakhovetski, H.C. Graber, and B.K. Haus. Factors affecting the accuracy of showex hf radar wave measurements. *Journal of Atmospheric and Oceanic Technology*, 22:847–859, 2005.

L.R Wyatt, J.J. Green, A. Middleditch, M.D. Moorhead, J. Howarth, M. Holt, and S. Keogh. Operational wave, current, and wind measurements with the pisces hf radar. *IEEE Journal of Oceanic Engineering*, 31(4):819–834, 2006.